EXPERIMENTAL STUDY OF DYNAMIC FRICTIONAL SLIDING MODES ALONG INCOHERENT INTERFACES

Thesis by

George Lykotrafitis

In Partial Fulfillment of the Requirements for the

Degree of

Doctor of Philosophy

CALIFORNIA INSTITUTE OF TECHNOLOGY

Pasadena, California

2006

(Defended November 21, 2005)

ACKNOWLEDGEMENTS

I would like to express my sincere gratitude to my thesis advisor, Professor Ares J. Rosakis, for his invaluable guidance, support and encouragement during my years at Caltech. I have greatly benefited from his intuition, his innovative, constructive and rigorous approach to various problems that emerged during my research. He will always be a reference point for me due to his dedication to research, his zeal for teaching, and in general for his energetic and optimistic attitude.

I sincerely thank Professor Guruswami Ravichandran for his generous and always to-the-point advice, which decisively helped me to advance and complete this work. I am always impressed by his deep understanding of the underlying physics of the engineering problems and by his capacity of easily unfolding complicated situations and focus on the essential features of the subjects under consideration.

I am grateful to Professor Hiroo Kanamori for his wise suggestions during my research. I am indebted to Professor Needleman for his encouraging comments and his generous help. I also sincerely thank Professor Nadia Lapusta for many helpful discussions on dynamic friction and for her invaluable help in interpreting the experimental results. I am grateful to Professor James Knowles, Professor Jeroen Tromp, and Professor Yonggang Huang, who served on my thesis committee and have provided many valuable suggestions.

I sincerely thank my former advisor at NTUA Professor Haralampos G. Georgiadis for his wise advices and his generous help. I wish to also thank Professor Demir Coker for many discussions on dynamic friction and his kind hospitality when I visited his laboratory in Oklahoma State University at Stillwater. I thank Dr. David Anderson for introducing me to dynamic fracture experimental facilities. I also owe many thanks to all the previous students of Professor Rosakis, since they greatly contributed to the development of the laboratory where I completed this work. Special thanks to Petros Arakelian, who was always very helpful and resourceful. I also thank Joe Haggerty, Ali Kiani and Bradley St. John for their help in the machine shop.

I am deeply thankful to Donna Mojahedi for her help during my thesis work. She has the rare talent to accomplish even the most tedious work with patience, dedication and good-nature.

It was a real pleasure to live, work and interact at Caltech with my fellow students and postdocs. They are too many to list in this short space, but I can not miss expressing my gratitude to Gianluca Bonuglia, Yashasree Kulkarni, George Matheou, Min Tao, Amir Sadjadpour, Kaiwen Xia, Michal Brown, Xiao Lu, Rongjing Zhang, Theresa Kidd, Samantha Feakins, Winston Jackson, Christian Franck, Dr. Vijay Chalivendra, Dr. Soonsung Hong, Dr. Abhishek Bhattacharyya and Dr. YaBei Gu.

Financial support for this work was provided by the Office of Naval Research and National Science Foundation and is gratefully acknowledged.

ABSTRACT

Dynamic sliding at high strain rates along incoherent (frictional) interfaces is investigated experimentally in a microsecond time scale. A bimaterial system comprised of Homalite and steel plates and a homogeneous system consisting of two Homalite plates are considered. The plates are held together by a uniform compressive stress while dynamic sliding is initiated by an impact-induced shear loading.

The evolution of maximum shear stress contours is recorded by high-speed photography in conjunction with dynamic photoelasticity. A newly developed technique based on laser interferometry is employed to locally measure sliding speed at the interface. The combination of the classic full-field technique of photoelasticity with the local technique of velocimetry is proven to be a very powerful tool in the investigation of dynamic sliding.

The response of the Homalite-steel bimaterial system differs according to whether the impact loading is applied to the Homalite plate or to the steel plate. In the first case, the interaction between the traveling impact wave and the preexisting static field causes the generation of a relatively broad eye-like fringe formation emanating from the interface and propagating just behind the P-wave front. A disturbance traveling at the interface at a constant speed close to the Rayleigh wave speed of steel, which is higher than the shear wave speed of Homalite, generates a shear Mach line crossing the P-wave front and the eye-like fringe structure. Velocimetry reveals that sliding initiates behind the eye-like fringe pattern. A second shear Mach line, originating from the sliding tip, appears in the

photoelastic images, indicating that the sliding is supershear with respect to the shear wave speed of Homalite. A disturbance, traveling at constant speeds between the shear wave speed and the longitudinal wave speed of Homalite, appears behind the sliding tip. Self-sustained wrinkle-like opening pulses, propagating along the bimaterial interface at a constant speed between the Rayleigh wave and the shear wave speed of Homalite, are also observed. When the impact load is applied to steel plate, then the data acquired by the velocimeter are the only useful source of information. Analysis of these data shows that sliding at a given point initiates with the arrival of the P-wave front there, so that the rupture is sonic with respect to the steel and supersonic with respect to the Homalite.

A central issue in the modeling of frictional sliding is the duration of the slip at a point on the interface compared to the duration of sliding. The most classic approach of sliding uses shear crack models (crack-like mode), where the slip duration at a point is significant fraction of the overall sliding. According to the pulse-like model, the duration of slip at a point is considerably shorter than the duration of sliding.

In all the experiments performed on the bimaterial structure (Homalite-steel), sliding occurs always in a crack-like mode. In the case of a homogeneous system of Homalite plates, however, direct physical evidence of different modes of sliding is recorded. Crack-like sliding, pulse-like sliding and mixed mode sliding in the form of pulses followed by a crack are discovered. The propagation speeds of the sliding tips are not dependent on the confining stress but only on the projectile speed. They span almost the whole interval from sub-Rayleigh speeds to nearly the sonic speed of the material, with the exception of a

forbidden gap between the Rayleigh wave speed and the shear wave speed. Supersonic trailing pulses are also recorded. Mach lines with different inclination emanating from the sliding zone tips are discovered. Behind the sliding tip, wrinkle-like pulses are developed for a wide range of impact speeds and confining stresses. They always travel at speeds between the Rayleigh wave speed and the shear wave speed of Homalite.

TABLE OF CONTENTS

Acknowledgements iii
Abstract vi
Table of Contents ix
Summary xi
Chapter 1: Introduction 1
References 15
Chapter 2: Experimental Methods 21
2.1 Introduction 21
2.2 Materials and Specimen Configuration 21
2.3 Experimental Setup and Procedure 23
2.3.1 Dynamic Photoelasticity Setup 23
2.3.2 Sliding Velocity Measurement Setup 24
2.3.3 Simultaneous measurements of the Horizontal and Vertical Components of the Velocity 25
2.4 Background Experimental work 25
2.4.1 Particle Velocity Measurement Setup 26
2.4.2 Reliability of the Proposed Technique 27
References 32
List of Figures 33
Figures 36
Chapter 3: Frictional Sliding of Incoherent Bimaterial Interfaces Subjected to Impact Shear Loading 46
3.1 Introduction 46
3.2 Materials and Specimen Configuration 48
3.3 Experimental Setup and Procedure 49
3.3.1 Dynamic Photoelasticity Setup 50
3.3.2 Sliding Velocity Measurement Setup 51
3.3.3 Simultaneous Measurement of the Horizontal and Vertical Components of the Velocity 51
3.4 Sliding Induced by an Impact Shear Loading Applied on the Homalite Plate of a Bimaterial Specimen 52
3.4.1 Initiation and Evolution of Dynamic Frictional Sliding 52
3.4.2 Influence of Impact Speed and Confining Stress on Sliding 58
3.4.3 Observation of Wrinkle-like Pulses 62
3.4.4 Frictional Sliding Induced by High Impact Speeds 66
3.4.5 Study of the Speeds of the Various Features Propagating along the Bimaterial Interface 69
3.5 Sliding Induced by Impact Shear Loading Applied on the Steel Plate of the Bimaterial Specimen 70
3.6 Concluding Remarks 73

References 75
List of Figures 77
Figures 82
Chapter 4: Dynamic Frictional Sliding along Incoherent Interfaces of Homogeneous Systems at Low Impact Speeds 100
4.1 Introduction 100
4.2 Specimen Configuration and Loading 103
4.3 Experimental Techniques 104
4.4 Experimental Results 105
4.4.1 Initiation of Dynamic Frictional Sliding 105
4.4.2 Visualizing Pulse-like and Crack-like Ruptures in the Laboratory 107
4.4.3 Wrinkle-like Pulses along Interfaces in Homogeneous Systems 115
4.5 Conclusions 120
References 121
List of Figures 125
Figures 130
Chapter 5: Dynamic Frictional Sliding along Incoherent Interfaces of Homogeneous Systems Induced by High-Speed Impact Shear Loading 142
5.1 Introduction 142
5.2 Material and Specimen Configuration 142
5.3 Experimental Procedure 143
5.4 Photoelastic Stress Field during Dynamic Sliding of a Homalite Plate Subjected to a Constant External Compressive Stress and Different Impact Speeds 145
5.5 Frictional Sliding without Confining Pressure 154
5.6 Influence of External Pressure on the Sliding Process 157
5.7 Effect of the Surface Roughness on Dynamic Sliding 159
5.7.1 Dynamic Sliding of Polished Surfaces 160
5.7.2 Dynamic Sliding of Roughened Surfaces 161
5.8 Conclusions 162
References 164
List of Figures 165
Figures 169
Chapter 6: Epilogue 184
References 188

SUMMARY

This doctoral dissertation consists of five chapters. The overall theme is the experimental study of dynamic sliding along incoherent (frictional) interfaces featuring in a bimaterial system comprised of Homalite and steel plates, and a homogeneous system consisting of two Homalite plates. The plates are held together by a uniform compressive stress, while sliding is initiated by a shear loading induced via an edge impact near the interface. In the first chapter, an introduction to the subject of dynamic frictional sliding is presented. The second chapter illustrates the experimental methods employed in this investigation. It describes the experimental configuration for the dynamic photoelasticity and it details a newly developed technique, which is based on laser interferometry, for local sliding velocity measurement. Finally, the reliability of the proposed technique is tested extensively.

In the third chapter, dynamic photoelasticity in conjunction with velocimetry is employed in the study of frictional sliding along the incoherent interface of a Homalite-steel bimaterial system in a microsecond time scale. The response of the system differs according to whether the impact loading is applied to the Homalite plate or to the steel plate. In the first case, the interaction between the traveling impact wave and the preexisting static field causes a relatively broad eye-like fringe formation, which emanates from the interface and travels behind the P-wave front. A disturbance traveling at the interface at a constant speed close to the Rayleigh wave speed of steel, (which is higher than the P-wave of Homalite,) generates a shear Mach line that crosses the P-wave front

and the eye-like fringe structure. Data recorded by the velocimeter show that this disturbance affects the relative velocity but does not create sliding. Velocimetry reveals that sliding initiates behind the eye-like fringe pattern. A second shear Mach line, emanating from the sliding tip, appears in the photoelastic images, indicating that the sliding is supershear with respect to the shear wave speed of Homalite. A disturbance, traveling at constant speeds between the shear wave speed and the longitudinal wave speed of Homalite, appears behind the sliding tip. Self-sustaining wrinkle-like pulses propagating along the bimaterial interface are also observed. It is expected that wrinkle-like pulses might play an important role in the failure mechanism of bimaterial structures subjected to impact shear loading. Unlike classic shear cracks in coherent interfaces of finite strength, sliding areas in frictional interfaces seem to grow without any noticeable acceleration phase and at various discrete speeds. When the impact load applies to steel plate then the data acquired by the velocimeter are the only useful source of information. Analysis of these data shows that sliding initiates with the arrival of the P-wave front so that the rupture is sonic with respect to the steel and supersonic with respect to Homalite.

A central issue in the modeling of frictional sliding is the duration of the slip at a point on the interface compared to the duration of sliding. The most classic approach of sliding uses shear crack models (crack-like mode), where the slip duration at a point is significant fraction of the overall sliding. According to the pulse-like model, the duration of slip at a point is one order of magnitude shorter than the overall duration of sliding. In all the performed experiments on bimaterial structures (Homalite-steel), sliding occurs always in a crack-like mode.

In chapter 4 however, where the case of the homogeneous system of Homalite plates is studied, photoelasticity in conjunction with velocimetry provide direct physical evidence of different sliding modes. Crack-like, pulse-like and mixed mode sliding in the form of sliding pulses followed by a crack are discovered and recorded. The mechanism of sliding initiation and its dependence on impact speeds and on confining stress is studied thoroughly. A relatively broad loading wave caused by the interference between the impact wave and the preexisting static stress field is observed emanating from the interface. Sliding velocity measurements reveal that sliding starts behind the loading wave. In addition, evidence of wrinkle-like pulses generated for a wide range of impact speeds and confining stresses are recorded.

The combined use of classic dynamic photoelasticity with velocimetry allowed us to fully characterize the frictional sliding process. However, the maximum particle velocity which can be measured by the velocimeter is $10\,m/s$. In order to work within the above limit, low impact speeds were used in chapter 4. This limitation is suspended for the experiments in chapter 5, where only dynamic photoelasticity in conjunction with high-speed photography is used as a diagnostic tool. Thus, a wide spectrum of impact speeds is employed for sliding initiation. Experimental results obtained at high impact speeds (on the order of $80\,m/s$) are compared to results obtained at low impact speeds (on the order of $10\,m/s$). The observed propagation speeds of the sliding tips are not dependent on the confining stress but only on the projectile speed. They span almost the whole interval from sub-Rayleigh speeds to

nearly the sonic speed of the material, with the exception of a forbidden gap between the Rayleigh wave speed and the shear wave speed. Supersonic trailing pulses are also recorded. Mach lines with different inclination angles emanating from the sliding zone tips are discovered. In addition, behind the sliding tip, wrinkle-like pulses are generated for a wide range of impact speeds and confining stresses. They always travel at speeds between the Rayleigh wave speed and the shear wave speed of Homalite.

Besides the impact speed, the static confining stress and the surface roughness are two parameters which also drastically affect the dynamic sliding. Three different types of contact surfaces with one order of magnitude difference in roughness between each other are also used. It is concluded that the surface roughness does not affect the propagation speeds of the rupture tip or the propagation speed of the wrinkle-like pulse. It affects, however, the rupture initiation process.

Finally, it is noted that the following four papers have been emerged from this work:

Coker, D., Lykotrafitis, G., Needleman, A. & Rosakis, A. J. Frictional sliding modes along an interface between identical elastic plates subject to shear impact loading. *J. Mech. and Phys. of Solids*. **53**, 884-922 (2005).

Lykotrafitis, G., Rosakis, A. J. & Ravichandran, G. Particle Velocimetry and Photoelasticity Applied to the Study of Dynamic Sliding Along Frictionally-Held Bimaterial Interfaces: Techniques and Feasibility. *Experimental Mechanics*. Accepted 2005.

Lykotrafitis, G., Rosakis, A. J. & Ravichandran, G. Visualizing “pulse-like” and “crack-like” ruptures in the laboratory. *Nature*. Submitted (2005).

Lykotrafitis, G. & Rosakis, A. J. Sliding along frictionally held incoherent interfaces in homogeneous systems subjected to dynamic shear loading. *Int. J. Fract.* Submitted (2005).

And three other papers are in preparation:

Lykotrafitis, G. & Rosakis, A. J. Experimental investigation of dynamic frictional sliding along incoherent interfaces in bimaterials. (In preparation).

Rosakis, A. J., Lykotrafitis, G., Xia, K., and Kanamori, H. Dynamic shear rupture in frictional interfaces: speeds, directionality and modes, (Invited review paper in *Treatise on Geophysics*, Volume 4, Earthquake Seismology: Fracture and Frictional Mechanics - Experimental Study I, in preparation)

Lykotrafitis, G., Coker, D., Rosakis, A. J. & Needleman, A. Dynamic frictional sliding modes in homogeneous systems: A comparison between experimental studies and finite elements simulations. (In preparation).

C h a p t e r 1

Introduction

Many physical systems of interest to both engineering and applied sciences involve dynamic frictional sliding along incoherent interfaces between two deformable solids. Examples include moving machinery surface interactions (relevant to both macro- and micro-machinery operations), material processing (e.g., cutting), the failure of fiber reinforced composites (e.g., dynamic fiber pullout) as well as earthquake dynamics (fault rupture). However, a unified framework for quantifying the wide range of observed dynamic frictional phenomena is only beginning to emerge. The classical Amontons-Coulomb description of friction states that shear stress at an interface is proportional to the normal stress, with the coefficient of proportionality being the coefficient of friction. In this classic description of friction, two coefficients of friction are identified: a static coefficient of friction that governs the onset of sliding and a dynamic coefficient of friction that characterizes the behavior during sliding. In a slightly more advanced description, the coefficient of friction may take the form of a simple function of sliding distance (slip) or of sliding speed or of both while the linear dependence on normal stress is still preserved.

From the microscale point of view, an evolving population of contacts and their local deformation, phase transition and fracture and the presence of various lubricants appear to play an important role in controlling the functional form of the dependence of frictional strength on slip sliding speed and normal stress. From the phenomenological point of view, rate and state models of friction have recently been introduced in an attempt to replace the

simplistic Amontons-Coulomb descriptions given above (e.g. Dieterich 1979; Ruina 1983; Rice and Ruina 1983; Linker and Dieterich 1992; Prakash and Clifton 1993; Prakash 1998). Such models, based on experimental observations, attempt to describe the local microprocesses of surface interaction and to introduce the notion of "system memory" through appropriately chosen state variables. Rate and state models of friction have come to the fore because they substantially influence the predicted mode and stability of the dynamic interfacial sliding processes (Coker, Lykotrafitis, Needleman and Rosakis 2005).

Dynamic sliding modes

There are two widely accepted approaches to the description of dynamic sliding (Rice 2001). The most classic approach uses elastodynamic shear rupture (or crack) models in which the surfaces behind the leading edge of rupture (rupture tip) continuously slide and interact through contact and friction. More recently, pulse-like models in which sliding occurs over a relatively small propagating region have been introduced. In these models, the sliding is confined to a finite length and is followed by interfacial locking.

The duration of slip at a point on an interface (or fault) in comparison with the duration of the rupture of the entire fault is a central issue in the modeling of earthquake rupture (Rice 2001). The crack-like mode has been generated in many numerical simulations of spontaneous rupture when a rate-independent friction law was implemented (Madariaga 1976; Andrews 1976 and 1985; Das and Aki 1977; Day 1982; Ruppert and Yomogida 1992; Harris and Day 1993). It has been pointed out, however, that inversions of seismic data for slip histories from well-recorded events (Heaton 1982 and 1990; Hartzell and

Heaton 1983; Liu and Helmberger 1983; Mendoza and Hartzell 1988 and 1989) indicate that the duration of slip at a point on the fault was one order of magnitude shorter than the event duration, giving rise to the concept of a pulse-like rupture mode. Some eyewitness accounts also reported short slip duration (Wallace 1983; Pelton, Meissner and Smith 1984).

The concept of a pulse-like rupture went against a widely-accepted view of how seismic rupture occurs. Its introduction was followed by various efforts to illuminate the physics leading to this process through analytical and numerical investigations. Different mechanisms for "self-healing" pulse generation along faults in homogeneous systems have been proposed. One postulation is that if the fault strength is low immediately behind the rupture front and is increased rapidly at a finite distance, then slip might be restricted to a short, narrow propagating area (Brune 1976). Recent theoretical and numerical investigations show that a strong velocity-weakening friction law model could indeed allow for pulse-like behavior of rupture under certain conditions (Zheng and Rice 1998). However, simulations utilizing velocity weakening have sometimes resulted in crack-like rupture and sometimes in "self-healing" pulse propagation (e.g., Cochard and Madariaga 1994 and 1996; Perrin, Rice and Zheng 1995; Beeler and Tullis 1996; Ben-Zion and Rice 1997; Lapusta et al. 2000; Cochard and Rice 2000; Nielsen, Carlson and Olsen 2000; Coker et al. 2005; Lapusta 2005). Friction laws along interfaces between two identical elastic solids have to include laboratory-based state evolution features and they must not exhibit ill-posedness or paradoxical features (Cochard and Rice 2000; Ranjith and Rice 2001). It has been proven that generalized rate and state friction laws are appropriate

candidates for uniform faults (Cochard and Rice 2000; Ranjith and Rice 2001; Rice, Lapusta and Ranjith 2001; Zheng and Rice 1998). Within the frame of rate and state friction laws, the following three requirements have to be fulfilled for rupture to occur as a "self-healing" pulse (Zheng and Rice 1998; Rice 2001). One requirement is that the friction law must include strengthening with time on slipped portions of the interface that are momentarily in stationary contact (Perrin, Rice and Zheng 1995). Another is that the velocity weakening at high slip rates must be much greater than that associated with the weak logarithmic dependence observed in the laboratory during low-velocity sliding experiments. Lastly, the third requirement is that the overall driving stress has to be lower than a certain value, but high enough to allow for self-sustained pulse propagation (Zheng and Rice 1998).

While strong velocity weakening is a mechanism which explains the onset of short duration slip-pulses along interfaces (faults) which separate similar materials, it is important to note that other mechanisms exist as well. One involves geometric confinement of the rupture domain by unbreakable regions (barrier model). That is, sliding (an earthquake) consists of a number of crack-like ruptures of short duration on a small rupture area that are separated by locked regions (Aki, 1979; Papageorgiou and Aki 1983a and 1983b). In one implementation of this scenario, a pulse-like rupture behavior was found in a 3D geometry when the rupture process was confined within a long but narrow region by unbreakable barriers (Day 1982). It was observed that the rupture started in a classic crack-like mode and it propagated in all directions. After some time, arresting waves arrived from the boundaries and they effectively relocked the fault behind the rupture front, resulting in two

slip pulses. Alternatively, a rupture nucleates and propagates bilaterally, but may arrest suddenly at a strong barrier at one end. Following its arrest, the reflected waves from the barrier spread back and heal the rupture surface. The combination of the still-propagating end of the rupture with the healing reflected wave forms a moving pulse-like configuration (Johnson 1990).

In general, narrow slip pulses can be generated during dynamic sliding along interfaces by strongly velocity-weakening friction on a homogeneous system (same material across the interface), by strong fault zone heterogeneities (Rice 2001) or by variations in normal stress along the rupture interface. All of the above conditions (velocity weakening, heterogeneities and bimaterial contrast) can produce slip pulses with low dynamic stress at the active part of the slip and provide satisfactory solution to the heat flow paradox. An extensive discussion of the subject is presented by Nielsen and Madariaga 2003. We finally note that finite element calculations have been carried out by Coker, Lykotrafitis, Needleman and Rosakis 2005 for a configuration similar to the experimental setup used in this work. These simulations show that generation of slip pulses along an interface characterized by a rate and state dependent frictional law is feasible.

Stability of sliding modes

Renardy (1992) and Adams (1995) showed that sliding along a bimaterial interface governed by Amontons-Coulomb friction is unstable to periodic perturbations, with an instability growth rate proportional to the wave number, for a wide range of friction coefficients and material properties. Ranjith and Rice (1995) found that for moderate

material contrast for which the generalized Rayleigh wave exists, there are unstable modes for all values of the Coulomb friction coefficient. On the other hand, when the material contrast is large enough so that the Generalized Rayleigh wave does not exist, such unstable modes appear only for a friction coefficient larger than a critical value. For lower values of friction coefficient, periodic disturbances are either neutrally stable (do not grow with time) or stable (diminishing with time giving rise to stable sliding). Mathematically, instability makes the response of a material interface with Coulomb friction ill-posed (no solution exists) to generic (nonperiodic) perturbations or pulses, which can be thought of as infinite superposition of periodic perturbations of various wavelengths. Physically, the above instability implies that during sliding, energy is transferred to shorter wave lengths, leading to pulse sharpening and splitting. Numerically, the splitting of individual pulses creates inherent grid-size dependency for numerical calculations (Andrews and Ben-Zion 1997, Ben-Zion and Andrews 1998). Ranjith and Rice 2001 demonstrated that an experimentally-based rate and state dependent friction law (Prakash-Clifton 1993, Prakash 1998), in which the shear strength in response to an abrupt change in normal stress evolves continuously over time, provides well-posedness (regularization) to the problem of generic perturbations propagation (solutions for non-splitting single pulses can be found). Convergence through grid size reduction is then achieved (Cochard and Rice 2000). Ben-Zion and Huang 2002 proved that though the mathematical problem with regularized friction is well-posed, the self-sharpening behavior of the pulses still exists for large enough propagation distances or equivalently for long times. We finally note that use of rate and state dependent friction not only regularize the ill-posedness of the sliding problem but also eliminates certain features of models of sliding

between two identical elastic solids such as supersonic propagation of rupture fronts (Rice, Lapusta and Ranjith 2001). However, the physical reason for excluding supersonic propagation is not clear.

In the case of sliding along an interface between two identical elastic solids (no mismatch in wave speeds across the interface) there is no coupling between normal stress and slip. Unstable slip is impossible under symmetric far field loading if the interface is governed by the classical Amontons-Coulomb law (i.e., with a single, constant coefficient of friction). Indeed, as described by Rice 2001, the study of instable pulses requires more elaborate friction laws for which, under constant normal stress, the frictional strength at a point decreases as the slip displacement or slip velocity increases. In cases where the frictional strength decreases with sliding speed (velocity weakening), questions of well-posedness and stability of sliding bear striking resemblance to the bimaterial case discussed above. For example, when the velocity-weakening frictional law does not feature any history dependence the problem of periodic perturbations is well-posed (solutions can be found) while these perturbations are unstable, with an instability rate proportional to the wave number, provided that the rate of velocity weakening is stronger than the critical level. They are neutrally stable or stable otherwise. For strong enough velocity weakening, however, the problem is ill-posed (no solution exists) for sliding involving isolated (or generic) self-healing pulses and the associated numerical problems of pulse splitting still remain an issue. As in the case of bimaterial sliding, the introduction of history dependence in the form of rate and state frictional laws provides regularization but does not necessarily guarantee stability (i.e. individual pulses that do not split up can be found but may still

grow with time). Perrin, Rice and Zheng 1995 and Zheng and Rice 1998 found from 2-D antiplane (mode-III) calculations that a well-posed solution to the problem of propagation of a self-healing rupture pulse in a homogeneous fault requires frictional constitutive laws that include healing in stationary contact augmented by strong dependency of friction on slip velocity, and other, loading, rupture and fault conditions. They also found that under certain conditions, which depend, among other things, on the rate of steady-state velocity weakening and on the loading, rupture can be partially crack-like and partially pulse-like, whereas under other conditions rupture may still propagate as a classically expanding crack. Ben-Zion and Huang 2002 numerically studied a configuration of two identical solids separated by a fault zone layer at the limiting case, where the layer is of zero width. They assumed constant external compressive and shear fields. They showed that the friction law used by Ranjith and Rice 2001 and Cochard and Rice 2000 regularizes the Adams instability as it does with the dissimilar materials. The same conclusion was reached analytically by Rice, Lapusta and Ranjith 2001.

Sliding propagation speeds

The issue of limiting propagation speeds arises in the dynamic fracture mechanics of growing shear cracks (Freund 1990; Broberg 1999; Rosakis 2002), which has many similarities to the frictional sliding process. These theories treat the rupture front as a distinct point (sharp-tip crack). The crack-like rupture of coherent interfaces, separated by similar and dissimilar solids subjected to dynamic shear loading, has been the subject of extensive experimental, numerical and analytical investigations in the past years and has been summarized by Rosakis 2002 in a recent review. Intersonic shear rupture in coherent

interfaces occurs persistently in bimaterial systems and in homogeneous structures which feature interfaces. The first experimental observations of intersonically traveling cracks were made in connection with crack propagation along the interface of bimaterial systems (Tippur and Rosakis 1991; Liu, Lambros and Rosakis 1993; Lambros and Rosakis 1995, Singh and Shukla 1996; Rosakis, Samudrala, Singh and Shukla 1998; Kavaturu, Shukla and Rosakis 1998). Intersonic crack propagation in homogeneous systems was first observed experimentally by Rosakis, Samudrala and Coker 1999 and by Coker and Rosakis 2001 and has been numerically modeled by Needleman 1999 using the cohesive element methodology and by Hao, Wing, Klein and Rosakis 2004 using a mesh-free finite element methodology. A special rupture speed of $\sqrt{2}\,c_S$ as the speed separating regions of unstable and stable intersonic shear crack growth has also been identified (Burridge, Conn and Freund 1979; Freund 1979; Samudrala, Huang and Rosakis 2002(a, b)). Atomistic models of intersonic shear rupture (Abraham and Gao 2000; Abraham 2001; Gao, Huang and Abraham 2001) as well as field observations of intersonic rupture events during recent large crustal earthquakes (Archuleta 1984; Olsen, Madariaga and Archuleta 1997; Hernandez, Cotton and Campillo 1999; Bouchon et al. 2001; Lin et al. 2002; Bouchon and Vallee 2003; Ellsworth et al. 2004; Xia, Rosakis and Kanamori 2004; Xia, Rosakis, Kanamori and Rice 2005) have demonstrated the remarkable length scale persistence (over eleven orders of magnitude) of intersonic rupture phenomena and of the main features observed in laboratory experiments and in continuum theory.

Wrinkle-like pulses

The possibility of generating wrinkle-like pulses in incoherent frictionless contact between two dissimilar solids, when separation does not occur, was first investigated by Achenbach and Epstein 1967. These "smooth contact Stonely waves" (also known as slip waves or generalized Rayleigh waves) are qualitatively similar to those of bonded contact (Stonely waves) and occur for a wider range of material combinations. Comninou and Dundurs 1977 found that self-sustained slip waves with interface separation (detachment waves or wrinkle-like slip pulses) can propagate along the interface of two similar or different solids which are pressed together. The constant propagation speed of these waves was found to be between the Rayleigh wave speed and the shear wave speed of the slowest material. Weertman 1980 obtained a 2D self-sustained wrinkle-like slip pulse propagating at the generalized Rayleigh wave speed along a bimaterial interface governed by Coulomb friction when the remote shear stress was less than the frictional strength of the interface. Finite-difference calculations of Andrews and Ben-Zion 1997 show the propagation of wrinkle-like pulses along a bimaterial interface governed by Coulomb friction. Particle displacement in a direction perpendicular to the fault is much greater in the slower material than in the faster material, resulting in a separation of the interface during the passage of the slip pulse. Anooshehpoor and Brune 1999 discovered such waves in rubber sliding experiments (using a bimaterial system consisting of two rubber blocks with different wave speeds). The above-mentioned detachment waves are radically different from the Schallamach waves (Schallamach 1971) which propagate very slowly compared to the wave speeds of the solid.

Summary

As we see, there is a debate about the different high-rate phenomena that occur at the incoherent interface of two half-planes during frictional sliding and there are not enough experimental studies so far which would help to analyze the problem. Indeed, the majority of the existing experimental studies concentrate on processes occurring over large time scales (large compared to wave transit within the specimen) and they are concerned with developing qualitative and/or quantitative relationships between time-averaged friction data and various governing parameters. Unfortunately, most dynamic friction laws obtained using various experimental configurations and apparati lack the reproducibility of friction data (survey by Ibrahim 1994) to be of definite value to the theorists. The results of these experiments are multi-branched friction versus slip velocity curves, which even for the same material and the same experimental configuration depend not only on the properties of the frictional interface but also on the dynamic properties of the apparatus, such as mass, stiffness and damping. This suggests that the friction data obtained in the course of stick-slip motions do not purely reflect the intrinsic properties of the surfaces in contact but are also greatly affected by several of the dynamic variables involved in each particular experimental setup. Another shortcoming of most experiments is the achievable range of sliding speeds, (on the order of $1 \mu m / s$). An exception to this rule are the experiments of Prakash and Clifton 1993 and of Prakash 1998, who employed a plate-impact pressure-shear friction configuration to investigate the dynamic sliding response of an incoherent interface in the microsecond time-scale (sliding speeds on the order of $10 m / s$). The experimental results, deduced from the response to step changes imposed on the normal

pressure at the frictional interface, reinforce the importance of including frictional memory in the development of the rate-dependent state variable friction models. However, this setup is not able to provide information about the stress field developed in the specimen nor to shed light on the interfacial process during dynamic sliding. As in the cases described above, the implicit assumption crucial to the interpretation of the data is both stress and sliding process uniformity. Finally, the scarcity of fast sliding velocity data in the open literature has to be emphasized. We believe that this is an essential data set which could be proven as the ultimate arbitrator for the various dynamic sliding models and friction laws.

The purpose of this work is to study the dynamic sliding process along incoherent (frictional) interfaces in the microsecond time scale. A bimaterial system comprised of Homalite and steel plates and a homogeneous system consisting of two Homalite plates are considered. The plates are held together by a static uniform compressive pre-stress while dynamic sliding is initiated by asymmetric impact. The evolution of the maximum shear stress contours is recorded by high-speed photography in conjunction with dynamic photoelasticity. A newly-developed technique based on laser interferometry is employed to measure the sliding velocity at discrete points along the interface. The combination of the classic full-field technique of photoelasticity with the local technique of velocimetry is proven to be a very powerful tool in the investigation of dynamic sliding.

The response of the Homalite-steel bimaterial system differs according to whether the impact loading is applied to the Homalite plate or to the steel plate. In the first case, the

interaction between the impact wave and the preexisting static field causes the generation of a relatively broad eye-like fringe formation emanating from the interface behind the P-wave front. A disturbance traveling at the interface at a constant speed close to the Rayleigh wave speed of steel, which is higher than the P-wave speed of Homalite, generates a shear Mach line crossing the P-wave front and the eye-like fringe structure. Velocimetry reveals that sliding initiates behind the eye-like fringe pattern. A second shear Mach line, originating from the sliding tip, appears in the photoelastic images, indicating that the sliding is supershear with respect to the shear wave speed of Homalite. A self-sustaining wrinkle-like pulse, propagating along the bimaterial interface at a constant speed between the Rayleigh wave and the shear wave speed of Homalite, is observed. When the impact load is applied to steel plate, then the data acquired by the velocimeter are the only useful source of information. Analysis of these data shows that sliding at a given point initiates with the arrival of the P-wave front there.

In the case of the bimaterial structure (Homalite-steel), sliding occurs always in a crack-like mode. In the case of a homogeneous system of Homalite plates, however, direct physical evidence of different modes of sliding is recorded. Crack-like sliding, pulse-like sliding and mixed mode sliding in the form of pulses followed by a crack are discovered. A relatively broad loading wave emanating from the interface and caused by the interference between the impact wave and the preexisting static stress field appears. The propagation speeds of the sliding tips are not dependent on the confining stress but only on the projectile speed. They span almost the whole interval from sub-Rayleigh speeds to nearly the sonic speed of the material, with the exception of a forbidden gap between the Rayleigh wave speed and

the shear wave speed. Supersonic trailing pulses are also recorded. Mach lines with different inclinations emanating from the sliding zone tips are discovered. Behind the sliding tip, wrinkle-like pulses are developed for a wide range of impact speeds and confining stresses. They always travel at speeds between the Rayleigh wave speed and the shear wave speed of Homalite.

REFERENCES

Abraham, F. F. & Gao, H. J. How fast can cracks propagate? *Phys. Rev. Letters* **84**, 3113-3116 (2000).

Abraham, F. F. The atomic dynamics of fracture. *J. Mech. and Phys. of Solids* **49**, 2095-2111 (2001).

Achenbach, J. D. & Epstein, H. I. Dynamic interaction of a layer and a half-space. *J. Eng. Mechanics* **5**, 27-42 (1967).

Adams, G. Self-excited oscillations of two elastic half-spaces sliding with a constant coefficient of friction. *J. Appl. Mechanics* **62**, 867-872 (1995).

Aki, K. Characterization of barriers on an earthquake fault. *J. Geophys. Res.* **84**, 6,140-148 (1979).

Andrews, D. J. & Ben-Zion, Y. Wrinkle-like slip pulse on a fault between different materials. *J. Geophys. Res.* **102**, 553-571 (1997).

Andrews , D. J. Rupture propagation with finite stress in antiplane strain. *J. Geophys. Res.* **81**, 3575-3582 (1976).

Andrews, D. J. Dynamic plane-strain shear rupture with a slip-weakening friction law calculated by a boundary integral method. *Bull. Seismol. Soc. America* **75**, 1-21 (1985).

Anooshehpoor, A. & Brune, J. N. Wrinkle-like Weertman pulse at the interface between two blocks of foam rubber with different velocities. *Geophysical Research Letters* **23**, 2025-2028 (1999).

Archuleta, R. J. A faulting model for the 1979 Imperial Valley earthquake. *J. Geophys. Res.* **89**, 4559-4585 (1984).

Beeler, N. M. & Tullis, T. E. Self-healing slip pulses in dynamic rupture models due to velocity-dependent strength. *Bull. Seismol. Soc. America* **86**, 1130-1148 (1996).

Ben-Zion, Y. & Rice, J. R. Dynamic simulations of slip on a smooth fault in an elastic solid. *J. Geophys. Res.* **102**, 17,771-17,784 (1997).

Ben-Zion, Y., & Andrews, D. J. Properties and implications of dynamic rupture along a material interface. *Bull. Seismol. Soc. Amer.* **88**, 1085-1094 (1998).

Ben-Zion, Y., & Huang, Y. Dynamic rupture on an interface between a compliant fault zone layer and a stiffer surrounding solid. *J. Geophys. Res.* **107**, B2, 10.1029/2001JB000254 (2002).

Bouchon, M., Bouin, M. P., Karabulut, H., Toksoez, M. N., Dietrich, M. & Rosakis, A. J. How fast is rupture during an earthquake? New sights from the 1999 Turkey earthquakes. *Geophysical Research Letters* **28**, 2723-2726 (2001).

Bouchon, M. & Vallee, M. Observation of long supershear rupture during the magnitude 8.1 Kunlunshan earthquake. *Science* **301**, 824-826 (2003).

Broberg, K. B. *Cracks and fracture* (Academic Press, London, 1999).

Brune, J. N. The physics of earthquake strong motion. *Seismic Risk and Engineering Decisions* (ed. Lomnitz, C. & Rosenbluth, E.) 141-171 (Elsevier, New York, 1976).

Burridge, R., Conn, G. & Freund, L. B. The stability of rapid mode II shear crack with finite cohesive traction. *J. Geophys. Res.* **84**, 2210-2222 (1979).

Cochard, A. & Madariaga, R. Dynamic faulting under rate-dependent friction. *Pure Appl. Geophys.* **142**, 419-445 (1994).

Cochard, A. & Madariaga, R. Complexity of seismicity due to highly rate-dependent friction. *J. Geophys. Res.* **105**, 25891-25907 (1996).

Cochard, A. & Rice, J. R. Fault rupture between dissimilar materials: Ill-posedness, regularization, and slip-pulse response. *J. Geophys. Res.* **105**, 25891-25907 (2000).

Coker, D. & Rosakis, A. J. Experimental observations of intersonic crack growth in asymmetrically loaded unidirectional composite plates. *Philosophical Magazine A* **81**, 571-595 (2001).

Coker, D., Lykotrafitis, G., Needleman, A. & Rosakis, A. J. Frictional sliding modes along an interface between identical elastic plates subject to shear impact loading. *J. Mech. and Phys. of Solids*. **53**, 884-922 (2005).

Comninou, M. and Dundurs, J. Elastic interface waves involving separation. *Journal of Applied Mechanics, ASME* **44**, 222-226 (1977).

Das, S. & Aki, K. A numerical study of two-dimensional spontaneous rupture propagation. *Geophys. J. Royal Astron. Soc.* **50**, 643-668 (1977).

Day, S. M. Three-dimensional finite difference simulation of fault dynamics: rectangular faults with fixed rupture velocity. *Bull. Seismol. Soc. America* **72**, 705-727 (1982).

Dieterich, J. H. Modeling of rock friction 1. Experimental results and constitutive equations. *J. Geophys. Res.* **84**, 2161-2168 (1979).

Ellsworth, W. L., Celebi, M., Evans, J. R., Jensen, E. G., Kayen, R., Metz, M. C., Nyman, D. J., Roddick, J. W., Spudich, P. & Stephens, C. D. Near-field ground motion of the 2002 Denali fault, Alaska, earthquake recorded at pump station 10. *Earthquake Spectra* **20**, 597-615 (2004).

Freund, L. B. The mechanics of dynamic shear crack propagation. *J. Geophys. Res.* **84**, 2199-2209 (1979).

Freund, L. B. *Dynamic fracture mechanics* (Cambridge University Press, Cambridge, UK, 1990).

Gao, H. J., Huang, Y. & Abraham, F. F. Continuum and atomistic studies of intersonic crack propagation. *J. Mech. and Phys. of Solids* **49**, 2113-2132 (2001).

Hao, S., Wing, K. L., Klein, P. A., & Rosakis, A. J. Modeling and simulation of intersonic crack growth. *Int. J. Sol. and Struct.* **41**, 1773-1799 (2004).

Harris R. A. & Day, S. M. Dynamics of fault interactions: parallel strike-slip faults. *J. Geophys. Res.* **98**, 4461-4472 (1993).

Hartzell, S. H. & Heaton, T. H. Inversion of strong ground motion and teleseismic waveform data for the fault rupture history of the 1979 Imperial Valley, California, earthquake. *Bull. Seismol. Soc. America* **73**, 1553-1583 (1983).

Heaton, T. H. The 1971 San Fernando earthquake; a double event? *Bull. Seismol. Soc. America* **72**, 2037-2062 (1982).

Heaton, T. H. Evidence for and implications of self-healing pulses of slip in earthquake rupture. *Phys. Earth Planet. In.* **64**, 1-20 (1990).

Hernandez, B., Cotton, F. & Campillo, M. Contribution of radar interferometry to a two-step inversion of the kinematic process of the 1992 Landers earthquake. *J. Geophys. Res.* **104**, 13083-13099 (1999).

Ibrahim, R. A. Friction-induced vibration, chatter, squeal, and chaos, Part I: Mechanics of contact and friction. *Applied Mechanics Reviews, ASME* **47**, 209-226 (1994).

Johnson, E. On the initiation of unidirectional slip. *Geophys. J. Int.* **101**, 125-132 (1990).

Kavaturu, M., Shukla, A. & Rosakis, A. J. Intersonic crack propagation and interfaces: experimental observations and analysis. *Experimental Mechanics* **38**, 218-225 (1998).

Lambros, J. & Rosakis, A. J. Shear dominated transonic interfacial crack growth in a bimaterial-I. Experimental observations. *J. Mech. and Phys. of Solids* **43**, 169-188 (1995).

Lapusta, N., Rice, J. R., Ben-Zion, Y. & Zheng, G. Elastodynamic analysis for slow tectonic loading with spontaneous rupture episodes on faults with rate- and state-dependent friction. *J. Geophys. Res.* **105**, 23,765-23,789 (2000).

Lapusta, N. Proceedings. SEM, Portland (2005).

Lin, A., Guo, J., Zeng, Q., Dang, G., He, W. & Zhao, Y. Co-seismic strike-slip and rupture length produced by the 2001 M_s 8.1 central Kunlun earthquake. *Science* **296**, 2015-2017 (2002).

Linker, M. F. & Dieterich, J. H. Effects of variable normal stress on rock friction: Observations and constitutive equations. *J. Geophys. Res.* **97**, 4923-4940 (1992).

Liu, C., Lambros, J. & Rosakis, A. J. Highly transient elastodynamic crack growth in a bimaterial interface: Higher order asymptotic analysis and optical experiments. *J. Mech. and Phys. of Solids* **41**, 1857-1954 (1993).

Liu, H. L. & Helmberger, D. V. The near-source ground motion of the 6 August 1979 Coyote Lake, California, earthquake. *Bull. Seismol. Soc. America* **73**, 201-218 (1983).

Madariaga, R. Dynamics of an expanding circular fault. *Bull. Seismol. Soc. America* **66**, 639-666 (1976).

Mendoza, C. & Hartzell, S. H. Inversion for slip distribution using GDSN P waves: North Palm Springs, Borah peak, and Michoacan earthquakes. *Bull. Seismol. Soc. America* **78**, 1092-1111 (1988).

Mendoza, C. & Hartzell, S. H. Slip distribution of 19 September 1985 Michoacan, Mexico, earthquake: Near-source and teleseismic constraints. *Bull. Seismol. Soc. America* **79**, 655-669 (1989).

Needleman, A. An analysis of intersonic crack growth under shear loading. *ASME, J. Appl. Mech.* **66**, 847-857 (1999).

Nielsen, S. B., Carlson, J. M. & Olsen, K. B. Influence of friction and fault geometry on earthquake rupture. *J. Geophys. Res.* **105**, 6069-6088 (2000).

Nielsen, S. & Madariaga, R. On the self-healing fracture mode. *Bulletin of The Seismological Society of America* **93**, 2375-2388 (2003).

Olsen, K. B., Madariaga, R. & Archuleta, R. J. Three-dimensional dynamic simulation of the 1992 Landers earthquake. *Science* **278**, 834-838 (1997).

Papageorgiou, A. & Aki, K. A specific barrier model for the quantitative description of inhomogeneous faulting and the prediction of strong ground motion. I. Description of the model. *Bull. Seismol. Soc. America* **73**, 693-722 (1983a).

Papageorgiou, A. & Aki, K. A specific barrier model for the quantitative description of inhomogeneous faulting and the prediction of strong ground motion. II. Applications of the model. *Bull. Seismol. Soc. America* **73**, 953-978 (1983b).

Pelton, J. R., Meissner, C. W. & Smith K.D. Eyewitness account of normal surface faulting. *Bull. Seismol. Soc. America* **74**, 1083-1089 (1984).

Perrin, G. Rice, J. R. & Zheng, G. Self-healing slip pulse on a frictional surface. *J. Mech. Phys. Solids* **43**, 1461-1495 (1995).

Prakash, V. & Clifton, R. J. Pressure-shear plate impact measurement of dynamic friction for high speed machining applications. *Proceedings of the 7th International Congress on Experimental Mechanics,* Society of Experimental Mechanics, Bechtel, CT, 556-564 (1993).

Prakash, V. Frictional response of sliding interfaces subjected to time varying normal pressures. *Journal of Tribology, ASME* **120**, 97-102 (1998).

Ranjith, K. & Rice, J. R. Slip dynamics at an interface between dissimilar materials. *J. Mech. and Phys. of Solids* **49**, 341-361 (2001).

Renardy, M. Ill-posedness at the boundary for elastic solids sliding under Coulomb friction. J. Elasticity **27**, 281-287 (1992).

Rice, J. R. and Ruina, A. L. Stability of frictional sliding. *Journal of Applied Mechanics* **50**, 343-349 (1983).

Rice, J. R., Lapusta, N. & Ranjith, K. Rate and state dependent friction and the stability of sliding between elastically deformable solids. *J. Mech. and Phys. of Solids* **49**, 1865-1898 (2001).

Rice, J. R. Mechanics for a New Millennium. in *Proceedings of the 20th International Congress of Theoretical and Applied Mechanics, 2000, Chicago* (ed. Aref, H. & Philips, J. W.) 1- 23 (Kluwer Academic Publishers, Dordrecht, 2001).

Rosakis, A. J., Samudrala, O., Singh, R. P. & Shuckla, A. Intersonic crack propagation in bimaterial systems. *J. Mech. and Phys. of Solids* **46**, 1789-1813 (1998).

Rosakis, A. J., Samudrala, O. & Coker, D. Cracks faster than the shear wave speed. *Science* **284**, 1337-1340 (1999).

Rosakis, A. J. Intersonic shear cracks and fault ruptures. *Advances in Physics* **51**, 1189-1257 (2002).

Ruina, A. L. Slip instability and state variable friction laws. *J. Geophys. Res.* **88**, 10359-10370 (1983).

Ruppert, S. D. & Yomogida, K. A crack-like rupture model for the 19 September 1985 Michoacan, Mexico, earthquake. *Pure and Appl. Geophys.* **138**, 407-427 (1992).

Samudrala, O., Huang, Y. & Rosakis, A. J. Subsonic and intersonic shear rupture of weak planes with a velocity weakening cohesive zone. *J. Geophys. Res.* **107**, No B8, 10129/2001JB000460 (2002a).

Samudrala, O., Huang, Y. & Rosakis, A. J. Subsonic and intersonic mode II crack propagation with a rate-dependent cohesive zone. *J. Mech. and Phys. of Solids* **50**, 1231-1268 (2002b).

Schallamach, A. How does rubber slide? *Wear* **17**, 301-312 (1971).

Singh, P. R. & Shukla, A. Subsonic and transonic crack growth along a bimaterial interface. *Journal of Applied Mechanics* **63**, 919-924 (1996).

Tippur, H. V. & Rosakis, A. J. Quasi-static and dynamic crack growth along bimaterial interfaces: a note on crack-tip field measurements using coherent gradient sensing. *Experimental Mechanics* **31**, 243-251 (1991).

Wallace, R. E. Eyewitness account of surface fault during the earthquake of 28 October 1983 Borah peak, Idaho. *Bull. Seismol. Soc. America* **74**, 1091-1094 (1983).

Weertman, J. Unstable slippage across a fault that separates elastic media of different elastic constants. *J. Geophys. Res.* **85**, 1455-1461 (1980).

Xia, K., Rosakis, A. J. & Kanamori, H. Laboratory earthquakes: The sub-Rayleigh-to-supershear rupture transition. *Science* **303**, 1859-1861 (2004).

Xia, K. W., Rosakis A. J., Kanamori H. & Rice J. R. Inhomogeneous faults hosting earthquakes in the laboratory: directionality and supershear. *Science **308***, 681-684 (2005).

Zheng, G. & Rice, J. R. Conditions under which velocity-weakening friction allows a self-healing versus a crack-like mode of rupture. *Bull. Seismol. Soc. America* **88**, 1466-1483 (1998).

Chapter 2

EXPERIMENTAL METHODS

2.1 Introduction

The purpose of this chapter is to provide a clear picture of the experimental procedures followed in order to address the subject of frictional sliding. The materials, the specimen configuration, the loading devices and the experimental setup employed in this investigation are described in detail. The time evolution of the dynamic stress field in the bulk was recorded by high-speed digital photography in conjunction with dynamic photoelasticity. A newly developed technique, based on laser interferometry, was employed to locally measure the horizontal and vertical components of the in-plane particle velocity. The above technique is presented in detail and its reliability is tested extensively. The methodology employed for the measurement of the local sliding velocity by using two independent velocimeters is demonstrated. We also describe the setup for the simultaneous measurements of the in-plane horizontal and vertical components of the particle velocity. The combination of the full-field technique of photoelasticity with the local technique of velocimetry will be proven to be a very powerful tool in the study of dynamic sliding.

2.2 Materials and Specimen Configuration

Experiments were performed to investigate the nature of dynamic frictional sliding along the incoherent interface of two plates made of identical material and along the interface of a high-contrast bimaterial system as well. In the case of identical plates, the material used

was Homalite-100, whereas in the case of a bimaterial system, the specimen consisted of a Homalite-100 plate and a steel plate. In both cases, the plates were held together by a uniform compressive stress (see Figure 1). Homalite-100 is a mildly rate-sensitive brittle polyester resin that exhibits stress-induced birefringence with an optical coefficient $F_\sigma = 22.6\,KN/m$. At the strain rate developed during the experiments (on the order of $10^3\,s^{-1}$) and at room temperature, Homalite exhibits a purely linear elastic behavior. The longitudinal, shear and Rayleigh wave speeds in Homalite are $C_1^H = 2583\,m/s$, $C_2^H = 1249\,m/s$ and $C_R^H = 1155\,m/s$ respectively. Steel was chosen as the other half of the bimaterial system because it provides a strong material property mismatch across the interface, similar to mismatches encountered in composites. The dilatational, shear and Rayleigh wave speeds in steel are $C_1^S = 5838\,m/s$, $C_2^S = 3227\,m/s$ and $C_R^S = 2983\,m/s$ respectively. The wave speeds for Homalite and steel were obtained by ultrasonic measurements using shear and pressure transducers operating at $5\,MHz$.

In the experiments, the configuration was approximated by plane stress conditions, since plate specimens $76.2\,mm$ high, $139.7\,mm$ long and $9.525\,mm$ thick were employed. The shear wave speeds are identical in 3-D and for the plane stress approximation. The same is true for the Rayleigh wave speed, since the contribution in the Rayleigh wave formation comes primarily from the shear wave. However, the plane stress longitudinal wave speeds of Homalite-100 and steel are $C_{1\sigma}^H = 2187\,m/s$, $C_{1\sigma}^S = 5378\,m/s$ respectively.

2.3 Experimental Setup and Procedure

A compressive stress was applied with a press calibrated using a load cell. The asymmetric impact loading was imposed via a cylindrical steel projectile with a diameter of $25\,mm$ and a length of $51\,mm$, fired by a gas gun. A steel buffer $73\,mm$ high, $25.4\,mm$ long and $9.525\,mm$ thick was attached to the impact side of the Homalite plate to prevent shattering and to induce a more or less planar loading wave (Figure 1).

2.3.1 Dynamic Photoelasticity Setup

Dynamic photoelasticity is a classical full-field technique, which visualizes the contours of maximum shear stress in the bulk of a birefringent plate (Frocht 1962; Durelli and Riley 1965; Dally and Riley 1978). A typical experimental setup for dynamic photoelasticity experiments is shown in Figure 2. The optical setup was arranged for a light field. Isochromatic fringes are contours of maximum in-plane shear stress $\tau_{\max}$ governed by the stress optical law

$$2\tau_{\max} = \sigma_1 - \sigma_2 = N\, F_\sigma / h$$

where F_σ is the material's stress optical coefficient, h is the specimen thickness, σ_1, σ_2 are the principal stresses and $N = n + 1/2$ (with $n = 0,1,2,..$) is the isochromatic fringe order. A continuous laser was used as the light source in our experiments. The laser was set to operate on a single wave length of $540\,nm$ (green light). It emitted an intense beam $2\,mm$ in diameter and 100:1 vertically polarized. The laser beam first passed through a

quarter wave plate, which transformed it into a circular polarized beam. Then it passed through a $6\mu m$ pinhole and a collimator lens. Finally, the coherent monochromatic circular polarized light went through a collimator lens and expanded in a uniform laser beam of $130\,mm$ diameter. The laser beam was transmitted through the specimen and an analyzer. The resulting photoelastic fringe pattern was recorded with a high-speed digital camera (Cordin model 220), which is able to record 16 distinct frames at framing rates up to 100 million frames per second. In this experimental work, most of the high-speed photography was performed at 250,000 to 1,000,000 frames per second. The field of view was wide enough to cover most of the specimen.

2.3.2 Sliding Velocity Measurement Setup

The local sliding velocity was obtained as follows. A pair of fiber-optic velocimeters measured the horizontal particle velocities at two adjacent points across the interface. The horizontal relative velocity history was obtained by subtracting the velocity of the lower plate point from the velocity of the upper plate point. A schematic representation of the setup is shown in Figure 3(a) for the case of a bimaterial specimen. The same setup was also employed in the case of identical Homalite plates. The laser beams emitted from the velocimeter heads were focused on points M_1 and M_2 on the thin vertical surfaces of the reflective membranes, which were attached to the surfaces of the Homalite (top) and steel (bottom) plates respectively. The distance of each point from the interface was less than $250\mu m$ before compression, and both points had the same horizontal distance from the impact side of the Homalite plates. A picture of the actual setup is presented in Figure 3(b).

The velocimeter and its use in measuring the in-plane components of a particle velocity are described in detail in the next section.

2.3.3 Simultaneous Measurement of the Horizontal and Vertical Components of the Velocity

By using two velocimeters, we can of course measure not only the horizontal component of the in-plane velocity, but the vertical component as well. For this, the laser beam is aimed perpendicular to the narrow horizontal surface of the reflective membrane. Preliminary experimental results showed that the velocities in steel plate (in bimaterial specimen) are one order of magnitude lower than the velocities in Homalite plate. Taking advantage of this fact, we assumed that the particle velocities in the steel plate were negligible and we carried out several tests using the two velocimeters we had at our disposal to record both the horizontal and vertical in-plane particle velocities. These were subsequently interpreted as sliding and opening speeds respectively. A schematic of the setup used for the measurement is shown in Figure 4.

2.4 Background Experimental Work

As described previously, the slip velocity measurement involved a pair of independent fiber-optic velocimeters that continuously measured the horizontal particle velocities at two adjacent points across the interface. By subtracting the velocity of the point below the interface from that of the point above the interface, the horizontal relative velocity history was obtained. Since this is the first time the technique of the in-plane relative velocity measurement is presented, different issues that emerged during its development are

addressed. We start by describing a relatively simple yet very accurate method to measure the in-plane and the out-of-plane components of the velocity at one point in the top plane. A point worth noting is that there have been only a few attempts to obtain in-plane particle velocities associated with classical fracture mechanics (Sharpe 1971; Abou-Sayed, Clifton and Hermann 1976; Kim, Clifton and Kumar 1977; Sharpe, Payne and Smith 1978; Lu, Suresh and Ravichandran 1998.

2.4.1 Particle Velocity Measurement Setup

A velocimeter was used to measure the horizontal and vertical in-plane components of the particle velocity as well as the out-of-plane velocity component. The velocimeter is composed of a modified Mach-Zehnder heterodyne interferometer (Polytec, OFV-511) and a velocity decoder (Polytec, OFV-5000) (see Figure 5). The interferometer combines the reference beam, which undergoes modulation through a Bragg cell, with the reflected beam from the surface point where the particle velocity is measured. From the interference of these two beams, the decoder gives the component of the velocity along the direction of the laser beam. The decoder was set to a full range scale of $\pm 10 m/s$ with a maximum frequency of $1.5 MHz$ and a maximum acceleration of $10^7 g$. The beam spot size was approximately $70 \mu m$, whereas the error of the velocity measurements was 1%.

Figure 6 shows how the different components of the particle velocity were measured. A reflective membrane $360 \mu m$ thick was attached to the surface. For the measurement of the out-of-plane component of the particle velocity, the velocimeter laser beam had to be perpendicular to the surface of the reflective membrane at the measurement position (beam

3 in Figure 6 focused at C). For the measurement of the in-plane horizontal component of the velocity, the laser beam had to be horizontal, parallel to the specimen surface, and focused on the vertical lateral surface of the membrane (beam 1 in Figure 3 focused at A). The vertical component of the velocity was measured by the vertical beam (beam 2 in Figure 6 focused at B) which was perpendicular to the horizontal lateral surface of the membrane. The reflective membrane consisted of small glass spheres (approximately 50 μm in diameter) that were glued with an elastic epoxy to the plate surface. Each sphere acts as a small "cat's-eye", scattering light back along the path of the incident beam. As the laser beam usually hits several glass beads at one time, each of the beams can interfere with each other and produce a speckle pattern. If the focused spot is very small, as it was in the presenting experiments, the number of scattering centers is small and the angular dependence of the path length differences in a given direction is also small. This leads to a large solid angle over which the interference condition is reasonably constant and the speckle noise is small. In the experiments, the deviation of the laser beams from the normal direction to the corresponding membrane surface was approximately 2^o to 3^o, and an excellent quality signal was received from the velocimeter. This amount of deviation angle did not affect the results, as we demonstrate below.

2.4.2 Reliability of the Proposed Technique

As was already mentioned, two independent velocimeters were employed in the experiments. We had to verify that both instruments were calibrated and would consequently give the same result when they simultaneously measured the velocity at the same point. To this end, we performed the following experiment. A reflective membrane

was attached to the side S_1 of the upper Homalite plate (see Figure 7) and a uniform compressive stress of $10MPa$ was applied to the specimen. Both velocimeters were focused at essentially the same point on the membrane, at $10mm$ from the interface. A projectile hit the buffer at a speed of $13m/s$. The diagram in Figure 8(a) depicts the variation of the horizontal velocity at a point measured by the two different velocimeters. As we can see, both measurements are almost identical. A magnification of the area of the diagram in Figure 8(a), which is designated by a dotted line, is shown in Figure 8(b). Only after the velocity reached the value $10m/s$ (the saturation level of the device) did a very small difference (on the order of 1%) appear between the two recordings. We note that when the velocity decreased, the devices once more gave identical results.

Another issue to be clarified is the following. The velocimeter measures the component of the velocity of a point at the thin lateral surface of the reflective membrane along the direction of the laser beam. In order to prove that the velocity of the point on the membrane and the velocity of the corresponding point on the plate were the same, the following comparison was performed. Two reflective membranes were attached to the edge of the Homalite plate, on the side opposite the impact position (see Figure 9(a)). One was attached to the narrow surface S_1, which was perpendicular to the direction of the impact, and the second membrane was attached to the lateral surface S_2, which was parallel to the direction of impact. The horizontal particle velocities were measured at points A and B. The distance between these two points was approximately $2mm$. The laser beam that was focused at A was vertical to the large membrane surface, and the out-of-plane velocity with respect to plane S_1 was measured. This is the most favorable arrangement for the instrument, since it

has been designed to measure the out-of-plane velocities. We note that the above measurement gives the velocity of a point on the plate. The laser beam focused on B was vertical to the narrow surface of the membrane, and it measured the horizontal in-plane component of the velocity at point B of the membrane. Since point A was very close to point B, we can argue that their velocities should also be very similar. The confining pressure was $10\,MPa$ and the impact speed $11\,m/s$. In Figure 9(b), the velocity histories of both points A and B are shown. In this case the distance from the measurement points to the interface was $d = 5\,mm$, and both instruments gave almost identical results. The wave front arrived at the measurement points simultaneously at around $100\,\mu s$. The particle velocity increased until it reached a maximum value of approximately $7\,m/s$, and then it decelerated. Since the devices gave very similar results, we can safely argue that the point on the membrane had the same speed as the most adjacent point on the plate's surface. Thus, we conclude that the procedure we followed for the measurement of the in-plane component of the velocity was accurate.

The final subject for investigation is the following. In order to measure the horizontal component of the particle velocity at a point on the surface, the laser beam had to be horizontal and parallel to the plate surface. The maximum difference between the height of the velocimeters' heads and the height of the point of reflection was less than $2.5\,mm$. It is also noted that the velocimeters' heads were at a distance of about $300\,mm$ from the side of the reflective membrane. A difference in height of $2.5\,mm$ resulted in a deviation angle from the horizontal direction of less than 0.5^o. This small deviation did not affect our

measurements, since the error from the projection of the velocity on the laser beam is two orders of magnitude less than the intrinsic error of the velocimeter, which is 1%. Although the deviation from the horizontal direction was very small, we were sometimes forced to move the velocimeter head a small distance out of the vertical plane of the specimen in order to have a good quality signal. The maximum angle was 2.5^o, and in order to be sure that this lateral deviation did not affect the results, the following experiment was performed. A uniform compressive stress $10MPa$ was applied on a bimaterial (Homalite-steel) specimen. A reflective membrane was attached to the surface of the Homalite plate. Two independent velocimeters were pointed at essentially the same point A on the reflective membrane, but in different angles with respect to the vertical plane (see Figure 10(a)). Point A was at a distance of $70mm$ from the impact side of the Homalite plate and $25mm$ from the interface. One laser beam formed an angle of approximately 1^o with the vertical plane, and the other laser beam formed an angle of approximately 5^o. The distance of the velocimeter head from the measurement point was approximately $300mm$. A projectile hit the buffer at a speed of $9.5m/s$. The diagram in Figure 10(b) illustrates the variation of the component of the horizontal particle velocity at A along the directions of the laser beams of the two different velocimeters. Both measurements were almost identical, and we conclude that even a 5^o deviation angle from the vertical plane did not affect the result. It is noted that 5^o is a very large deviation angle since it corresponds to a $25mm$ translation of the velocimeter head out of the plane of the Homalite plate, and it never happened during the frictional sliding experiments. After the

above tests, we concluded that the experimental error, due to small misalignments of the laser beam, was smaller than the inherent velocimeter error of 1% .

The results of the above investigation demonstrate that the measurement technique can be used with confidence to record, in real time, the in-plane components of the particle velocity on the surface of a plate.

REFERENCES

Abou-Sayed, A. S., Clifton, R. J. & Hermann, L. The Oblique-plate impact experiment. *Experimental Mechanics* **16**, 127-132 (1976).

Dally, J. W. & Riley, W. F. *Experimental stress analysis* (McGraw-Hill, New York, N.Y. 1978)

Durelli, A. J. & Riley, W. F. *Introduction to photomechanics* (Prentice-Hall, Englewood Cliffs, N.J. 1965)

Frocht, M. M. *Photoelasticity* (John Wiley & Sons, London, 1962)

Kim, K-S, Clifton, R. J. & Kumar, P. A combined normal- and transverse-displacement interferometer with an application to impact of y-cut quartz. *J. Appl. Phys.* **48**, 4132-4139 (1977).

Lu, J., Suresh, S. & Ravichandran, G. Dynamic indentation for determining the strain rate sensitivity of metals. *J. Mech. Phys. Solids* **51**, 1923-1938 (1998).

Sharpe, W. N. Interferometric surface strain measurement. *International Journal of Nondestructive Testing* **3**, 59-76 (1971).

Sharpe, W. N., Payne T. S. & Smith, M. K. Biaxial laser-based displacement transducer. *Review of Scientific Instruments* **49**, 741-745 (1978).

List of Figures

Figure 1 Geometry and loading configuration for a bimaterial specimen consisting of a Homalite and a steel plate.

Figure 2 Dynamic photoelasticity setup. A circular polarized laser beam passes through the specimen that is subjected to uniform confining stress and to impact shear loading via a projectile fired by a gas gun. The resulting isochromatic fringe patterns are recorded by a high-speed digital camera.

Figure 3 (a) Schematic illustration of the experimental configuration for the sliding velocity measurement. The area inside the dotted line is shown magnified. Points M_1 and M_2 were at the same distance d from the impact side of the Homalite plate; (b) Photograph of the actual setup.

Figure 4 Schematic illustration of the experimental configuration for the simultaneous measurement of the horizontal and vertical components of the particle velocity. The area inside the dotted line is shown magnified.

Figure 5 Photograph of the velocimeter. It is composed of an interferometer (Polytec, OFV-511), a velocity decoder (Polytec, OFV-5000) and a velocimeter head (Polytec, OFV-C-102).

Figure 6 Schematic illustration for the measurement of the in-plane and out-of-plane components of the particle velocity. The area inside the dotted line is shown magnified.

Figure 7 Schematic illustration of the experimental setup for the simultaneous measurement of the horizontal velocity at essentially the same point on the lateral surface S_1 of the upper Homalite plate by two independent velocimeters. The area inside the dotted line is shown magnified, $d = 10\,mm$.

Figure 8 (a) The horizontal velocity history recorded by two independent velocimeters at a point that was situated on the lateral surface S_1 of the upper Homalite plate at a distance of $10\,mm$ from the interface. The confining stress was $10\,MPa$ and the impact speed was $13\,m/s$. (b) The curves inside the dotted square of figure (a) are shown in higher resolution.

Figure 9 (a) Schematic illustration of the experimental setup for the out-of-plane (A) and in-plane (B) horizontal particle velocity measurement. (b) Histories of the out-of-plane and in-plane horizontal particle velocities. The confining stress was $10\,MPa$, the impact speed was $11\,m/s$ and the distance of points A and B from the interface was $d = 5\,mm$.

Figure 10 (a) Schematic illustration of the experimental setup for the horizontal particle velocity measurement for angles of 1^o and 5^o between the laser beam and the vertical Homalite plane. (b) Histories of the horizontal particle velocity for angles of 1^o and 5^o between the laser beam and the vertical Homalite plane. The confining stress was $10\,MPa$ and the impact speed was $9.5\,m/s$. The point A was at a distance $d = 70\,mm$ from the impact side of the Homalite plate.

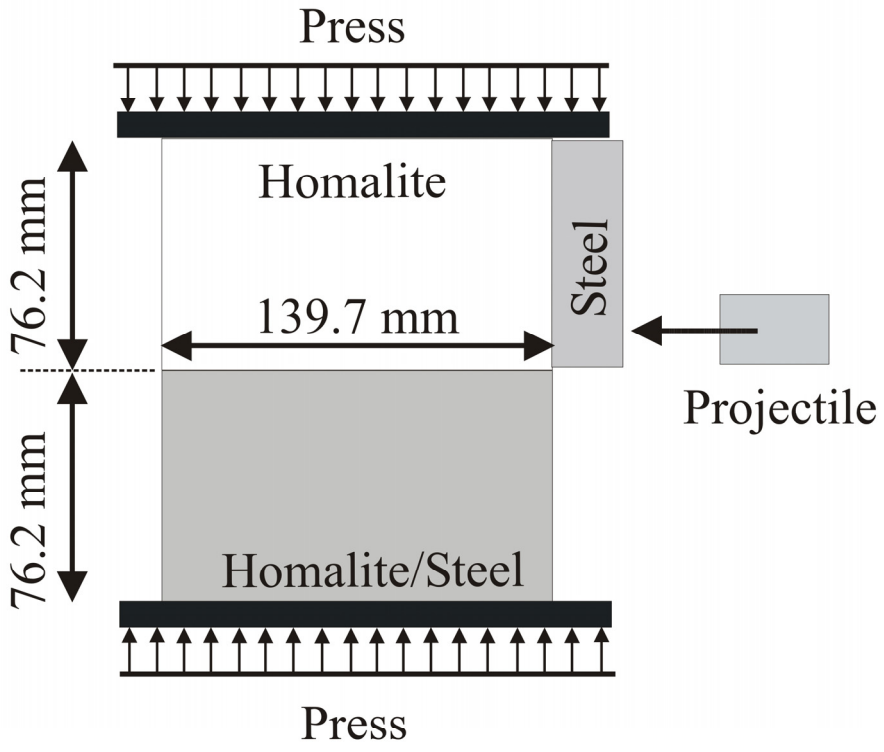

Figure 1 Geometry and loading configuration for a bimaterial specimen consisting of a Homalite and a steel plate.

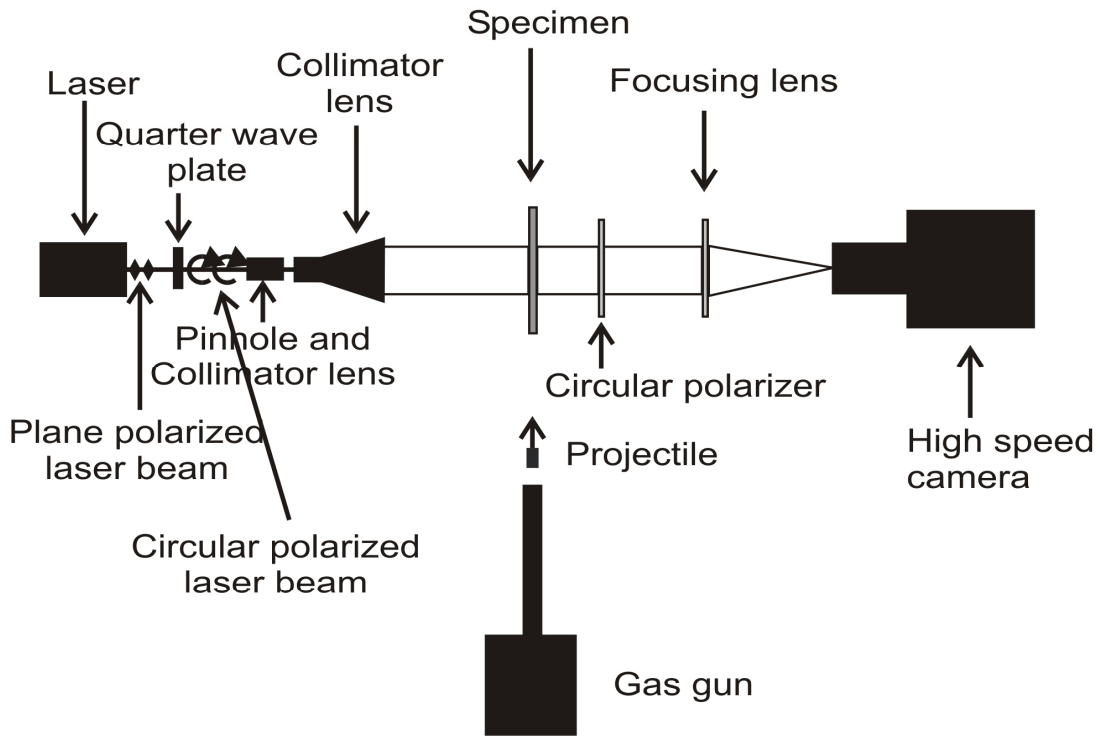

Figure 2 Dynamic photoelasticity setup. A circular polarized laser beam passes through the specimen that is subjected to uniform confining stress and to impact shear loading via a projectile fired by a gas gun. The resulting isochromatic fringe patterns are recorded by a high-speed digital camera.

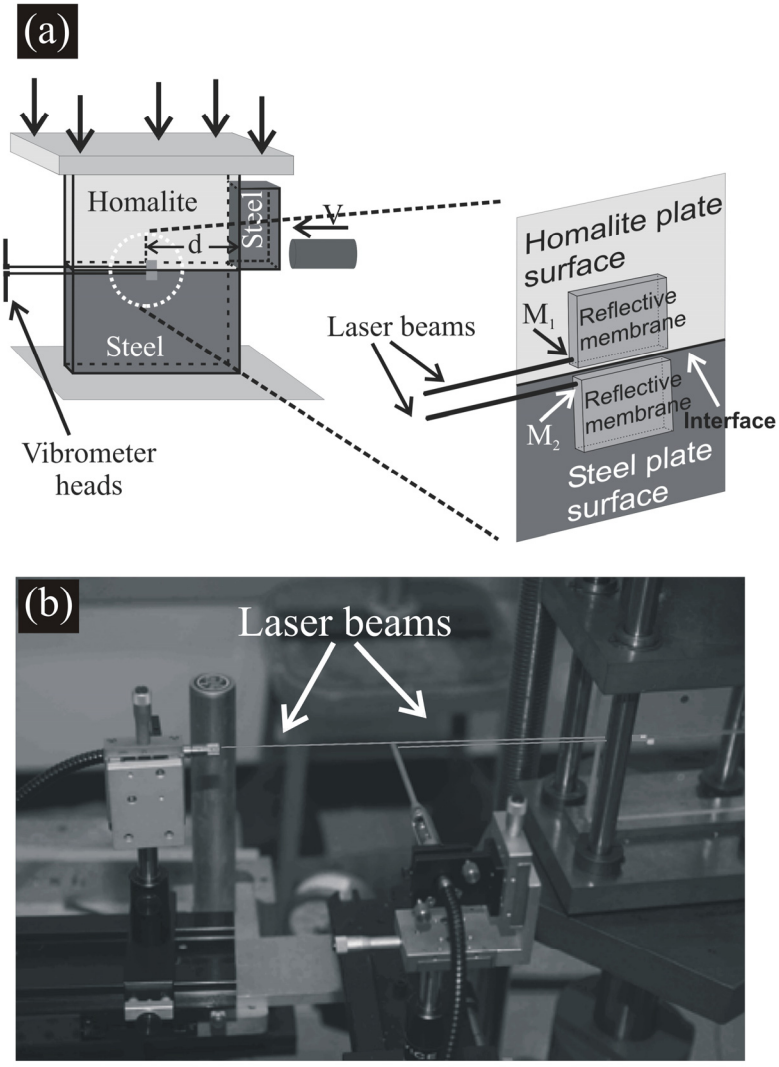

Figure 3 (a) Schematic illustration of the experimental configuration for the sliding velocity measurement. The area inside the dotted line is shown magnified. Points M_1 and M_2 were at the same distance d from the impact side of the Homalite plate (b) Photograph of the actual setup.

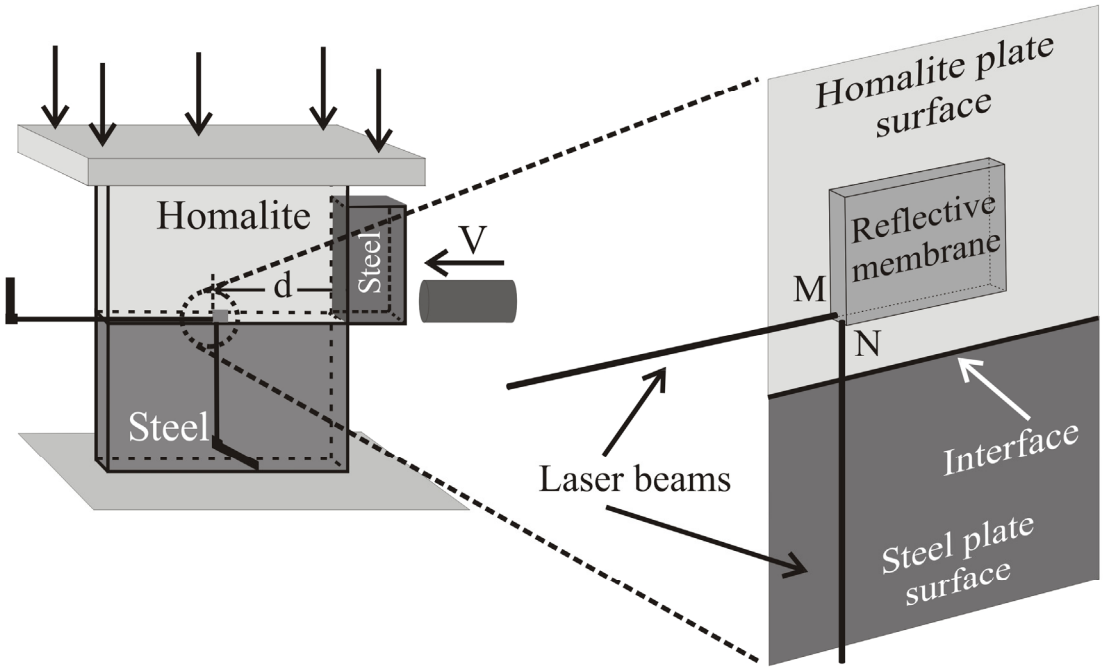

Figure 4 Schematic illustration of the experimental configuration for the simultaneous measurement of the horizontal and vertical components of the particle velocity. The area inside the dotted line is shown magnified.

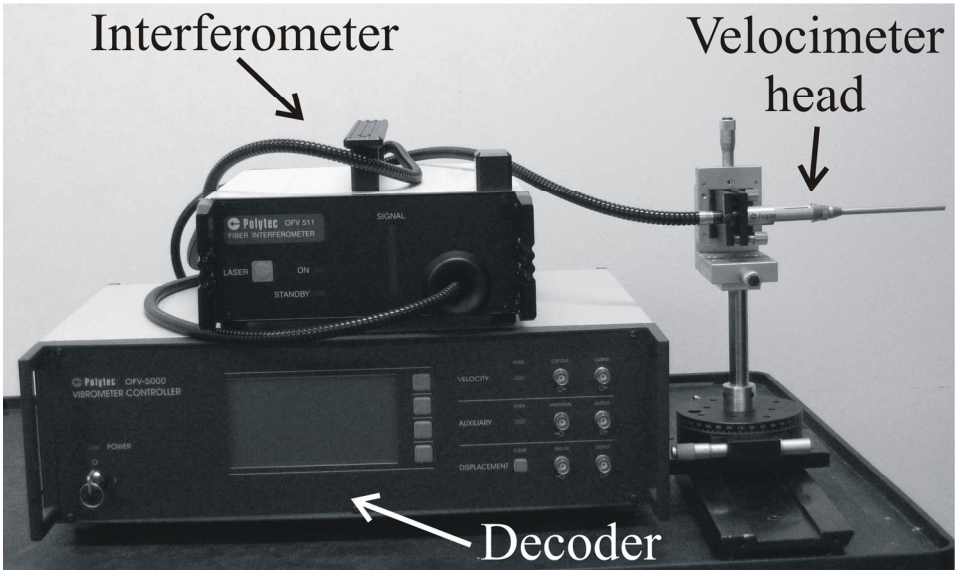

Figure 5 Photograph of the velocimeter. It is composed of an interferometer (Polytec, OFV-511), a velocity decoder (Polytec, OFV-5000) and a velocimeter head (Polytec, OFV-C-102).

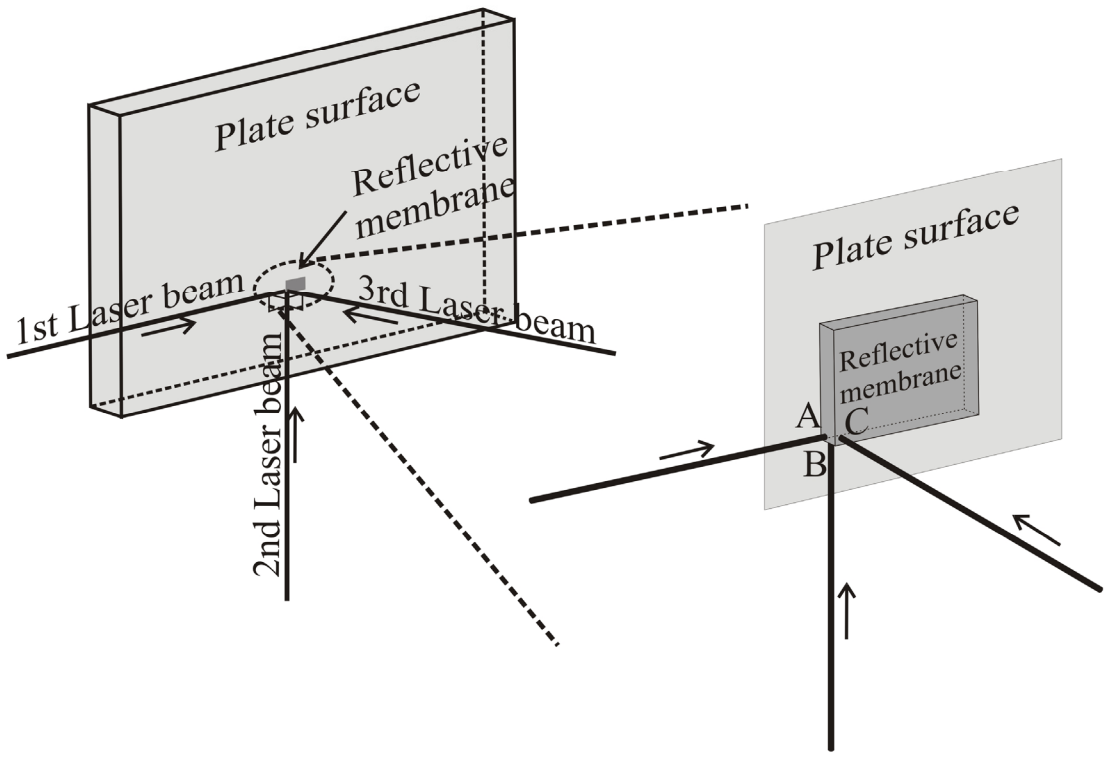

Figure 6 Schematic illustration for the measurement of the in-plane and out-of-plane components of the particle velocity. The area inside the dotted line is shown magnified.

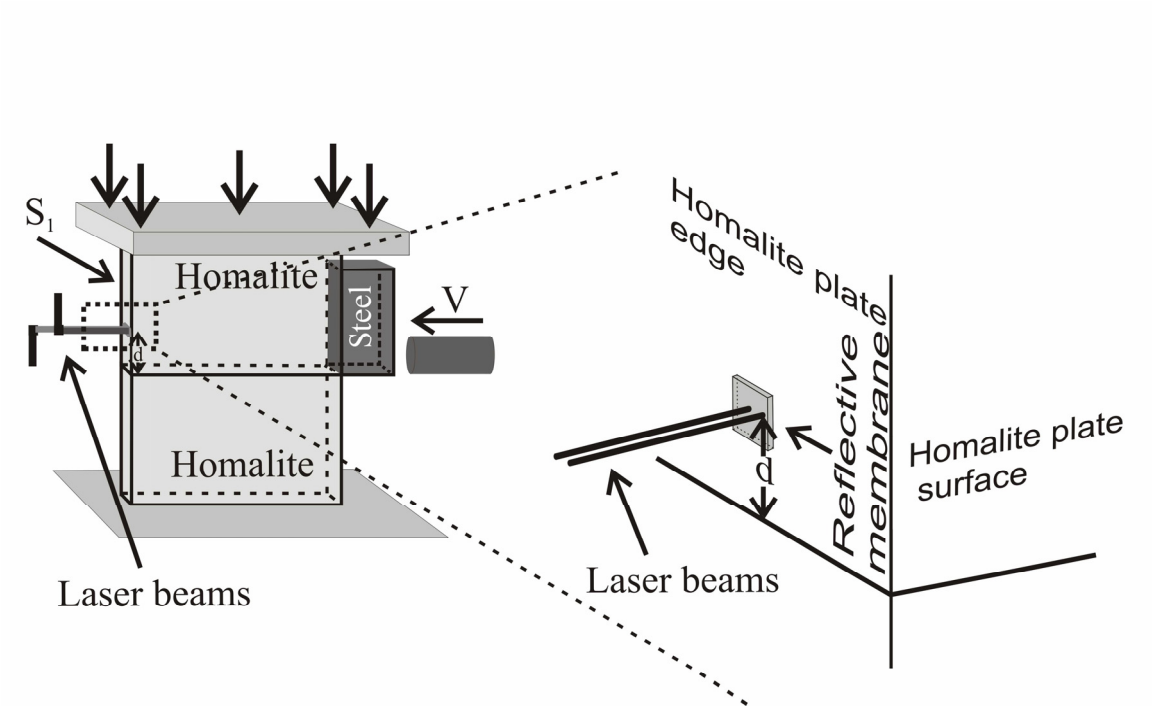

Figure 7 Schematic illustration of the experimental setup for the simultaneous measurement of the horizontal velocity at essentially the same point on the lateral surface S_1 of the upper Homalite plate by two independent velocimeters. The area inside the dotted line is shown magnified, $d = 10\,mm$.

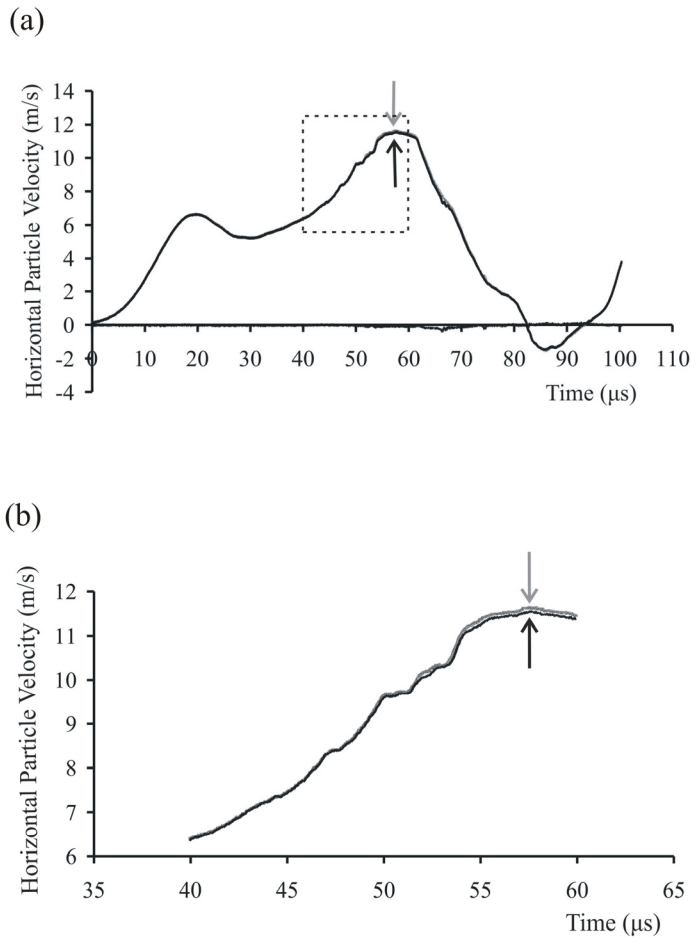

Figure 8 (a) The horizontal velocity history recorded by two independent velocimeters at a point that was situated on the lateral surface S_1 of the upper Homalite plate at a distance of $10\,mm$ from the interface. The confining stress was $10\,MPa$ and the impact speed was $13\,m/s$. (b) The curves inside the dotted square of figure (a) are shown in higher resolution.

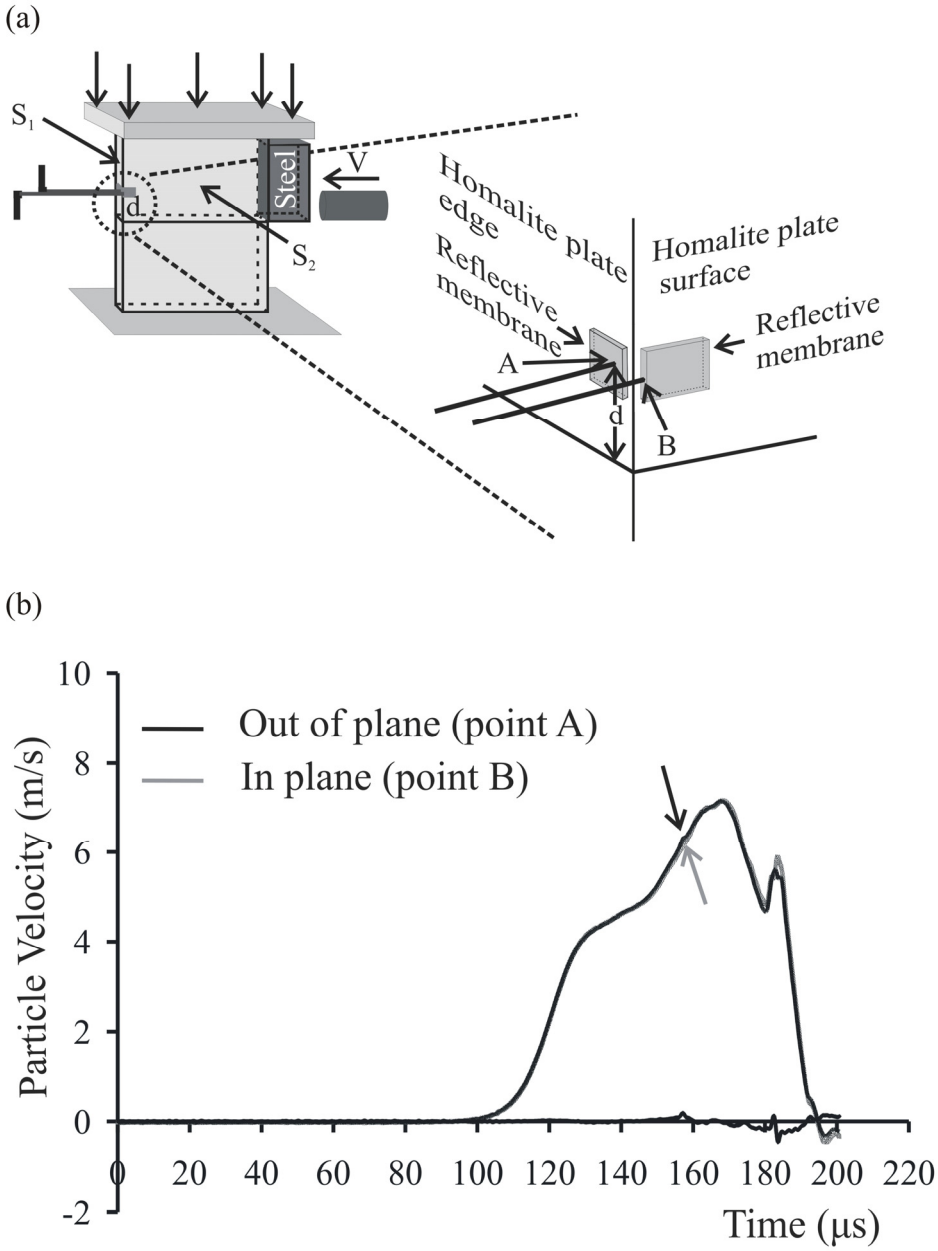

Figure 9 (a) Schematic illustration of the experimental setup for the out-of-plane (A) and in-plane (B) horizontal particle velocity measurement. (b) Histories of the out-of-plane and in-plane horizontal particle velocities. The confining stress was $10\,MPa$, the impact speed was $11\,m/s$ and the distance of points A and B from the interface was $d = 5\,mm$.

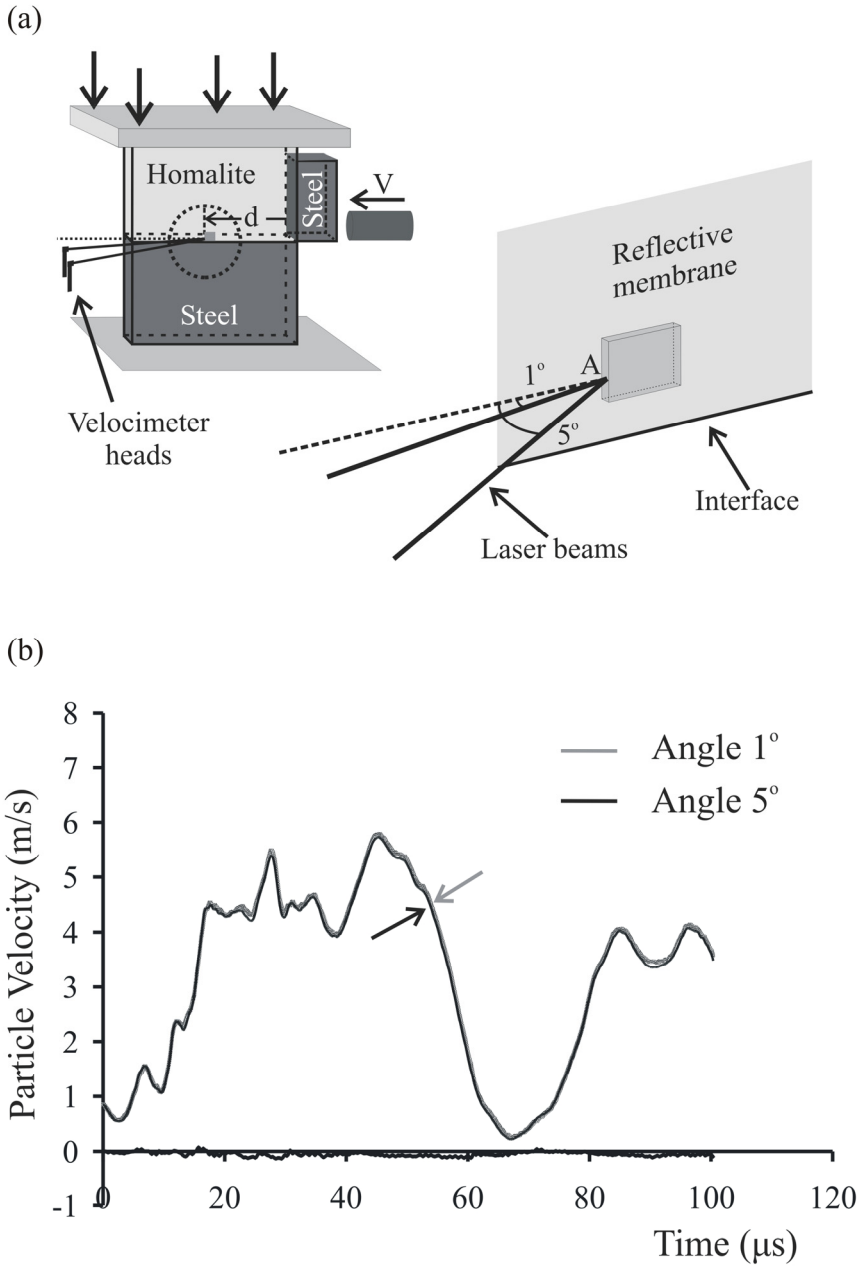

Figure 10 (a) Schematic illustration of the experimental setup for the horizontal particle velocity measurement for angles of 1^o and 5^o between the laser beam and the vertical Homalite plane. (b) Histories of the horizontal particle velocity for angles of 1^o and 5^o between the laser beam and the vertical Homalite plane. The confining stress was $10\,MPa$ and the impact speed was $9.5\,m/s$. The point A was at a distance $d = 70\,mm$ from the impact side of the Homalite plate.

C h a p t e r 3

FRICTIONAL SLIDING OF INCOHERENT BIMATERIAL INTERFACES SUBJECTED TO IMPACT SHEAR LOADING

3.1 Introduction

Earlier interest in dynamic failure processes along bimaterial interfaces has been focused on the case of coherent interfaces (bonded interfaces of finite strength and toughness). However, many composite structures in various engineering applications (e.g., bolted joints and sandwich structures) consist of layers of different materials held together by applied pressure without any bond between the contact faces. In order to utilize these layered structures effectively, the failure procedure along the incoherent (frictional) interfaces is the key problem to be investigated. Here, we confine our attention to the failure process generated by impact shear loading. Unlike the case of coherent interfaces, where the resistance to failure through sliding comes from the bond between the plates, in the case of incoherent interfaces the resistance to sliding comes from the frictional forces between the surfaces in contact.

Classic dynamic fracture theories (Freund 1990; Broberg 1999) of growing shear cracks have many similarities to the frictional sliding process. These theories treat the rupture front as a distinct point (sharp-tip crack). The crack-like rupture of coherent interfaces, separating similar and dissimilar solids subjected to dynamic shear loading, has been the subject of extensive experimental, numerical and analytical investigations in the past years

and was summarized by Rosakis in a recent review article (Rosakis 2002). Of relevance to the present study is the persistent occurrence of intersonic shear rupture along coherent bimaterial interfaces (Tippur and Rosakis 1991; Liu, Lambros and Rosakis 1993; Lambros and Rosakis 1995; Singh and Shukla 1996; Rosakis, Samudrala, Singh and Shukla 1998; Kavaturu, Shukla and Rosakis 1998).

Theoretical and numerical investigations (Comninou and Dundurs 1977; Weertman 1980; Andrews and Ben-Zion 1997) have shown that incoherent interfaces of compressed bimaterial structures can sustain wrinkle-like pulses involving separation. Particle displacement in a direction perpendicular to the interface is greater in the slower material than in the faster material; that may result in a local separation of the interface during sliding. Wrinkle-like pulses have also been observed experimentally in rubber sliding experiments (Anooshehpoor and Brune 1999). We note that the wrinkle-like pulses (separation or detachment waves) propagate at a speed close to the shear wave speed of the slower material and are different from the Schallamach waves, which are very slow compared to the wave speeds of the involved materials (Schallamach 1971).

In this chapter, frictional sliding along incoherent interfaces in bimaterial systems is studied experimentally. Pairs of rectangular Homalite and steel plates are used. A uniform external compressive stress is applied to the bimaterial specimen via a hydraulic press. Asymmetric impact loading is imposed using a gas gun and a steel projectile. Dynamic photoelasticity is combined with laser interferometry-based velocimetry to record frictional sliding events in a microsecond time scale. The fringe pattern evolution in conjunction with the sliding

velocity history gives direct evidence of the sliding mode, the existence of a supersonic disturbance with respect to Homalite, the exact point of sliding initiation and the sliding propagation speed. Strong evidence of a wrinkle-like pulse traveling along the interface is also recorded. The results presented here show that under some loading conditions the failure of bimaterial structures subjected to impact shear loading can take the form of a supershear crack-like sliding, followed by a local opening displacement in the form of a wrinkle-like pulse.

The following sections 3.2 and 3.3 are identical with sections 2.2 and 2.3 in chapter 2. The reason for this repetition is to ensure that chapter 3 can be self-contained. Some limited repetition regarding the materials used, the specimen configuration and the experimental techniques is also encountered in chapters 4 and 5 for the same reason as above.

3.2 Materials and Specimen Configuration

Experiments were performed to investigate the nature of dynamic frictional sliding along the incoherent interface of a high-contrast bimaterial system. The bimaterial specimen consisted of a Homalite-100 plate and a steel plate held together by a uniform compressive stress (see Figure 1). Homalite-100 is a mildly rate-sensitive brittle polyester resin that exhibits stress-induced birefringence with an optical coefficient of $F_\sigma = 22.6\,KN/m$. At the strain rate developed during the experiments (on the order of $10^3\,s^{-1}$) and at room temperature, Homalite exhibits a purely linear elastic behavior. The longitudinal, shear and Rayleigh wave speeds in Homalite are $C_1^H = 2583\,m/s$, $C_2^H = 1249\,m/s$ and

$C_R^H = 1155\,m/s$ respectively. Steel was chosen as the other half of the bimaterial system because it provides a strong material property mismatch across the interface, similar to mismatches encountered in composites. The dilatational, shear and Rayleigh wave speeds in steel are $C_1^S = 5838\,m/s$, $C_2^S = 3227\,m/s$ and $C_R^S = 2983\,m/s$ respectively. The wave speeds for Homalite and steel were obtained by ultrasonic measurements using shear and pressure transducers operating at $5\,MHz$.

In the experiments, the configuration was approximated by plane stress conditions, since plate specimens $76.2\,mm$ high, $139.7\,mm$ long and $9.525\,mm$ thick were employed. The shear wave speeds are identical in 3-D and for the plane stress approximation. The same is true for the Rayleigh wave speed, since the contribution in the Rayleigh wave formation comes primarily from the shear wave. However, the plane stress longitudinal wave speeds of Homalite-100 and steel are $C_{1\sigma}^H = 2187\,m/s$, $C_{1\sigma}^S = 5378\,m/s$ respectively.

3.3 Experimental Setup and Procedure

A combination of two experimental techniques was used in this investigation. Dynamic photoelasticity, which gives the full field maximum shear stress distribution, was used in conjunction with a new technique based on laser interferometry. This technique provides a continuous local measurement of the in-plane horizontal and vertical components of the relative velocity of two adjacent points across the bimaterial interface. The initiation and evolution of sliding was explored through photoelasticity and velocimetry at a micro-second time scale.

The compressive stress was applied with a hydraulic press calibrated using a load cell. The asymmetric impact loading was imposed via a cylindrical steel projectile with a diameter of $25\,mm$ and a length of $51\,mm$, fired by a gas gun. A steel buffer $73\,mm$ high, $25.4\,mm$ long and $9.525\,mm$ thick was attached to the impact side of the Homalite plate to prevent shattering and to induce a more or less planar loading wave.

3.3.1 Dynamic Photoelasticity Setup

A typical experimental setup for dynamic photoelasticity experiments is shown in Figure 2. The optical setup was arranged for a light field. Isochromatic fringes are contours of maximum in-plane shear stress τ_{max} governed by the stress optical law

$$2\tau_{max} = \sigma_1 - \sigma_2 = N\ F_\sigma / h$$

where F_σ is the material's stress optical coefficient, h is the specimen thickness, σ_1, σ_2 are the principal stresses and $N = n + 1/2$ (with $n = 0,1,2,...$) is the isochromatic fringe order. A continuous laser was used as the light source in our experiments. The vertically polarized laser beam first passed through a quarter wave plate, which transformed it into a circular polarized beam. Then it expanded in a uniform laser beam of $130\,mm$ diameter. The laser beam was transmitted through the specimen and an analyzer. The resulting photoelastic fringe pattern was recorded with a high-speed digital camera (Cordin model 220), which is able to record 16 distinct frames at framing rates up to 100 million frames

per second. In this experimental work, most of the high-speed photography was performed at 250,000 to 1,000,000 frames per second. It is noted that the field of view was wide enough to cover most of the specimen.

3.3.2 Sliding Velocity Measurement Setup

The local sliding velocity was obtained as follows. A pair of fiber-optic velocimeters measured the horizontal particle velocities at two adjacent points across the interface. The horizontal relative velocity history was obtained by subtracting the velocity of a point on the lower plate from the velocity of a point across the interface on the upper plate. A schematic representation of the setup is shown in Figure 3(a). The laser beams emitted from the velocimeters were focused on points M_1 and M_2 on the thin vertical surfaces of the reflective membranes, which were attached to the surfaces of the Homalite (top) and steel (bottom) plates respectively. The distance of each point from the interface was less than $250\mu m$ before compression, and both points had the same horizontal distance from the impact side of the Homalite plates. A picture of the actual setup is presented in Figure 3(b). The technique is presented in detail in Lykotrafitis, Rosakis and Ravichandran 2005.

3.3.3 Simultaneous Measurement of the Horizontal and Vertical Components of the Velocity

The two velocimeters can be used to measure not only the horizontal component of the in-plane velocity, but also the vertical component. For this, the laser beam is aimed perpendicular to the narrow horizontal surface of the reflective membrane. Preliminary

experimental results showed that the velocities in steel plate are one order of magnitude slower than the velocities in Homalite plate. Taking advantage of this fact, we assumed that particle velocities in the steel were negligible and we carried out several tests using the two velocimeters we had at our disposal to record both the horizontal and vertical in-plane particle velocities. These were subsequently interpreted as sliding and opening speeds respectively. A schematic of the setup employed for the measurement is shown in Figure 9.

3.4 Sliding Induced by an Impact Shear Loading Applied on the Homalite Plate of a Bimaterial Specimen

3.4.1 Initiation and Evolution of Dynamic Frictional Sliding

In the present experiments, dynamic photoelasticity (in conjunction with high-speed photography) was combined with velocimetry to investigate the initiation and evolution of frictional sliding along the incoherent interface of a bimaterial specimen consisting of Homalite and steel. The specimen was subjected to a uniform compressive load of $10\,MPa$ and impacted on the Homalite side at a speed of $16.5\,m/s$ .The sequence of photoelastic images in Figure 4 is studied in combination with the horizontal velocities measurements presented in Figure 5. The images in Figure 4 show the isochromatic fringe pattern in the Homalite plate at selected times. A pair of fiber-optic velocimeters recorded the history of the horizontal in-plane velocities of two adjacent points, M_1 and M_2 in the Homalite (top) and steel (bottom) plate respectively (see Figure 3). Both points were at the same horizontal distance of $110\,mm$ from the impact side of the Homalite plate and at less than $250\,\mu m$

from the interface. Figure 5 shows the histories of the horizontal in-plane velocities of both points, as well as the history of the relative horizontal velocity. The insert in Figure 5(a) displays the history of the relative displacement, which was obtained from the velocity history by numerical integration.

The images in Figures 4(a)-(e) have similar structure, and this signifies that sliding had reached a more or less steady state. At $110\,\mu s$ (see Figure 4(f)), reflected waves from the free left side of the plate had entered the picture and the sliding process became transient, resulting in a distorted photoelastic fringe pattern. As can be seen in Figure 4(a), the compressive stress wave (P-wave) in the Homalite plate arrives from the right, in front of a relatively broad fringe structure (shown just behind point F), which has a rib-eye structure and emanates from the interface. Since this structure was missing in similar experiments, without external pressure, we can safely conjecture that it was caused by the interference of the impact wave with the preexisting static pressure.

A head wave emanates from point A on the interface and crosses the eye-like fringe structure. Point A is ahead of the P-wave front in the Homalite plate. This shows that a disturbance was traveling along the interface at a speed higher than the P-wave in Homalite. The propagation speed V of the disturbance was determined in each frame by measuring the Mach angle θ and using the relation $V = C_2^H / \sin\theta$, where C_2^H is the shear wave speed of Homalite. The average value was $2830\,m/s = 0.88\,C_2^S = 0.95\,C_R^S = 1.3\,C_{1\sigma}^H = 1.1\,C_1^H$, where C_2^S is the shear wave speed of steel, C_R^S is the Raleigh

wave speed of steel, $C_{1\sigma}^{H}$ is the plane stress P-wave speed of Homalite and C_{1}^{H} is the plane strain P-wave speed of Homalite. The disturbance traveled at a speed 5% lower than the Rayleigh wave speed of steel and 12% lower than the shear wave speed of steel. This result was consistently repeatable. We note that this disturbance is not a generalized Rayleigh wave, since such waves do not exist for bimaterial systems with large contrast in material properties, such as we have in this case (Achenbach and Epstein 1967; Ranjith and Rice 2001; Rice, Lapusta and Ranjith 2001). The photoelastic images do not provide conclusive evidence regarding the exact nature of the disturbance at point A.

The effect of the above disturbance on the process of sliding was deciphered by using the recorded velocity data presented in Figure 5(b), which shows an expanded view of the history of the velocity of points M_1 and M_2 at the initiation of sliding. Point M_2, which was on the surface of the steel plate, started moving first at approximately $57.5\,\mu s$, under the influence of the compressive stress wave propagating in the steel plate. Point M_1 on the Homalite plate started moving at $59\,\mu s$. During the following $14\,\mu s$, M_1 and M_2 were moving at the same speed until approximately $72\,\mu s$. At that time, the point in the steel plate (M_2) decelerated and its velocity became negative. The velocity of the point on the Homalite plate (M_1) followed the same trend after approximately $1.5\,\mu s$. Up to that time, there was no sliding, since both points traveled together under the influence of the P-wave in the steel plate, and the relative velocity oscillated around zero. Then, at about $74\,\mu s$ and $76\,\mu s$ respectively, the velocities of M_1 and M_2 started increasing again. However, in this case, the velocity of the point on the Homalite surface increased faster than the velocity of

the point on the steel plate. The corresponding photoelastic frame taken at $75\,\mu s$ (Figure 4(b)) shows that a Mach line emanated from the interface, at a short distance in front of the reflective point, and ahead of the P-wave front in the Homalite plate. A very simple calculation shows that a disturbance traveling at a speed of $0.95C_R^S = 1.3C_{1\sigma}^H = 1.1C_1^H$ is expected to be at the reflective point at about $74\,\mu s$. This confirms that the disturbance caused the increase of the particle velocities. The disturbance was supersonic with respect to Homalite, and therefore, it was ahead of the P-wave front traveling in the Homalite plate. In addition, a Mach cone was formed with a tip at the disturbance. The initial impact of the projectile on the steel buffer created a compression P-wave, transmitted into the Homalite plate. Because of friction, some of the energy also transmitted into the steel plate. The P-wave traveled faster in the steel plate than in the Homalite plate, and thus, a precursor effect emerged. Nevertheless, photoelasticity is not very sensitive to compression, and because of this we could not see a possible Mach cone associated with the interface disturbance traveling at the P-wave speed of steel. The disturbance, however, caused the photoelastic fringe pattern to warp enough for it to be captured by the high-speed camera. The insert in Figure 4(a) schematically illustrates the loading configuration, the resulting wave fronts, the shear head wave and the supershear sliding tip with the resulting Mach cone. Curves 1, 2 and 3 correspond to the P-wave front in the steel plate, the shear wave front in the steel plate and the P-wave front in the Homalite plate. Point A represents the disturbance, just behind the shear wave front in the steel plate, and point B_1 represents the sliding tip.

In Figure 4(c), the tip of the first Mach line has passed the position of velocity measurement, whereas the eye-like structure has just arrived there. The velocimeter recording shows that at approximately $76\,\mu s$ the relative horizontal velocity between M_1 and M_2 has increased, but yet not very sharply. We also note that the numerically calculated relative horizontal displacement between the points M_1 and M_2 was less than $1\,\mu m$ until $84\,\mu s$. This indicates that until $84\,\mu s$ there was no sliding, but only shear elastic deformation of the material close to the interface (material between M_1 and M_2). Thus, the disturbance and the eye-like fringe structure did not create slip.

However, at approximately $84\,\mu s$, a drastic change occurred in the relative velocity and in the relative displacement (see Figure 5(a)). The velocity of the measurement point in the Homalite plate increased rapidly, whereas the velocity of the point in the steel plate remained almost constant. This resulted in a very steep rise in the relative velocity and in a very abrupt change in the slope of the relative displacement vs. time diagram. We conclude that the sliding, at the position of measurement, started at around $84\,\mu s$. The corresponding photoelastic frame (see Figure 4(d)) captured at $85\,\mu s$ is extremely revealing, in which a fringe concentration point (point B_1 of Figure 4(a) and (b)) coincides with the measurement position. It is the sliding tip, and because it propagated with a supershear speed, a Mach line emanated from this position. Indeed, following the positions of the tip in different frames and using a linear interpolation, we obtained the tip propagation velocity which was $1970\,m/s = 1.58\,C_2^H$, higher than the shear wave speed of Homalite.

The velocimeter measurement (Figure 5(a)) shows that the speed increased sharply from $84\,\mu s$ to approximately $98\,\mu s$, and then it remained almost constant until $110\,\mu s$, where a second acceleration event occurred. The time instance of $98\,\mu s$ (when the acceleration ceased) corresponded to a fringe concentration point B_2 (see Figure 4(d)). After point B_2, the fringes were parallel to the interface, which means that a constant maximum shear stress field was formed. In Figure 4(f), captured at $110\,\mu s$, the area of the photoelastic pattern with inclined fringes arrived at the measurement position, and this coincided with the initiation of the secondary acceleration caused by the arrival of the reflected waves from the free side of the Homalite plate. From the relative velocity history diagram, we conclude that sliding was continuous during the recording time. This means that sliding occurred in a crack-like mode.

The above exhaustive study of the experimental results clearly shows the power of the proposed point velocity measurement in combination with the full field technique of photoelasticity. We were able to completely identify the different fringe formations in the photoelastic images and explicitly connect them to the changes in sliding velocity. We finally note that, after the initiation of sliding, the in-plane horizontal particle velocity in the steel plate was one order of magnitude lower than the velocity in the Homalite plate. This is true not only for the experiment analyzed above, but for all of the performed experiments using Homalite - steel bimaterial specimens, impacted on the Homalite plate.

The findings of this experiment are similar to results obtained by experiments on crack growth in bimaterials (Samudrala, Huang and Rosakis 2002; Samudrala and Rosakis 2003; Coker, Rosakis and Needleman 2003). The first observations of intersonically traveling cracks were made in connection with crack propagation along the interface of bimaterial systems (Tippur and Rosakis 1991; Liu, Lambros and Rosakis 1993; Lambros and Rosakis 1995; Singh and Shukla 1996; Rosakis, Samudrala, Singh and Shukla 1998; Kavaturu, Shukla and Rosakis 1998). In the shear crack propagation experiments, the Homalite and steel plates were bonded together and a notch was machined along the bond line at one edge. Thus, the resistance to rupture was generated mainly from the bond. In the present study, the resistance to sliding was due to the frictional stress between the surfaces of the two plates in contact. It is noted that the frictional resistance was not uniform along the interface and not constant with time, since the dynamic compression and the sliding velocity were changing with position and time.

3.4.2 Influence of Impact Speed and Confining Stress on Sliding

Figure 6(a) displays an instantaneous isochromatic fringe pattern developed in an experiment where the impact speed decreased to $12\,m/s$ while the confining pressure was kept constant at $10\,MPa$. The fringe configuration has basically the same structure with that in the experiment presented in the previous section. A head wave which crosses the eye-like fringe structure appears as, does the fringe formation B_1B_2. The recorded velocity history of points M_1 and M_2 is illustrated in Figure 6(b). In this case, however, the velocities were measured $70\,mm$ from the impact side of the Homalite plate and the

maximum speed was less than $10\,m/s$, which is the velocimeter limit. We thus captured the evolution of the velocities over a longer period of time than before. By synchronizing the showed in Figure 6(a) velocity history recordings with the captured high-speed images, the different features appearing in the photoelastic image can be identified. The initial disturbance (at point A), which traveled at approximately $2955\,m/s = 1.14\,C_1^H = 2.37\,C_2^H = 0.92\,C_2^S$ and created the head wave which crossed the eye-like fringe structure, arrived at the measurement position at $96\,\mu s$. The sliding started at point B_1 at approximately $103\,\mu s$ and was propagating at a supershear speed of $2097\,m/s = 1.68\,C_2^H$. At approximately $110\,\mu s$ the velocity started increasing faster; this is shown in the photoelastic picture as a disturbance in the fringe structure (second dotted line). At approximately $112\,\mu s$, when point B_2 arrived at the measurement position, the velocity slowed down, and was oscillating until $120\,\mu s$, when another acceleration occurred. Then, the velocity remained high at approximately $6\,m/s$ for $30\,\mu s$. The velocity then decreased until approximately $180\,\mu s$, when another acceleration started, caused by the arrival of the reflected waves from the free left side of the Homalite plate. The last acceleration in Figure 5(a) happened sooner because the measurement point was closer to the free side of the Homalite plate, and the reflected waves arrived earlier in that case than here. The velocity of point M_2 on the steel plate was one order of magnitude lower than the velocity of point M_1, and thus, the relative velocity was almost identical with the velocity of point M_1.

Figure 7(a) shows the in-plane relative horizontal velocity history measured at the same distance of $70\,mm$ from the impact side of the Homalite plate in two different experiments. The external compression was $10\,MPa$ and the impact speeds were $13\,m/s$ and $12\,m/s$. The two measurements were consistent. They include an initial acceleration period and a period where the variation in speed is small. The relative velocity generated by the impact at $13\,m/s$ was slightly higher than the sliding velocity generated from the impact at $12\,m/s$ during the whole recording period. The duration of the first period of sliding was approximately $70\,\mu s$, the same for both experiments, and then a second period of sliding started because of the reflected waves from the free left side of the Homalite plate. The in-plane relative horizontal velocities measured $30\,mm$ from the impact side of the Homalite plate are displayed in Figure 7(b), for three different experiments performed at $10\,MPa$ external confining pressure and at impact speeds of $9\,m/s$, $11\,m/s$ and $13\,m/s$. The duration of the first period of sliding was approximately $60\,\mu s$, the same for all three cases. The relative velocities increased with the impact speed. We mention that the velocity corresponding to an impact speed of $13\,m/s$ saturated the velocimeter at around $20\,\mu s$ and $50\,\mu s$, but each time it recovered its measurement ability. It is also noted that the speeds after $70\,\mu s$ increased slowly, because the reflected waves had not arrived at the measurement position before the end of the recording. In Figure 7(c), the horizontal velocity histories recorded $30\,mm$ and $70\,mm$ from the impact side of the Homalite plate are compared. In both cases the impact speed was $13\,m/s$. The results show that the maximum velocity decreases because of attenuation. They also show that the duration of

the initial period of sliding increases as the distance between the measurement position and the impact side of the Homalite plate increases.

In this paragraph, results are presented for confining stresses less than $10\,MPa$. In Figure 8(a), the confining stress was $5\,MPa$ and the impact speed was $13\,m/s$. As the confining stress decreases, the eye-like fringe structure becomes less pronounced. By synchronizing the photoelastic images with the recorded relative velocity history (Figure 8(b)), we can conclude that the sliding at the velocity measurement point M started at approximately $50\,\mu s$, when point B crossed the measurement position. The sliding speed was supershear ($1932\,m/s = 1.55\,C_2^H = 0.75\,C_1^H$) and because of this a Mach line, highlighted by a dotted line, emanates from point B. A fringe structure can be seen at point C. It is noted that this structure crossed the measurement position at approximately $70\,\mu s$ and it did not generate any visible effect on the velocity history diagram. It traveled at a speed of $1261\,m/s = 1.0\,C_2^H$, close the shear wave speed of Homalite, and its character will be revealed in the next section. Decreasing the compression further at $1.5\,MPa$ and keeping the impact speed at $13.5\,m/s$, the eye-like fringe structure has almost completely disappeared (see Figure 8(c)). The fringe density is low and there is no visible discontinuity that would signify the initiation of sliding. However, by matching the velocity history diagram (Figure 8(d)) with the sequence of the recorded photoelastic images, the sliding tip can be located at point B (Figure 8(c)). The sliding at point M started at approximately $82\,\mu s$. At point C, a fringe structure appears traveling along the interface. Figures 8(b) and

8(d) show that the velocity of sliding increased more abruptly at lower compression than in the case of a confining stress of $10\,MPa$. This fact indicates that minor elastic effects took place before the initiation of sliding.

3.4.3 Observation of Wrinkle-like Pulses

The particle velocities in the steel plate were one order of magnitude less than the velocities in Homalite plate. Taking advantage of this fact, we used two velocimeters to record both the horizontal and vertical in-plane components of the velocity at a point on the Homalite plate, very close to the interface (see Figure 9). We then interpreted our measurements as "sliding" and "opening" speeds by assuming that the steel plate is effectively rigid compared to the Homalite.

Figure 10 shows a sequence of six isochromatic patterns displaying the evolution of maximum shear stress contours in the Homalite plate. The confining external stress applied to the bimaterial specimen was $5\,MPa$ and the speed of the projectile at impact was $22\,m/s$. Figure 11(a) shows the histories of the horizontal and vertical in-plane components of the velocity at points M and N respectively on the Homalite plate. These points were at a distance of $70\,mm$ from the impact side of the Homalite plate and at a distance of less than $250\,\mu m$ from the interface (see Figure 9). At $40\,\mu s$, the arrival of the P-wave front and the eye-like fringe structure at point M was captured by the high-speed camera (see Figure 10(a)). This was fortuitous, because we could now combine visual evidence from the photoelastic picture with the recording of the velocimeters. Figure 11(a)

shows that at $40\mu s$ the horizontal velocity increased, whereas the vertical velocity became negative, showing that point N moved downward, toward the velocimeter head. The interpretation is clear. Point M moved to the left under the influence of the horizontal compressive stress generated by the impact. Because of the Poisson effect, the horizontal compressive stress induced a dynamic (inertial) vertical compressive stress that forced point N to move downward. Using the experience accumulated from the previous experiments, we estimated that sliding started at approximately $46\mu s$, when the relative velocity increased rapidly. From $40\mu s$ to $46\mu s$, elastic shearing occurred, whereas sliding initiated when the tip of the Mach line (point B in Figure 10(a)) crossed the velocity measurement position M. At $50\mu s$, the sliding tip B was to the left of the measurement position (Figure 10(b)), signifying that the sliding had already started. Point B was traveling at a supershear speed of $1932 m/s = 1.55 C_2^H$. Figure 11(a) shows that at around $60\mu s$ the horizontal velocity reached its maximum value and the sliding continued for the rest of the recording time with no large variations in the sliding tip speed.

It is interesting to follow the evolution of the vertical velocity in Figure 11(a), and especially the evolution of the vertical displacement depicted in Figure 11(b). It is noted that the vertical displacement was obtained from the vertical velocity history by numerical integration. At the start, the specimen was subjected to a uniform external compression of $5 MPa$. A very simple 1D calculation showed that the vertical displacement of point N from the initial uncompressed position was less than $1\mu m$. The impact wave created a dynamic (inertial) compression which added to the static compression and the displacement

became more negative. However, after $55\mu s$, the vertical velocity became positive, which means that point N was moving upward, approaching the initial uncompressed position. At approximately $65\mu s$, the displacement became positive, signifying the initiation of the detachment of the Homalite plate from the steel plate. At approximately $95\mu s$, the opening closed and sliding continued again under compression. Looking at the photoelastic images in Figure 10, we see that at $65\mu s$ a fringe structure (shown by arrow C) approached the measurement position. At $70\mu s$ this structure arrived at N, when an interface opening started. At $100\mu s$ (see Figure 10(f)), when the opening had closed, the fringe structure had departed from N. The propagation speed of this fringe pattern was $1260 m/s = 1.0 C_2^H$, the shear wave speed of Homalite. The data show that the above fringe structure represents a wrinkle-like pulse traveling along the interface. The obtained speed is also consistent with theoretical predictions. The wrinkle-like pulse (detachment wave) had been predicted theoretically by Comninou and Dundurs 1977 and Weertman 1980 and numerically by Andrews and Ben-Zion 1997. However, this is the first observation of a wrinkle-like pulse at high strain rate experiments on elastic bimaterials. Optical evidence of wrinkle-like pulses traveling along interfaces of similar-material plates have also been recorded (see Lykotrafitis and Rosakis 2005). Anooshehpoor and Brune 1999 have found similar wrinkle-like pulses in sliding experiments involving very slow wave speed materials such as foam rubber. The above-mentioned fringe structure was very robust. It appeared in all of our experiments conducted at high impact speeds and low compressive loads, and was always connected to a local opening. We mention that the wrinkle-like pulse was not present in the first experiment, because the impact speed was not high enough to

trigger detachment. Finally, we note that the whole area from point B to point C in Figure 10(a) was sliding under compression.

As the impact speed decreased, we expect that the wrinkle-like pulse will create smaller vertical separation. In Figure 12(a) a photoelastic image shows the fringe pattern at a specific time in the case of a projectile speed of $13\,m/s$ and a confining pressure of $5\,MPa$. Although, the fringe density is lower than that in Figure 9, the eye-like structure and the following Mach-line are clearly visible. The supershear speed of the sliding tip was approximately $1833\,m/s = 1.47\,C_2^H$. A broad fringe structure located just behind the measurement point M signifies the wrinkle-like pulse. It is less visible than that in Figure 10, where the impact speed was higher. Its propagation speed was $1261\,m/s = 1.0\,C_2^H$. The time evolution of the vertical displacement at the measurement position is displayed in Figure 12(b). As in the case of the lower impact speed, the loading wave generates compression and a decompression period follows later. The maximum opening was approximately $12\,\mu m$, almost half of the opening produced in the case of $22\,m/s$. Experiments at lower impact speeds than $13\,m/s$ and at the same external pressure show reduced decompression produced by the wrinkle-like pulse. By increasing the confining stress the same effect was observed: the decompression decreased. Figure 12(c) shows a snapshot of the isochromatic fringes generated by an impact speed of $11\,m/s$ while the external applied stress was $10\,MPa$. It is noted that no visual sign of a wrinkle-like pulse appears in the full field photoelastic images. The history of vertical displacement (Figures 12(d)) shows that after the initial dynamic compression caused by the impact loading the

decompression was not enough to produce a significant positive displacement. Thus, in this case there was not any wrinkle-like pulse propagated along the interface, consistent with the fact that no fringe structure characteristic of the wrinkle-like pulse appears in the corresponding photoelastic image. We finally note that the wrinkle-like pulse did not appear in some of the experiments presented in the previous section as well (see Figures 4 and 6(a)), because the impact speed was again not high enough to produce detachment.

3.4.4 Frictional Sliding Induced by High Impact Speeds

In the experimental results we have presented up to this point, the impact speeds were low, less than $22\,m/s$. In this section, dynamic sliding initiated by impact speeds on the order of $50\,m/s$ will be investigated. Only photoelasticity will be employed here, since the resulting maximum particle velocities from the impact loading were well beyond $10\,m/s$ which is the limit of the velocimeter.

Figure 13(b) displays an instantaneous isochromatic fringe pattern generated by an impact speed of $52\,m/s$, at a uniform confining stress of $10\,MPa$. It is observed that while the basic characteristic features which appeared in cases at lower impact speeds and at the same confining stress (see e.g., Figure 4(a)) are also present here, new features emerge in the picture. An eye-like fringe pattern traveling behind the P-wave front (F) emanated from the interface. A head-wave originating from point A ahead of the P-wave front crossed the eye-like fringe formation. The inclination of the Mach line shows that the head wave was created by a disturbance moving along the interface at a supersonic speed (with respect to

Homalite) of $2813\,m/s = 2.25\,C_2^H = 1.1\,C_1^H = 1.3\,C_{1\sigma}^H$. We note at this point that because of the high impact speed, the head wave was intensified and thus became clearly visible. Figure 13(b) answers positively to any skepticism regarding the existence of such a wave based on the poor definition of the Mach line in previous cases at lower impact speeds. Figure 14(a) depicts the computed speeds of the head wave at various frames, using the relation $V = C_2^H / \sin\theta$, and the obtained average value. A second Mach line, behind the eye-like fringe structure, emanates from the supershear sliding tip B. The sliding propagation speed of $2563\,m/s = 2.0\,C_2^H = 1.0\,C_1^H = 0.79\,C_2^S$ was obtained from the inclination angle of the well-defined Mach line (Figure 14(a)). Both Mach lines are highlighted in the insert of Figure 13(b). Comparable experimental and numerical results, regarding the speed of the sliding tip, have been obtained by Coker, Rosakis and Needleman 2003 in the case of a dynamic crack growth along a composite-Homalite cohesive interface induced by an impact loading similar to that used in the present experiment. Two robust fringe structures appear behind the rupture tip (points C and D in Figure 13(b)). Following their position at different recorded photoelastic frames, their speeds were obtained through a linear interpolation. Figure 14(b) shows the positions of points C and D in various frames and the computed corresponding propagation speeds. The speed of point D was $2294\,m/s = 1.84\,C_2^H = 0.71\,C_2^S$. The fringe structure at point D could perhaps be linked to a theoretically predicted disturbance by Ranjith and Rice 2001, who studied the slip dynamics at an interface between dissimilar materials. In the case of a large contrast bimaterial system (steel-PMMA), they traced a disturbance traveling along the interface at a speed of $1.84\,C_2^{PMMA}$, similar to the speed of the disturbance that appeared in

our experiments. We also note that the disturbance at point D was robust and appeared in a persistent manner at high impact speed experiments. Its appearance becomes more pronounced as the confining stress decreases (see Figure 13 (c) - (d)). Point C was traveling at a speed of $1199\,m/s = 0.96\,C_2^H$ and we conclude that the corresponding fringe structure reflected the propagation of a wrinkle-like pulse along the interface, consistent to the results obtained at lower impact speeds.

At a compression of $20\,MPa$ and at an impact speed of $44\,m/s$ the same basic features as above arose with the eye-like fringe structure widened (Figure 13(a)). A remarkable difference is that in this case two sliding tips (B_1 and B_2) appeared. They traveled at different speeds and they formed an unstable supershear sliding zone which shrunk with time, as the speed of point B_2 was $2357 = 1.89\,C_2^H$, higher than the speed of B_1 which was $1854 = 1.48\,C_2^H$. Because both speeds were supershear, a transient double shock was formed. The disturbance at A, ahead of the P-wave front, was traveling at $2851 = 2.28\,C_2^H$ again creating a head wave which crossed the eye-like fringe formation. Behind the unstable segment B_1B_2, both the fast disturbance at D and the wrinkle-like pulse were present. The wrinkle-like pulse (point C) was traveling at $1237 = 0.99\,C_2^H$. The fast disturbance D was transient and we were not able to obtain its propagation speed. The insert in Figure 13(a) highlights the head wave and the double Mach lines.

As the confining stress was decreased to $5\,MPa$, the eye-like fringe structure shrank (Figure 13(c)) and it almost completely disappeared at $2\,MPa$ (Figure 13(d)). In Figure 13(c), the Mach line corresponds to a rupture tip velocity of $2545 = 2.0\,C_2^H$. The fast disturbance at D was traveling at $2178 = 1.74\,C_2^H$ while the speed of the wrinkle-like pulse at C was $1234 = 0.99\,C_2^H$. In the case displayed in Figure 13 (d), the confining stress was very low at $2\,MPa$ and the impact speed was $44\,m/s$. An unstable double shock wave was emanating from points B_1 and B_2, which were traveling at speeds of $2039\,m/s = 1.63\,C_2^H$ and $2039\,m/s = 1.63\,C_2^H$ respectively. The fast and slow (wrinkle-like) disturbances also appeared, propagating at speeds of $2039\,m/s = 1.63\,C_2^H$ and $1151\,m/s = 0.92\,C_2^H$ respectively. In addition, another slow interface disturbance appeared at point E. Its speed was $1125\,m/s = 0.9\,C_2^H$ and it seems that it is of the wrinkle-like type since the fringe structure and the propagation speed are similar to the corresponding features of the wrinkle-like pulses. This result, along with results obtained from experiments performed at similar conditions, shows that as the confining pressure decreased, two or more wrinkle-like pulses propagated along the interface, since a local opening occurred more easily.

3.4.5 Study of the Speeds of the Various Features Propagating Along the Bimaterial Interface

The propagation speeds for the head wave, the sliding tip, the fast interface disturbance and for the wrinkle-like pulse for various impact speeds and for different confining stresses are

displayed in Figure 15. As the impact speed increased, the propagation speed of the sliding tip also increased, approaching the P-wave speed of Homalite (Figure 15(b)).The rupture tip speeds were supershear with respect to Homalite for all the performed experiments. Figure 15(a) shows that the head wave speed, which was consistently lower than the shear wave of steel but higher than the P-wave speed of Homalite, did not depend on the impact speed. The same is true for the wrinkle-like pulse. Its speed was, within an experimental error, between the Rayleigh wave speed and the shear wave speed of Homalite (Figure 15(d)), consistent with the theoretical values obtained by Comninou and Dundurs 1977. The speed of the fast interface disturbance was also not dependent on the impact speed (Figure 15(d)). We note, however, that this disturbance, unlike the previous features, was transient at confining stresses of $10\,MPa$ and $20\,MPa$, and only with lower static pressures did it have a persistent appearance and a robust form.

3.5 Sliding Induced by Impact Shear Loading Applied on the Steel Plate of the Bimaterial Specimen

In this section, dynamic sliding initiated by impact loading applied on the steel plate is investigated. Figure 16(a) shows the isochromatic fringe pattern developed in the Homalite plate at a selected time with an impact speed of $17\,m/s$ and a confining stress of $10MPa$. The formation of a shear Mach line shows that a disturbance was traveling along the bimaterial interface at a speed higher than the shear wave speed of Homalite. The inclination angle of the Mach line was approximately 18^o, which corresponds to a $4042\,m/s = 1.25\,C_2^S = 0.7\,C_1^S$ propagation speed of the disturbance. This result means that

the disturbance follows closely the P-wave front in the steel plate. For more information however, we have to resort to velocimetry since photoelasticity is not very helpful given that the photoelastic images do not have enough structure. This happens because the dynamic vertical compressive stress was very low, since the Young's modulus of steel is large and thus the Poisson effect was very limited during sliding. Figure 16(b) depicts the evolution with time of the in-plane horizontal velocities of two points M_1 and M_2 (across the interface), which belonged to steel and Homalite plates respectively. The distance of M_1 and M_2 from the impact side of the steel plate was $30\,mm$ and their distance from the interface was less than $250\,\mu m$. The velocity of point M_1 on the steel plate was higher that the velocity of point M_2 on the Homalite plate, despite the fact that steel is much a stiffer material than Homalite. This shows that the energy transfer from the steel plate to the Homalite plate was not efficient. The Poisson effect, as we have already mentioned above, was minor and the dynamic (inertial) compression applied to the Homalite plate was low. Consequently, the frictional resistance was also low, and the local sliding initiated almost immediately with the arrival of the P-wave front there, without any significant elastic deformation of the Homalite surface. This is clear from Figure 16(c), where the velocity history of points M_1 and M_2 at the first microseconds of the sliding initiation is depicted. The velocity of point M_1 on the steel plate started increasing at approximately $36\,\mu s$ because of the horizontal compression applied from the longitudinal wave. Almost immediately, point M_2 (on the Homalite plate surface) started moving, dragged by the motion in the steel plate because of friction. At $40\,\mu s$ the relative velocity started increasing rapidly and sliding started (Figure 16(b)). This shows that elastic deformation

happened at the very first $4\,\mu s$ after the longitudinal wave arrival at M_1. The above result obtained through velocimetry agrees with the result obtained via photoelasticity (that a supershear disturbance, with respect to Homalite, was propagating along the interface just behind the P-wave front in steel) and makes clear that the disturbance was the sliding tip. It agrees also with both the experimental and numerical results obtained by Coker, Rosakis and Needleman 2003. We note that the process of sliding initiation was different in the case where the Homalite plate was impacted. For example, Figure 5(b) shows that for approximately $24\,\mu s$ points M_1 and M_2 were traveling together, since merely elastic deformation occurred during this period. Only after $24\,\mu s$ elapsed did the sliding start.

Figure 17 displays the history of the in-plane horizontal velocities of points M_1 and M_2, belonging to steel and Homalite plates respectively. The external confining stress was $10\,MPa$ and the impact speed was $13.5\,m/s$. The horizontal distance of points M_1 and M_2 from the impact side of the Homalite plate was again $30\,mm$. The sliding initiation procedure was very similar to that depicted in Figure 16(b). We also note that the duration of the initial sliding period was approximately $43\,\mu s$ (from $55\,\mu s$ until $98\,\mu s$), the same for both cases. The only difference is that the maximum horizontal velocity of M_1 was lower than in the previous case since the impact speed was lower here. The velocity of point M_2 in Homalite plate was also lower in Figure 17 than in Figure 16.

Figure 18 shows the time evolution of the horizontal in-plane velocities of points M_1 and M_2 located $110\,mm$ from the impact side of the steel plate. The external pressure was

$10\,MPa$ and the impact speed was $17\,m/s$. The same conditions were applied to the experiment shown in Figure 16. The velocities histories, however, depicted in Figure 16 were measured $30\,mm$ form the impact side of the steel plate. The sliding initiation procedure is similar in both cases. The difference between the two measurements is due to the attenuation of the particle velocities in steel, whereas the attenuation of the speed in Homalite was smaller. Moreover, the variation of the particle velocity on steel at $110\,mm$ was not as fast as it was at $30\,mm$.

We finally note that in all the performed experiments the duration of local sliding was long, and we conclude that rupture occurred in a crack-like mode.

3.6 Concluding Remarks

A new technique has been developed to record the evolution of the in-plane components of the particle velocity in real time. The combination of velocimetry with the full-field technique of dynamic photoelasticity was proven to be a very powerful tool in the study of dynamic frictional sliding along incoherent interfaces.

The experiments involved bimaterial specimens consisting of Homalite-100 and steel plates held together by uniform compressive stress and subjected to impact shear loading. When the impact loading was applied to the Homalite plate, the following effects were captured:

- The interaction between the impact wave and the preexisting static stress field caused a relatively broad loading wave that emanated from the interface.

- A disturbance, traveling along the interface at a speed close to the Rayleigh wave speed of steel, generated a Mach line that crossed the P-wave front and the eye-like fringe pattern. Data recorded by the velocimeter showed that this disturbance affected the relative velocity but did not cause sliding.
- The velocimeter revealed that the sliding initiated behind the eye-like fringe structure. A shear Mach line was visible in the photoelastic images, indicating that the sliding was supershear with respect to the shear wave speed of Homalite.
- The sliding occurred in a crack-like mode.
- A fast interface disturbance was captured propagating behind the rupture tip at high impact speeds.
- A self-sustaining wrinkle-like pulse propagating along the bimaterial interface was observed. It caused a local detachment between the two plates that was traveling at a speed close to the Rayleigh wave speed of Homalite. It is expected that the wrinkle-like pulse might play an important role in the failure mechanism of bimaterial structures subjected to impact shear loading.

When the impact loading was applied to the steel plate, then velocimetry was the only source of information. Sliding at a point on the interface started almost immediately with the arrival of the P-wave front there and it occurred in a crack-like mode in all the performed experiments.

REFERENCES

Achenbach, J. D. & Epstein, H. I. Dynamic interaction of a layer and a half-space. *J. Eng. Mech.* **5**, 27-42 (1967).

Andrews, D. J. & Ben-Zion, Y. Wrinkle-like slip pulse on a fault between different materials. *J. Geophys. Res.* **102**, 553-571 (1997).

Anooshehpoor, A. & Brune, J. N. Wrinkle-like Weertman pulse at the interface between two blocks of foam rubber with different velocities. *Geophys. Res. Lett.* **23**, 2025-2028 (1999).

Broberg, K. B. *Cracks and fracture.* (Academic Press, London, 1999).

Coker, D., Rosakis, A. J. & Needleman, A. dynamic crack growth along a polymer composite-homalite interface. *J. Mech. Phys. Solids* **51**, 425-460 (2003).

Comninou, M. & Dundurs, J. Elastic interface waves involving separation. *ASME J. Appl. Mech.* **44**, 222-226 (1977).

Freund, L. B. *Dynamic fracture mechanics* (Cambridge University Press, Cambridge, UK, 1990).

Kavaturu, M., Shukla, A. & Rosakis, A. J. Intersonic crack propagation and interfaces: Experimental observations and analysis. *Experimental Mechanics* **38**, 218-225 (1998).

Lambros, J. & Rosakis, A. J. Shear dominated transonic interfacial crack growth in a bimaterial-I. Experimental observations. *J. Mech. Phys. Solids* **43**, 169-188 (1995).

Liu, C., Lambros, J. & Rosakis, A. J. Highly transient elastodynamic crack growth in a bimaterial interface: Higher order asymptotic analysis and optical experiments. *J. Mech. Phys. Solids* **41**, 1857-1954 (1993).

Lykotrafitis, G. & Rosakis, A.J. Sliding along frictionally held incoherent interfaces in homogeneous systems under dynamic shear loading. *Int. J. Fract.*, Submitted (2005).

Lykotrafitis, G., Rosakis, A. J. & Ravichandran, G. Particle velocimetry and photoelasticity applied to the study of dynamic sliding along frictionally-held bimaterial interfaces: Techniques and feasibility. *Experimental Mechanics*, Accepted (2005).

Ranjith, K. & Rice, J. R. Slip dynamics at an interface between dissimilar materials. *J. Mech. Phys. Solids* **49**, 341-361 (2001).

Rice, J. R., Lapusta, N. & Ranjith, K. Rate and state dependent friction and the stability of sliding between elastically deformable solids. *J. Mech. Phys. Solids* **49**, 1865-1898 (2001).

Rosakis, A. J., Samudrala, O., Singh, R. P. & Shuckla, A. Intersonic crack propagation in bimaterial systems. *J. Mech. Phys. Solids* **46**, 1789-1813 (1998).

Rosakis, A. J. Intersonic shear cracks and fault ruptures. *Advances in Physics* **51**, 1189-1257 (2002).

Samudrala, O., Huang, Y. & Rosakis, A. J. Subsonic and intersonic mode II crack propagation with a rate-dependent cohesive zone. *J. Mech. Phys. Solids* **50**, 1231-1268 (2002).

Samudrala, O. & Rosakis, A. J. Effect of loading and geometry on the subsonic/intersonic transition of bimaterial interface crack. *Eng. Fract. Mech.* **70**, 309-337 (2003).

Schallamach, A. How does rubber slide? *Wear* **17**, 301-312 (1971).

Singh, P. R. & Shukla, A. subsonic and transonic crack growth along a bimaterial interface. *ASME J. Appl. Mech.* **63**, 919-924 (1996).

Tippur, H. V. & Rosakis, A. J. Quasi-static and dynamic crack growth along bimaterial interfaces: A note on crack-tip field measurements using coherent gradient sensing. *Experimental Mechanics* **31**, 243-251 (1991).

Weertman, J. Unstable slippage across a fault that separates elastic media of different elastic constants. *J. Geophys. Res.* **85**, 1455-1461 (1980).

List of Figures

Figure 1 Geometry and loading configuration for a bimaterial specimen consisting of a Homalite and a steel plate.

Figure 2 Dynamic photoelasticity setup. A circular polarized laser beam passes through the specimen that is subjected to uniform confining stress and to impact shear loading via a projectile fired by a gas gun. The resulting isochromatic fringe patterns are recorded by a high-speed digital camera.

Figure 3 (a) Schematic illustration of the experimental configuration for the sliding velocity measurement. The area inside the dotted line is shown magnified. Points M_1 and M_2 were at the same distance d from the impact side of the Homalite plate. (b) Photograph of the actual setup.

Figure 4 A sequence of isochromatic fringe patterns showing an intersonic frictional sliding, the corresponding shear Mach line (B_1) and a shear head wave (A). M_1 and M_2 are the positions of the velocity measurements.

Figure 5 (a) Histories of the horizontal in-plane velocities and of the relative velocity, measured at two adjacent points across the interface, $110\,mm$ from the impact side of the Homalite plate. The sliding initiated at B_1. The insert shows the

history of the relative displacement. (b) Detail of the velocity history diagram, showing the arrival of the P-wave front in the steel plate (P), the arrival of the shear wave front in the steel plate (A) and the sliding initiation (B_1).

Figure 6 Representative isochromatic fringe pattern and corresponding horizontal velocity histories and relative horizontal velocity history of points M_1 and M_2 located $70\,mm$ from the impact side of the Homalite plate. The head wave is highlighted by the white dotted line. The sliding started at B_1. The black dotted line marks the warping of the fringes related to a change in the slope of the horizontal particle velocity in Homalite, which occurred at $110\,\mu s$ after impact.

Figure 7 (a) Comparison of the horizontal in-plane relative velocity histories of points M_1 and M_2, located at distances of $70\,mm$ from the impact side of the Homalite plate, for different impact speeds. (b) Comparison of the horizontal in-plane relative velocity histories of points M_1 and M_2, located at distances of $30\,mm$ from the impact side of the Homalite plate, for different impact speeds. (c) Comparison of the horizontal in-plane relative velocity histories of points M_1 and M_2, located at distances of $70\,mm$ and $30\,mm$ from the impact side of the Homalite plate, for the same impact speed of $13\,m/s$. In all cases, the external compression is $10\,MPa$.

Figure 8 (a) and (c) Isochromatic fringe pattern captured during two different experiments. The supershear sliding initiated at B, whereas the wrinkle-like pulse is located at C. The dotted line highlights the Mach line. (b) and (d) Histories of the horizontal components of the in-plane particle velocity measured on the Homalite plate, $70\,mm$ from its impact side.

Figure 9 Schematic illustration of the experimental configuration for the simultaneous measurement of the horizontal and vertical components of the particle velocity. The area inside the dotted line is shown magnified.

Figure 10 Sequence of isochromatic fringe patterns showing intersonic frictional sliding, the corresponding shear Mach line (B) and the wrinkle-like pulse (C). M and N are at the corner of the reflective membrane, where the horizontal and vertical in-plane components of the velocity were measured.

Figure 11 (a) Histories of the horizontal and the vertical components of the in-plane particle velocity measured on the Homalite plate, $70\,mm$ from its impact side. The sliding initiated at B. The confining stress was $5\,MPa$ and the impact speed was $22\,m/s$. (b) History of the vertical displacement.

Figure 12 Representative isochromatic fringe patterns and corresponding vertical displacement histories measured on the Homalite plate, $70\,mm$ from its impact side.

Figure 13 Representative isochromatic fringe patterns from two different experiments at high impact speeds. The specimens were subjected to different confining stresses. Arrow A indicates the position of the disturbance which created the head wave. The arrows B, C, D and F indicate the positions of the rupture tip, of the wrinkle-like pulse, of the fast interface disturbance and of the P-wave front respectively. The arrow E indicates a second wrinkle-like pulse. The arrow B_1 and B_2 indicate the positions of the sliding tips which are the origin of a transient double shock.

Figure 14 (a) Sliding tip speeds and head wave speeds at different frames measured using the Mach angle. (b) Positions of the wrinkle-like pulse and the fast interface disturbance as a function of time.

Figure 15 (a) Variation of the sliding tip speed with the impact speed for various confining stresses. (b) The head wave speed is independent of the impact speed. (c) The wrinkle-like pulse speed remained between the Rayleigh wave speed and the shear wave speed of Homalite-100, independent of the impact speed and the

confining stress. (d) The speed of the fast interface disturbance did not depend on the impact speed or on the confining stress.

Figure 16 (a) Representative isochromatic fringe pattern from an experiment of sliding propagation initiated by impact on the steel plate. (b) Histories of the horizontal in-plane velocities and of the relative velocity, measured at two adjacent points M_1 and M_2, $30\,mm$ from the impact side of the Homalite plate. (c) Detail of the velocities histories diagram.

Figure 17 Histories of the horizontal in-plane velocities and of the relative velocity, measured at two adjacent points across the interface, $30\,mm$ from the impact side of the Homalite plate.

Figure 18 Histories of the horizontal in-plane velocities and of the relative velocity, measured at two adjacent points across the interface, $110\,mm$ from the impact side of the Homalite plate.

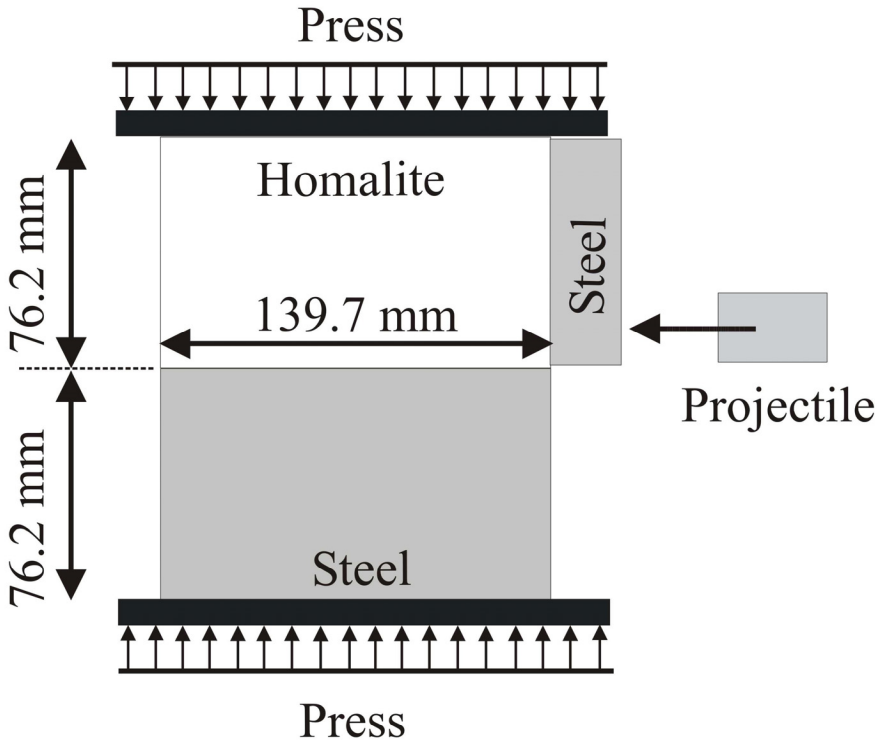

Figure 1 Geometry and loading configuration for a bimaterial specimen consisting of a Homalite and a steel plate.

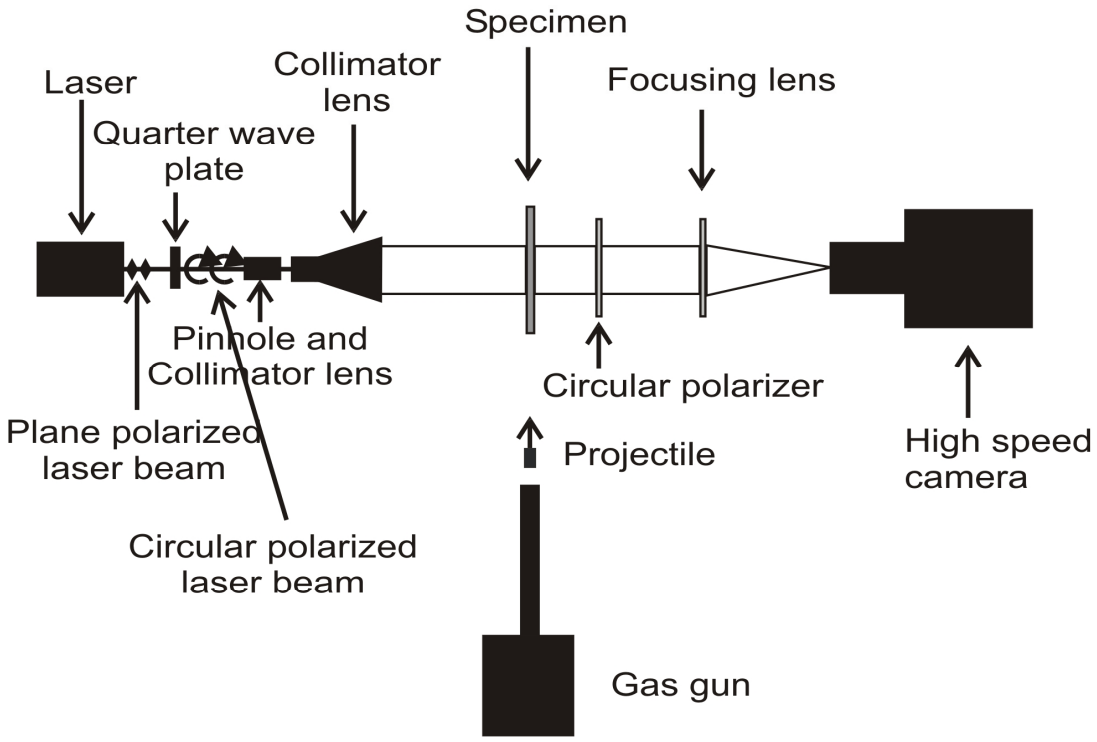

Figure 2 Dynamic photoelasticity setup. A circular polarized laser beam passes through the specimen that is subjected to uniform confining stress and to impact shear loading via a projectile fired by a gas gun. The resulting isochromatic fringe patterns are recorded by a high-speed digital camera.

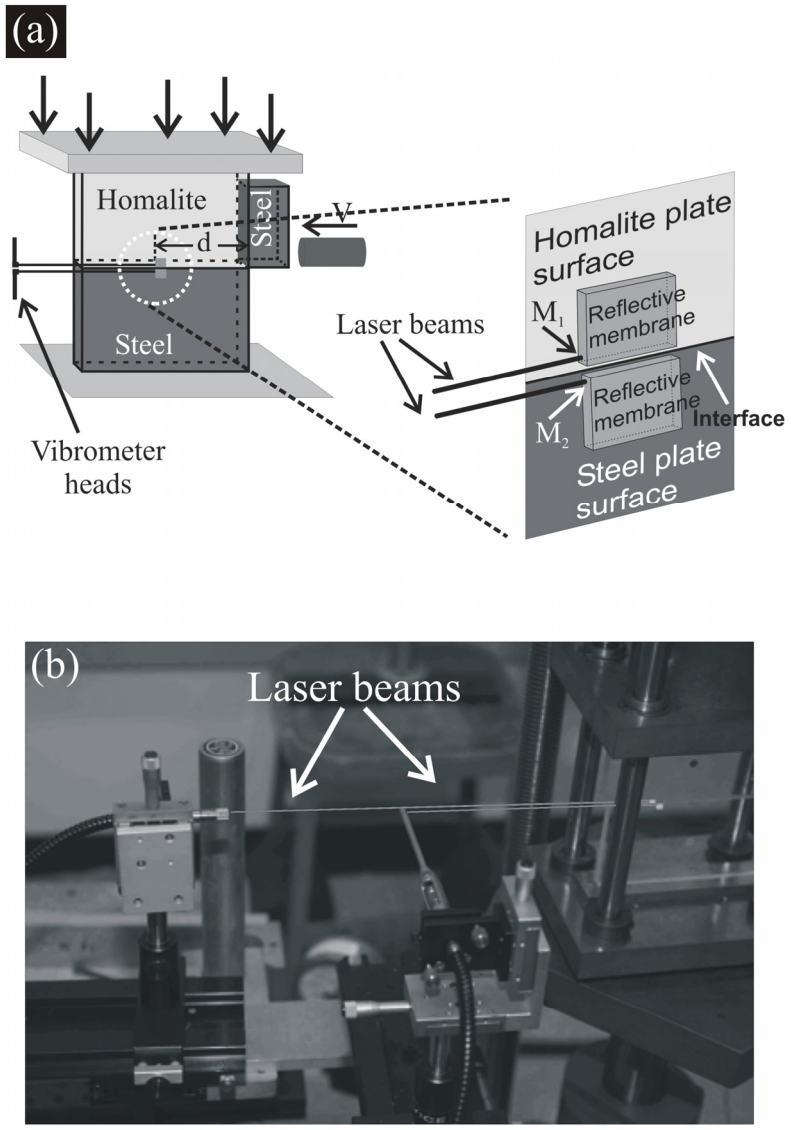

Figure 3 (a) Schematic illustration of the experimental configuration for the sliding velocity measurement. The area inside the dotted line is shown magnified. Points M_1 and M_2 were at the same distance d from the impact side of the Homalite plate. (b) Photograph of the actual setup.

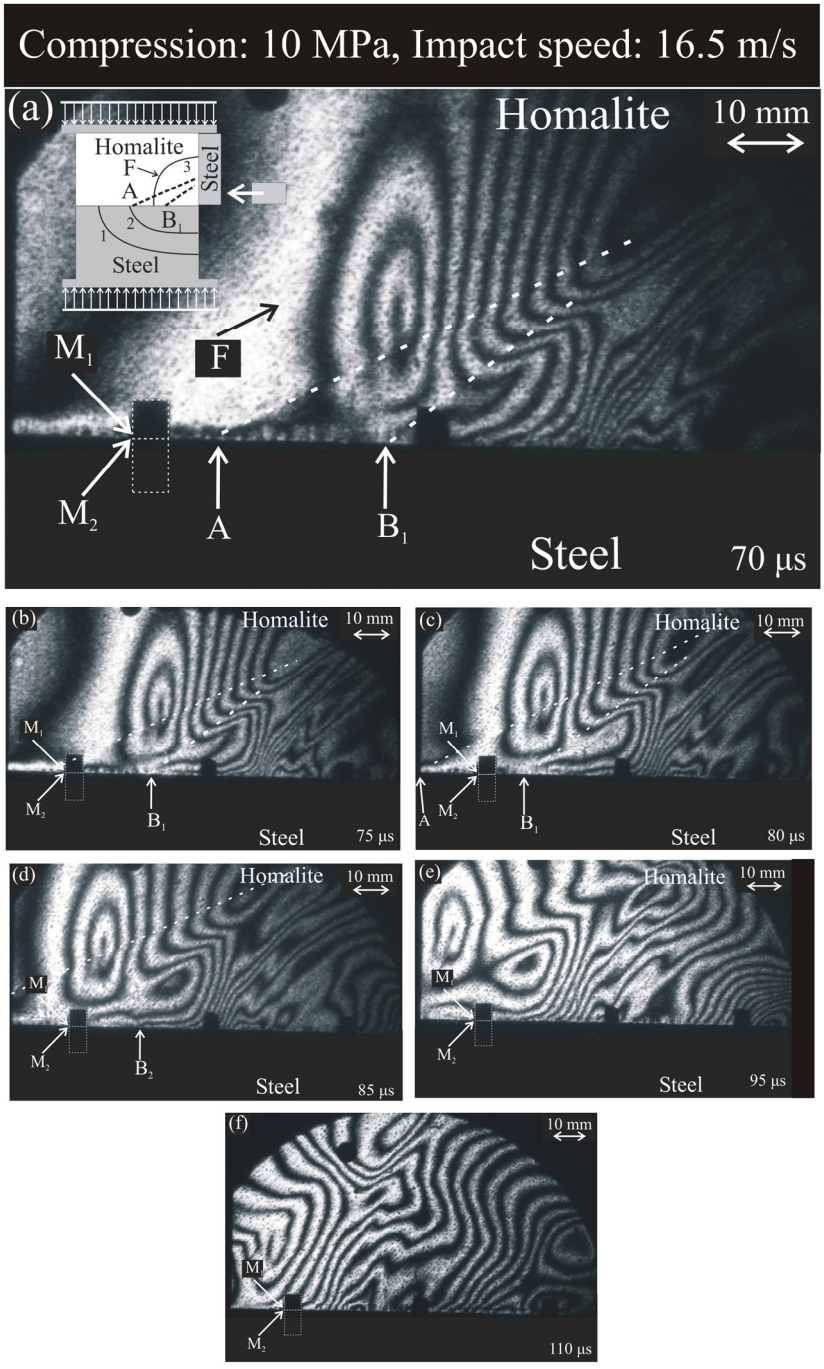

Figure 4 A sequence of isochromatic fringe patterns showing an intersonic frictional sliding, the corresponding shear Mach line (B_1) and a shear head wave (A). M_1 and M_2 are the positions of the velocity measurements.

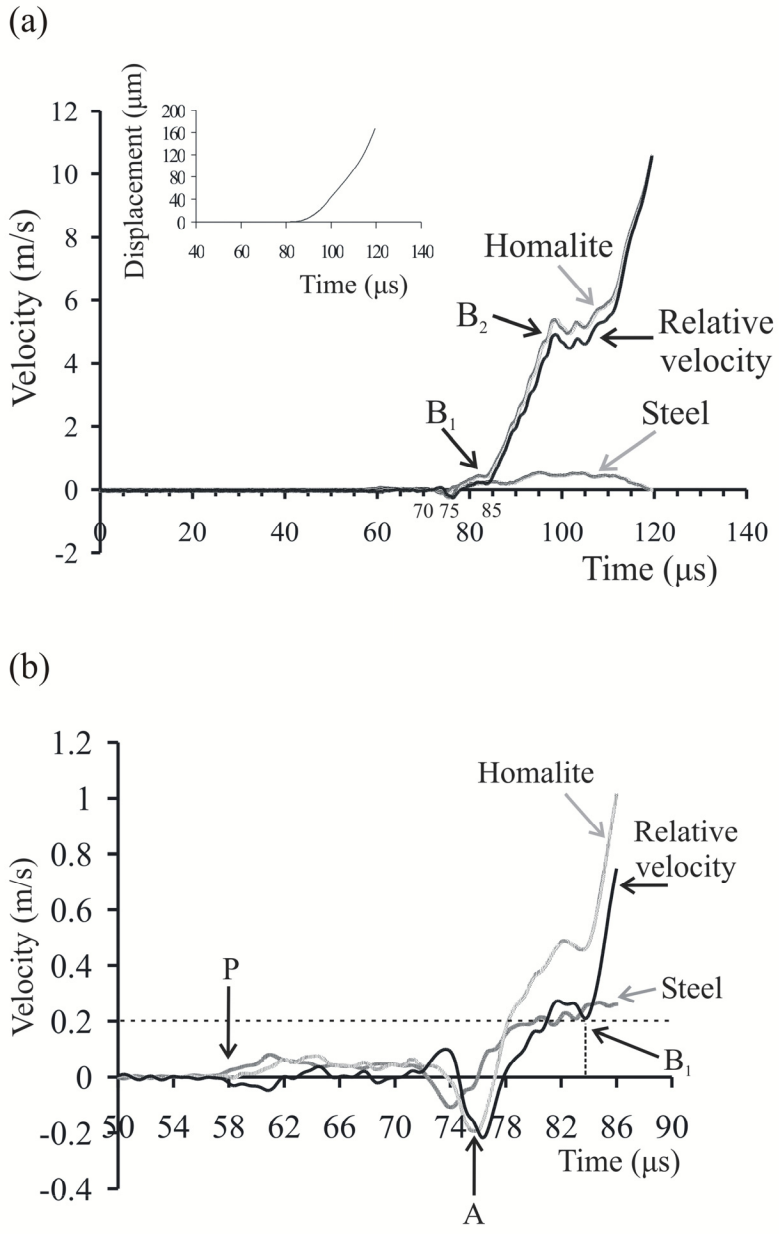

Figure 5 (a) Histories of the horizontal in-plane velocities and of the relative velocity, measured at two adjacent points across the interface, $110\,mm$ from the impact side of the Homalite plate. The sliding initiated at B_1. The insert shows the history of the relative displacement. (b) Detail of the velocity history diagram, showing the arrival of the P-wave front in the steel plate (P), the arrival of the shear wave front in the steel plate (A) and the sliding initiation (B_1).

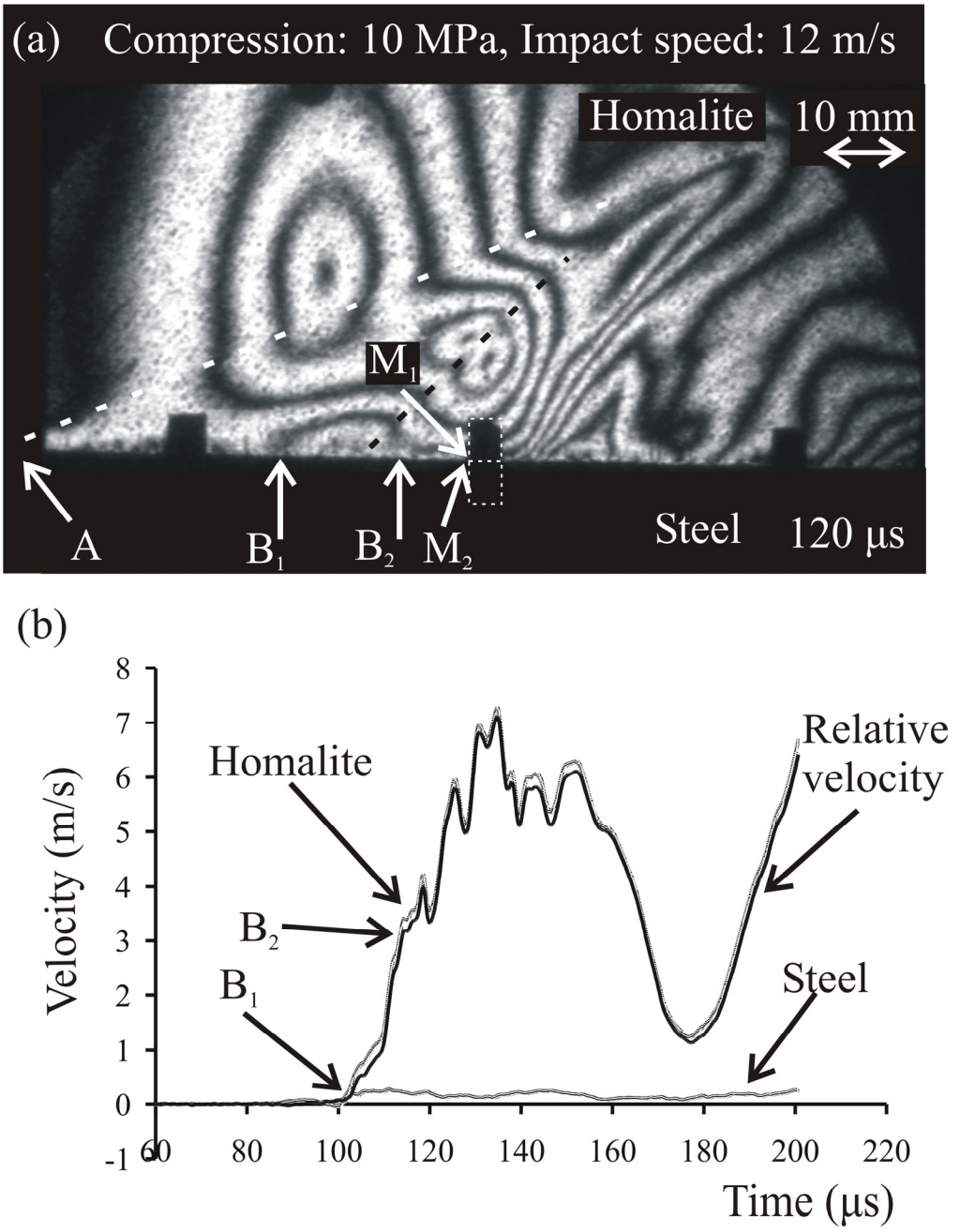

Figure 6 Representative isochromatic fringe pattern and corresponding horizontal velocity histories and relative horizontal velocity history of points M_1 and M_2 located $70\,mm$ from the impact side of the Homalite plate. The head wave is highlighted by the white dotted line. The sliding started at B_1. The black dotted line marks the warping of the fringes related to a change in the slope of the horizontal particle velocity in Homalite, which occurred at $110\,\mu s$ after impact.

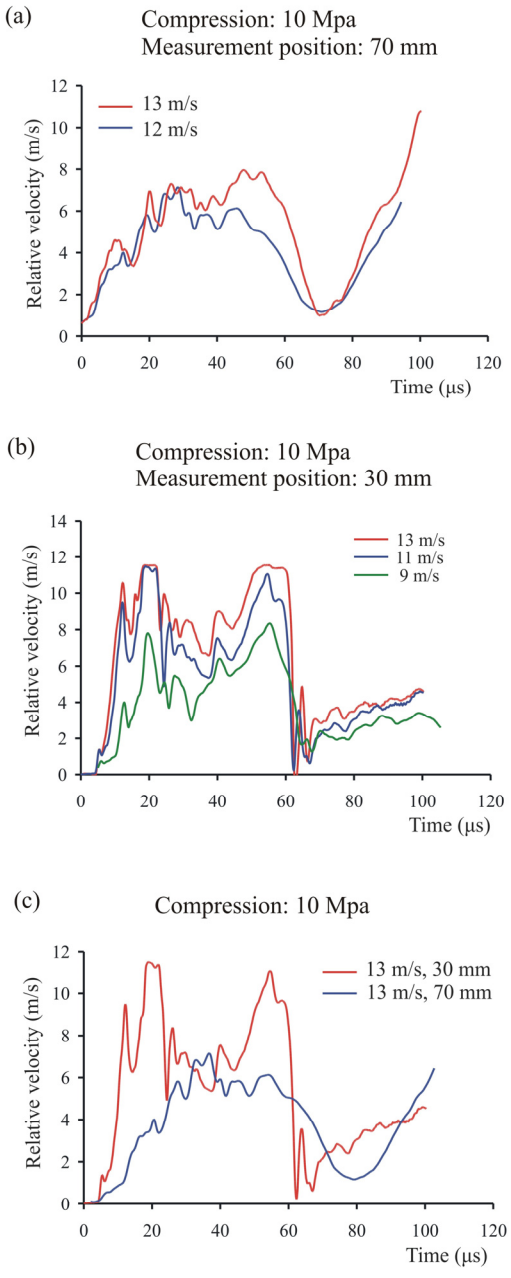

Figure 7 (a) Comparison of the horizontal in-plane relative velocity histories of points M_1 and M_2, located at distances of $70\,mm$ from the impact side of the Homalite plate, for different impact speeds. (b) Comparison of the horizontal in-plane relative velocity histories of points M_1 and M_2, located at distances of $30\,mm$ from the impact side of the Homalite plate, for different impact speeds. (c) Comparison of the horizontal in-plane relative velocity histories of points M_1 and M_2, located at distances of $70\,mm$ and $30\,mm$ from the impact side of the Homalite plate, for the same impact speed of $13\,m/s$. In all cases, the external compression is $10\,MPa$.

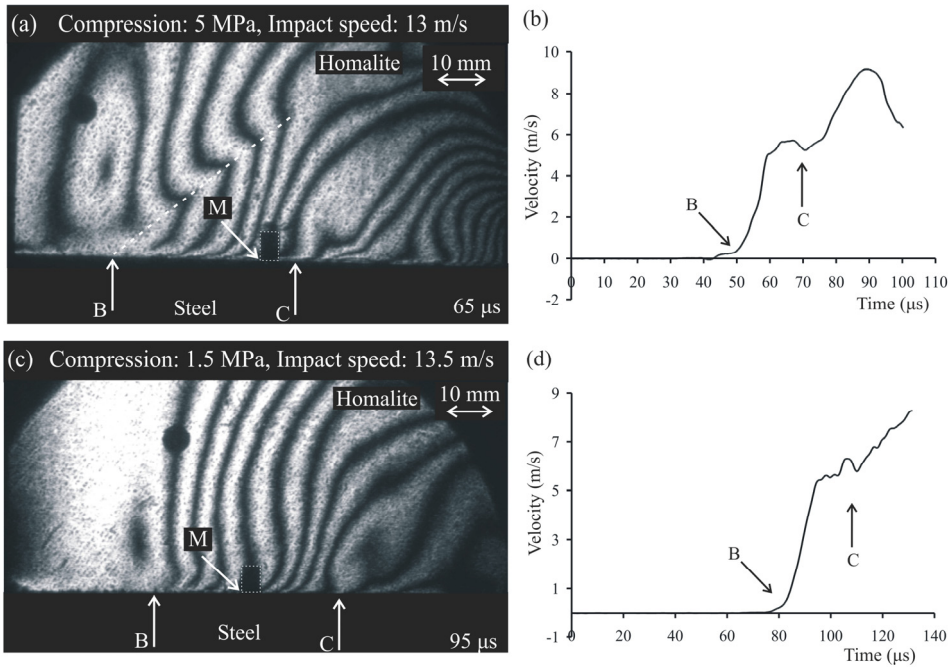

Figure 8 (a) and (c) Isochromatic fringe pattern captured during two different experiments. The supershear sliding initiated at B, whereas the wrinkle-like pulse is located at C. The dotted line highlights the Mach line. (b) and (d) Histories of the horizontal components of the in-plane particle velocity measured on the Homalite plate, $70\,mm$ from its impact side.

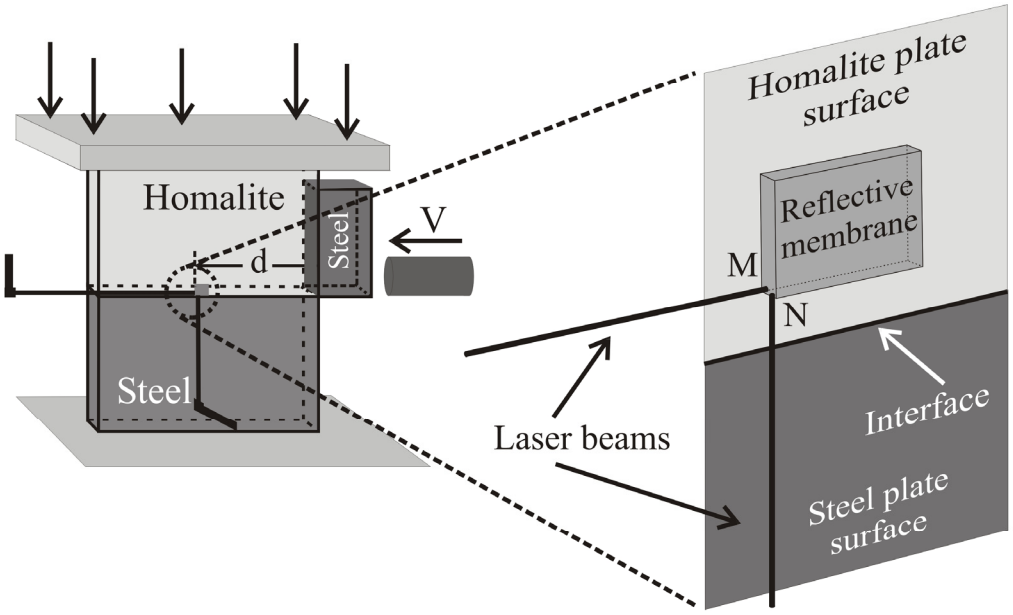

Figure 9 Schematic illustration of the experimental configuration for the simultaneous measurement of the horizontal and vertical components of the particle velocity. The area inside the dotted line is shown magnified.

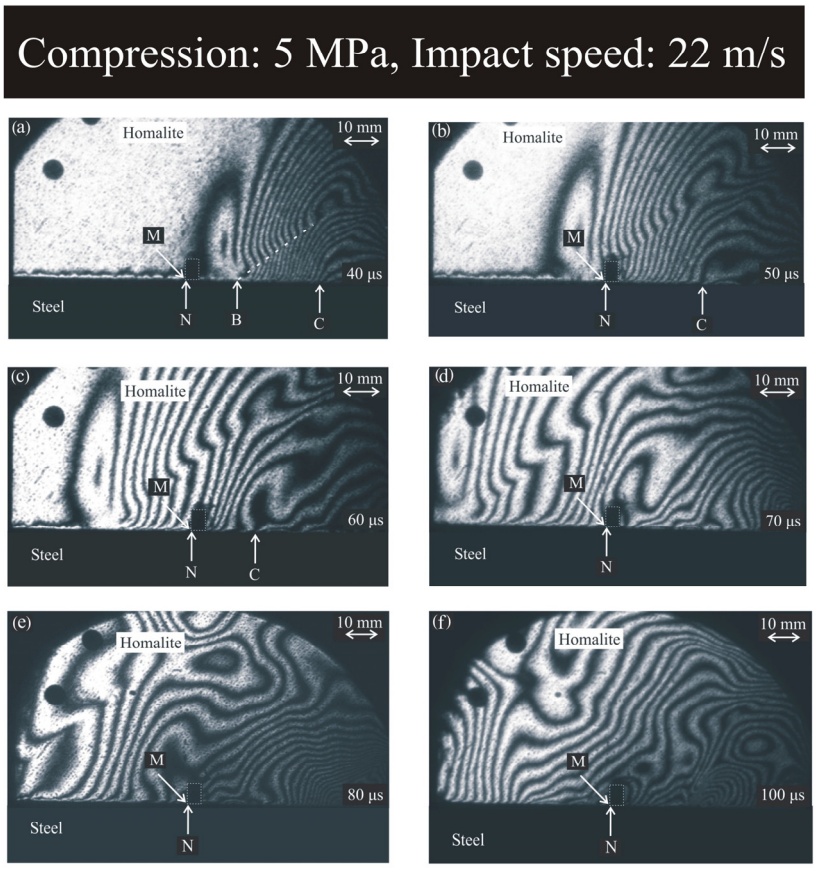

Figure 10 Sequence of isochromatic fringe patterns showing intersonic frictional sliding, the corresponding shear Mach line (B) and the wrinkle-like pulse (C). M and N are at the corner of the reflective membrane, where the horizontal and vertical in-plane components of the velocity were measured.

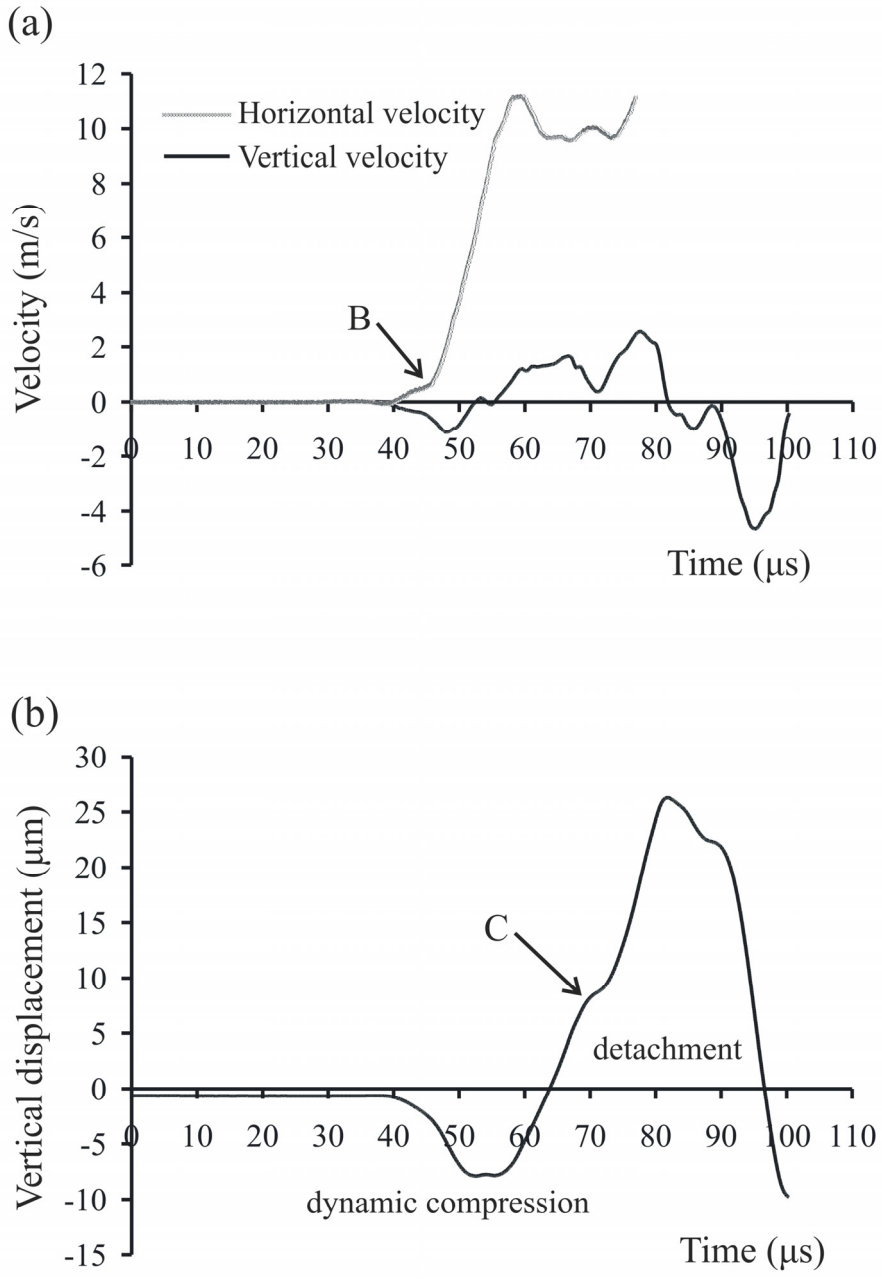

Figure 11 (a) Histories of the horizontal and the vertical components of the in-plane particle velocity measured on the Homalite plate, $70\,mm$ from its impact side. The sliding initiated at B. The confining stress was $5\,MPa$ and the impact speed was $22\,m/s$. (b) History of the vertical displacement.

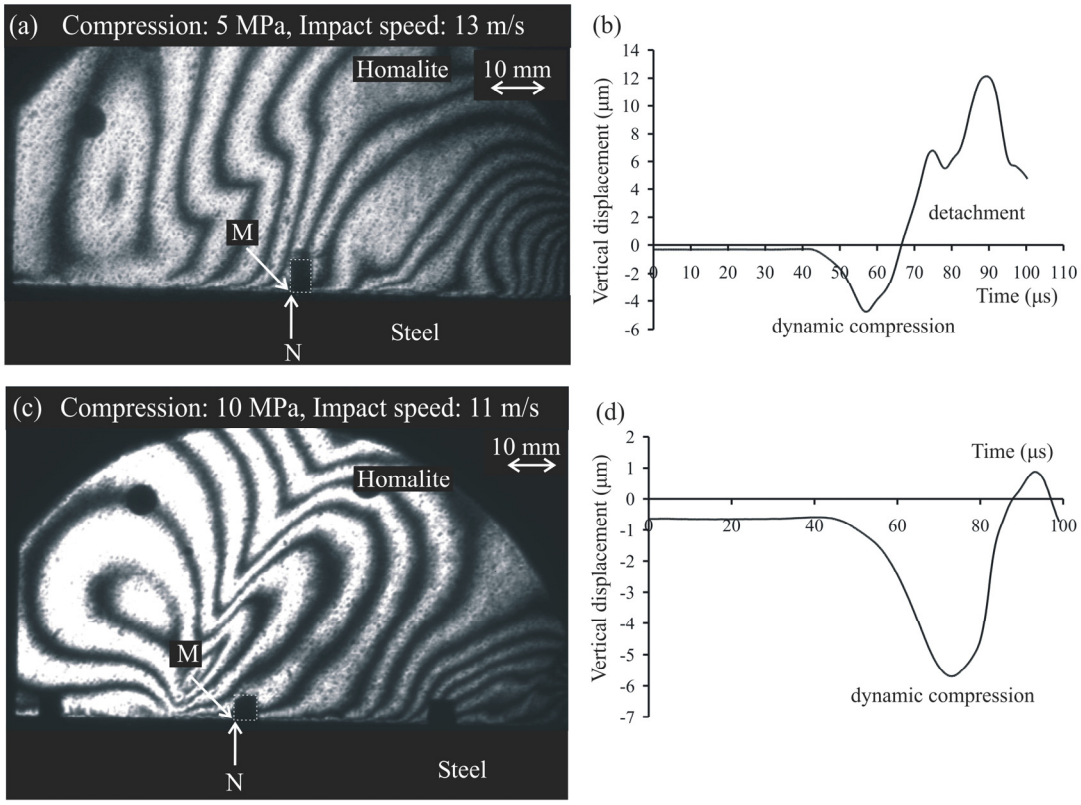

Figure 12 Representative isochromatic fringe patterns and corresponding vertical displacement histories measured on the Homalite plate, $70\,mm$ from its impact side.

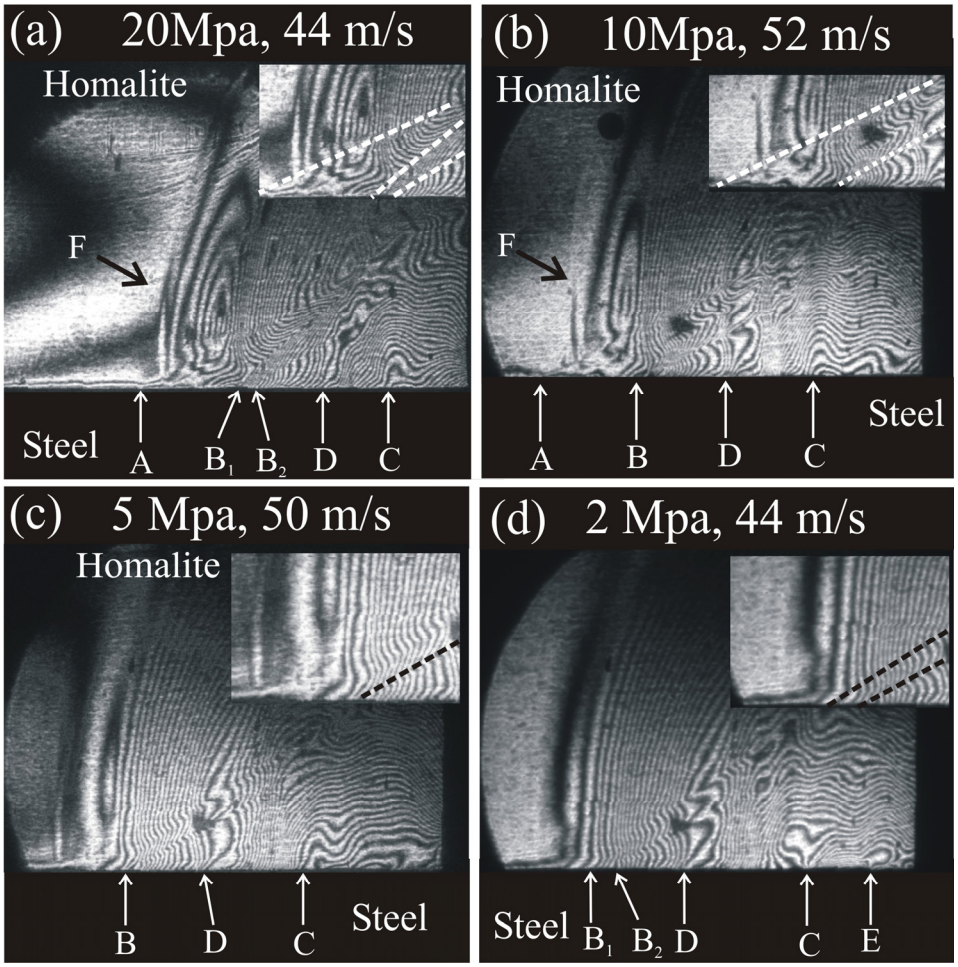

Figure 13 Representative isochromatic fringe patterns from two different experiments at high impact speeds. The specimens were subjected to different confining stresses. Arrow A indicates the position of the disturbance which created the head wave. The arrows B, C, D and F indicate the positions of the rupture tip, of the wrinkle-like pulse, of the fast interface disturbance and of the P-wave front respectively. The arrow E indicates a second wrinkle-like pulse. The arrow B_1 and B_2 indicate the positions of the sliding tips which are the origin of a transient double shock.

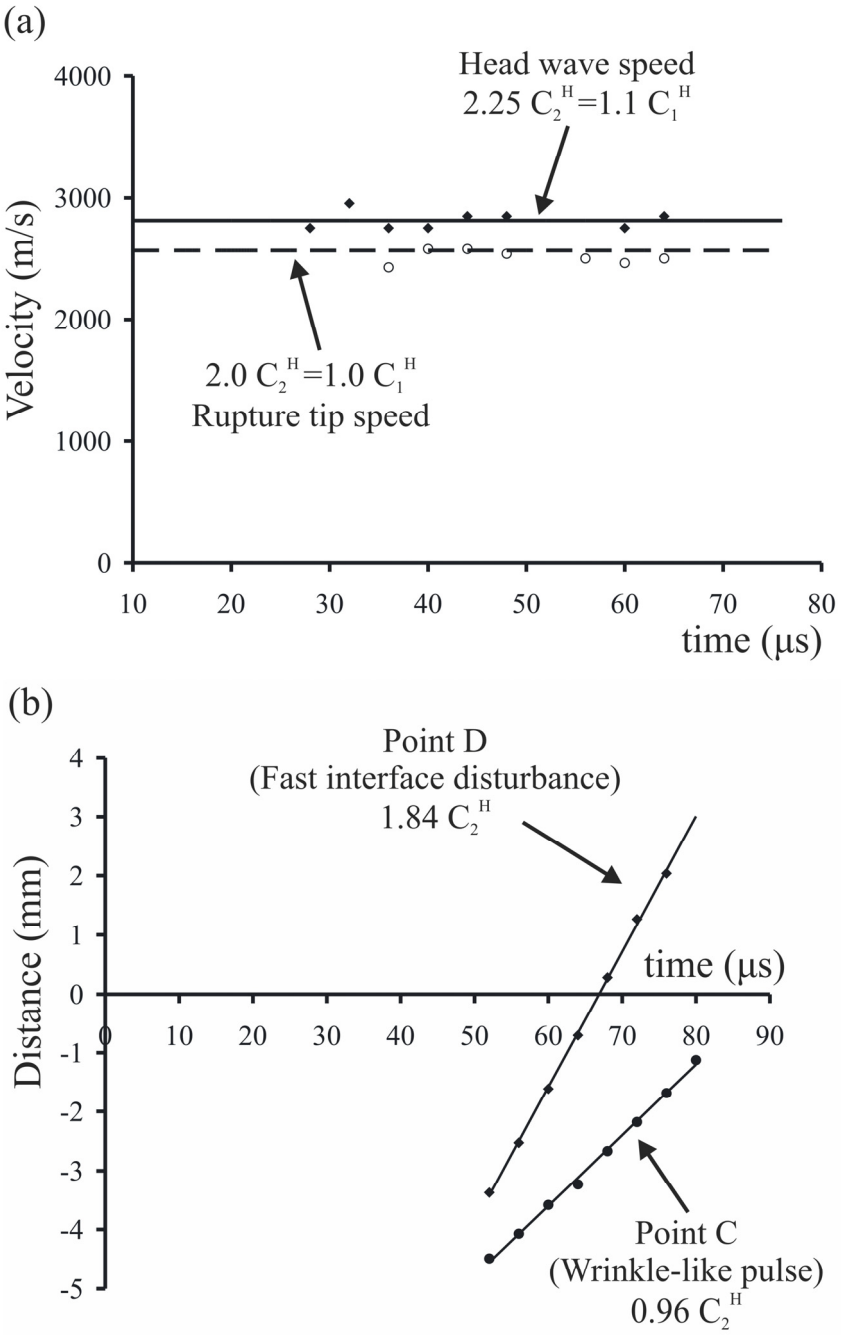

Figure 14 (a) Sliding tip speeds and head wave speeds at different frames measured using the Mach angle. (b) Positions of the wrinkle-like pulse and the fast interface disturbance as a function of time.

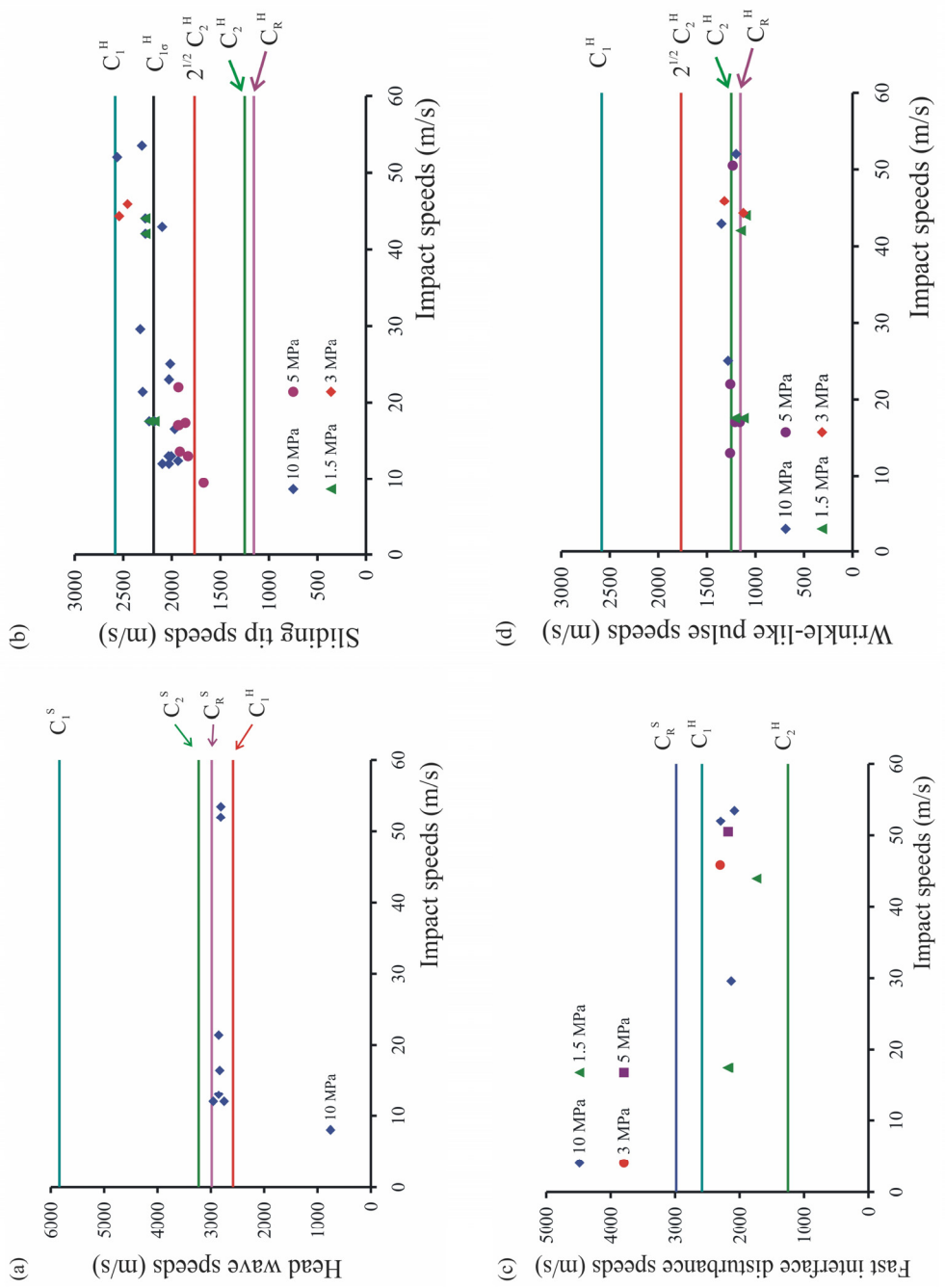

Figure 15 (a) The head wave speed is independent of the impact speed. (b) Variation of the sliding tip speed with the impact speed for various confining stresses. (c) The speed of the fast interface disturbance did not depend on the impact speed or on the confining stress. (d) The wrinkle-like pulse speed remained between the Rayleigh wave speed and the shear wave speed of Homalite-100, independent of the impact speed and the confining stress.

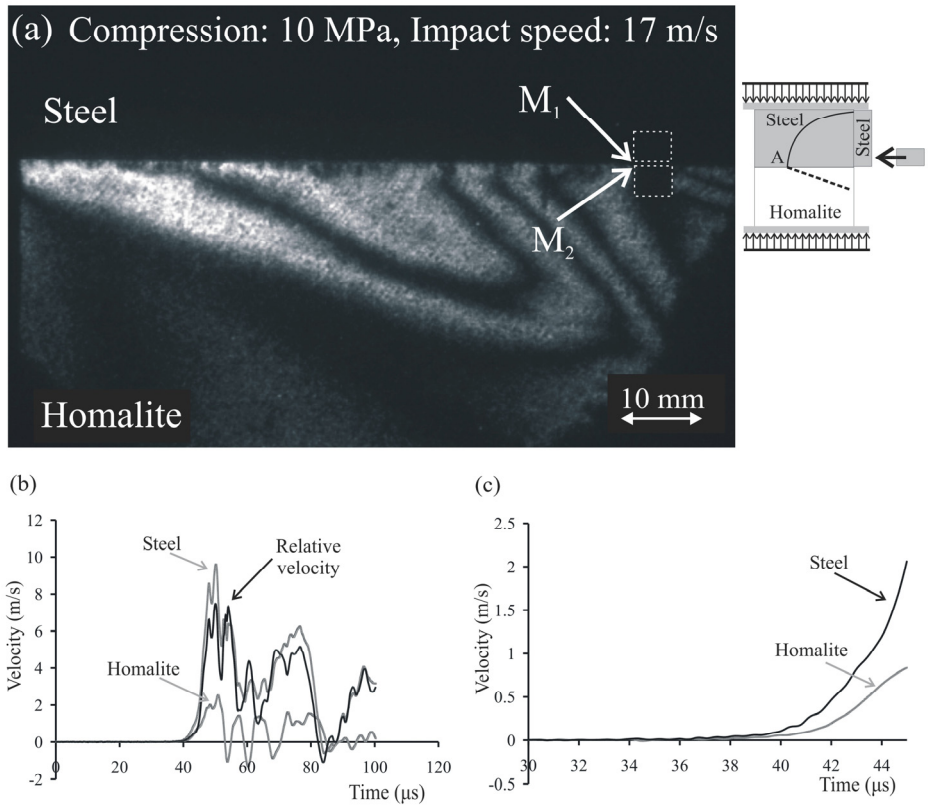

Figure 16 (a) Representative isochromatic fringe pattern from an experiment of sliding propagation initiated by impact on the steel plate. (b) Histories of the horizontal in-plane velocities and of the relative velocity, measured at two adjacent points M_1 and M_2, $30\,mm$ from the impact side of the Homalite plate. (c) Detail of the velocities histories diagram.

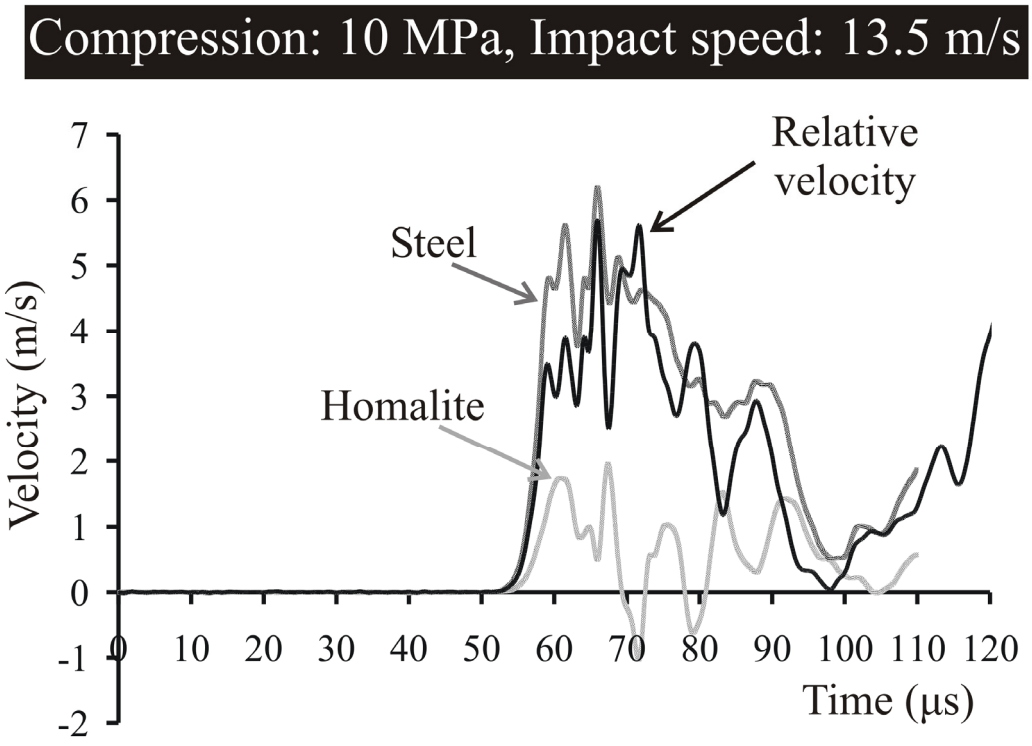

Figure 17 Histories of the horizontal in-plane velocities and of the relative velocity, measured at two adjacent points across the interface, $30\,mm$ from the impact side of the Homalite plate.

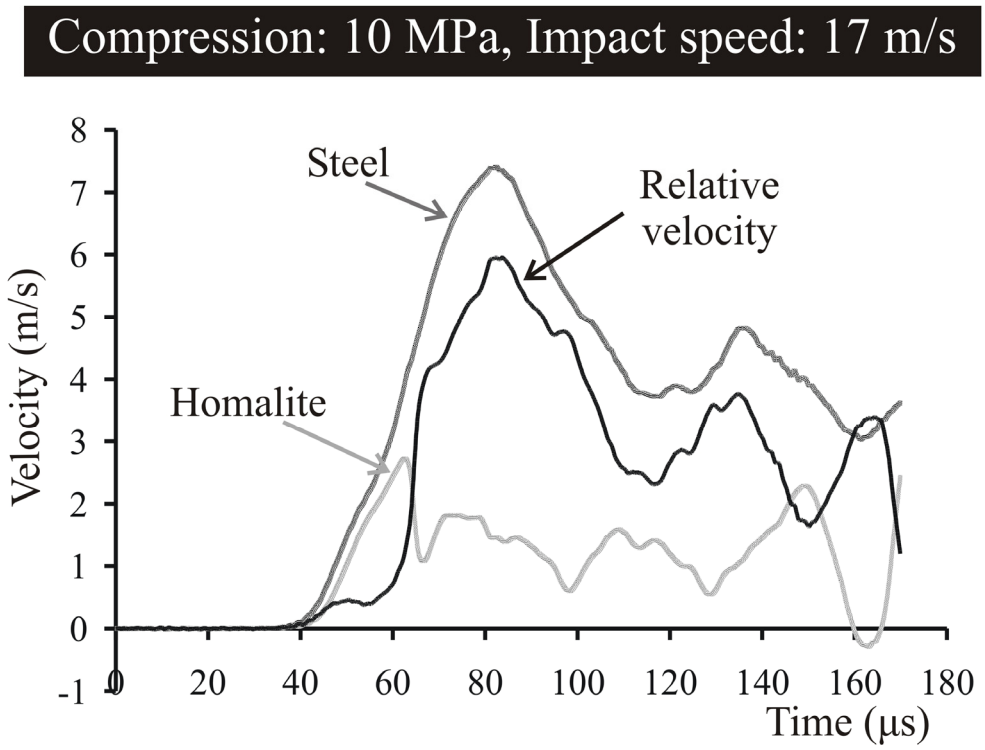

Figure 18 Histories of the horizontal in-plane velocities and of the relative velocity, measured at two adjacent points across the interface, $110\,mm$ from the impact side of the Homalite plate.

Chapter 4

DYNAMIC FRICTIONAL SLIDING ALONG INCOHERENT INTERFACES OF HOMOGENEOUS SYSTEMS AT LOW IMPACT SPEEDS

4.1 Introduction

In this chapter, dynamic sliding along incoherent (frictional) interfaces in homogeneous systems is investigated. Such interfaces (faults) along with their rupture behavior (frictional sliding) are of great interest not only to mechanics but also to seismology. A central issue in the modeling of earthquake rupture is the duration of slip at a point on the fault compared to the duration of the rupture of the entire fault (Rice 2001). The most classic approach of seismic rupture uses shear crack models (Broberg 1999; Freund 1990; Rosakis 2002), where the slip duration at a point ("rise time") is a significant fraction of the overall rupture propagation time. The crack-like mode has been generated in many numerical simulations of spontaneous rupture when a rate-independent friction law was implemented (Madariaga 1976; Andrews 1976 and 1985; Das and Aki 1977; Day 1982; Ruppert and Yomogida 1992; Harris and Day 1993). It has been pointed out, however, that inversions of seismic data for slip histories from well-recorded events (Heaton 1982 and 1990; Hartzell and Heaton 1983; Liu and Helmberger 1983; Mendoza and Hartzell 1988 and 1989) indicate that the duration of slip at a point on the fault was one order of magnitude shorter than the event duration, giving rise to the concept of a pulse-like rupture mode. Some eyewitness accounts also reported short slip duration (Wallace 1983; Pelton, Meissner and Smith 1984).

The concept of a pulse-like rupture went against a widely accepted view of how seismic rupture occurs. Its introduction was followed by various efforts to elucidate the physics leading to this process through analytical and numerical investigations. Different mechanisms for "self-healing" pulse generation along a homogeneous fault have been proposed. One postulation is that if the fault strength is low immediately behind the rupture front and is increased rapidly at a finite distance, then slip might be restricted to a short, narrow propagating area (Brune 1976). Recent theoretical and numerical investigations show that a strong velocity-weakening friction law model could indeed allow for pulse-like behavior of rupture under certain conditions (Zheng and Rice 1998). However, simulations utilizing velocity weakening have sometimes resulted in crack-like rupture and sometimes in "self-healing" pulse propagation (e.g., Cochard and Madariaga 1994 and 1996; Perrin, Rice and Zheng 1995; Beeler and Tullis 1996; Ben-Zion and Rice 1997; Lapusta et al. 2000; Cochard and Rice 2000; Nielsen, Carlson and Olsen 2000; Coker et al. 2005; Lapusta 2005). Friction laws along faults between two identical elastic solids have to include laboratory-based state evolution features and they must not exhibit ill-posedness or paradoxical features (Cochard and Rice 2000; Ranjith and Rice 2001). It has been proven that generalized rate and state friction laws are appropriate candidates for uniform faults (Cochard and Rice 2000; Ranjith and Rice 2001; Rice, Lapusta and Ranjith 2001; Zheng and Rice 1998). Within the frame of rate and state friction laws, the following three requirements have to be fulfilled for rupture to occur as a "self-healing" pulse (Zheng and Rice 1998; Rice 2001). One requirement is that the friction law must include strengthening with time on slipped portions of the fault that are momentarily in stationary contact (Perrin,

Rice and Zheng 1995). Another is that the velocity weakening at high slip rates must be much greater than that associated with the weak logarithmic dependence observed in the laboratory during low-velocity sliding experiments. Lastly, the third requirement is that the overall driving stress has to be lower than a certain value, but high enough to allow for self-sustained pulse propagation (Zheng and Rice 1998).

While strong velocity weakening is a mechanism which explains the onset of short duration slip-pulses along faults which separate similar materials, it is important to note that other mechanisms exist as well. One involves geometric confinement of the rupture domain by unbreakable regions (barrier model). That is, an earthquake consists of a number of short duration, crack-like ruptures on a small rupture area that are separated by locked regions (Aki, 1979; Papageorgiou and Aki 1983a and 1983b). In one implementation of this scenario, a pulse-like rupture behavior was found in a 3D geometry when the rupture process was confined within a long but narrow region by unbreakable barriers (Day 1982). It was observed that the rupture started in a classic crack-like mode and it propagated in all directions. After some time, arresting waves arrived from the boundaries and they effectively relocked the fault behind the rupture front, resulting in two slip pulses. Alternatively, a rupture nucleates and propagates bilaterally, but may arrest suddenly at a strong barrier at one end. Following its arrest, the reflected waves from the barrier spread back and heal the rupture surface. The combination of the still-propagating end of the rupture with the healing reflected wave forms a moving pulse-like configuration (Johnson 1990).

Since friction depends on normal stress, variations in normal stress on the rupture interface are also thought to be responsible for pulse formation (Richardson and Marone 1999). For example, expansion of pore fluid, caused by frictional heating, can dramatically reduce the effective normal stress and consequently the frictional stress. Pore pressure, however, may rapidly decrease behind the rupture tip, causing re-strengthening and possibly locking of the fault.

The possibility of generating wrinkle-like pulses along incoherent frictional interfaces in homogeneous systems is also investigated in this chapter. Comninou and Dundurs 1977 found that self-sustained slip waves with interface separation (detachment waves or wrinkle-like slip pulses) can propagate along the interface of two identical solids, which are pressed together. The constant propagation speed of these waves was found to be between the Rayleigh wave speed and the shear wave speed of the material. It is known that a system consisting of two identical half-planes and subjected to compression and to far field shear loading cannot sustain the propagation of a wrinkle-like pulse along the interface. In the setup used in our investigation, however, the loading was not strictly shear and there is not any physical reason to exclude the possibility of a wrinkle-like pulse.

4.2 Specimen Configuration and Loading

In order to investigate the physical plausibility of generating the two rupture modes described above, a number of well-controlled experiments involving dynamic sliding along incoherent (frictional) interfaces in homogeneous systems were performed. Two Homalite-100 plates, subjected to a uniform compressive stress, were frictionally held along the

interface. The top plate was also subjected to an impact shear loading (Figure 1). Each of the plates was $139.7\,mm$ long, $76.2\,mm$ wide and $9.525\,mm$ thick. All the experiments were executed at the same external confining stress of $P = 10\,MPa$, applied by a calibrated press. Homalite-100 is a brittle polyester resin that exhibits stress-induced birefringence and is mildly rate-sensitive. At the strain rate developed during our experiments (on the order of $10^3\,s^{-1}$) and at room temperature, Homalite exhibits a purely linear elastic behavior. The pressure, shear and Rayleigh wave speeds of Homalite-100 are $C_P = 2187\,m/s$, $C_S = 1249\,m/s$ and $C_R = 1155\,m/s$ respectively. The asymmetric impact loading was imposed via a cylindrical steel projectile with a diameter of $25.4\,mm$ and length of $50.8\,mm$, fired using a gas gun. The impact speeds ranged from $10\,m/s$ to $20\,m/s$ in the study of horizontal sliding and from $9\,m/s$ to $28\,m/s$ in the study of the vertical displacement along the interface. A steel buffer $73\,mm$ high, $25.4\,mm$ long and $9.525\,mm$ thick was attached to the impact side of the upper plate to prevent shattering and to induce a more or less planar loading wave.

4.3 Experimental Techniques

Dynamic photoelasticity, which depicts full-field contours of maximum shear stress, was combined with a newly-developed laser interferometry-based technique, which gives a local measurement of the sliding velocity at the interface (Figure 2). The results were registered in a microsecond time scale. The evolution of the isochromatic fringe pattern was recorded by a high-speed digital camera. In most of the experiments, the recording

frame rate was 1 frame per $4\mu s$. A collimated laser beam with a diameter of $130\,mm$ was used to illuminate most of the specimen. A pair of independent fiber-optic velocimeters was used to continuously measure the horizontal particle velocities at two adjacent points M_1 and M_2 across the interface. A schematic illustration of the experimental setup is shown in Figure 2b. The vertical distance of each point from the interface was less than $250\mu m$ before deformation. Both points had the same horizontal distance from the impact side of the Homalite plates. By subtracting the velocity of the point below the interface (M_2) from that of the point above the interface (M_1), the horizontal relative velocity history was obtained. The velocimeter consists of a modified Mach-Zehnder interferometer and a velocity decoder. The decoder was set to a full range scale of $\pm 10\,m/s$ with a maximum frequency of $1.5\,MHz$ and a maximum acceleration of $10^7\,g$. The beam spot size was approximately $70\mu m$, whereas the error of the velocity measurements was 1%. A Nicolet Integra 40 digital oscilloscope was used to record the output voltage of the velocimeter. The technique and the corresponding experimental setup are presented in detail in chapter 2 and in Lykotrafitis, Rosakis and Ravichandran 2005.

4.4 Experimental Results

4.4.1 Initiation of Dynamic Frictional Sliding

We start with the investigation of dynamic sliding initiation. The specimen (Figure 1) was subjected to a uniform confining pressure of $10\,MPa$, whereas the impact speed was $V = 24\,m/s$. An instantaneous isochromatic fringe pattern recorded at $40\mu s$ after impact is

displayed in Figure 3(a). An eye-like fringe structure is observed traveling, from right to left, behind the longitudinal wave front. At $40\,\mu s$, this structure has just arrived at the position where the horizontal particle velocities were measured. The pair of velocimeters was aimed at the adjacent points M_1 and M_2. Both points were at the same horizontal distance of $70\,mm$ from the impact side of the Homalite plate and at less than $250\,\mu m$ from the interface. Figure 3(c) shows the recorded in-plane horizontal velocities histories and the relative velocity history as well. In Figure 3(d), we focus on the time interval between $30\,\mu s$ and $52\,\mu s$, where the sliding initiation process took place. The red line corresponds to the horizontal velocity of point M_2 in the upper plane, the dark blue line corresponds to the horizontal velocity of point M_1 in the lower plane and the green line corresponds to the relative velocity. The longitudinal wave front arrived at the measurement position at $37\,\mu s$ (approximately $3\,\mu s$ before the arrival of the eye-like fringe structure there). At this time, the velocities of both points M_1 and M_2 commenced to rise. However, the relative velocity was almost zero until $45\,\mu s$, because the velocities of both points were practically the same. This fact shows that the longitudinal wave generated by the impact was traveling in the bulk of the two plates undisturbed by the interface and it caused the same acceleration for both points M_1 and M_2. At $45\,\mu s$ the relative velocity started to increase but it remained very low, less than $0.5\,m/s$, until approximately $50.5\,\mu s$. A numerical integration of the relative velocity with respect to time from $0\,\mu s$ to $50.5\,\mu s$ resulted in relative horizontal displacement of less than $2\,\mu m$ between points M_1 and M_2. This is explained by invoking the occurrence of an elastic shear deformation rather

than rupture (interfacial sliding) from $45\mu s$ until $50.5\mu s$. At that time, the relative velocity rose sharply and interfacial sliding began.

The above description of the sliding initiation mechanism agrees also with the high-speed photoelastic image captured at $50\mu s$ (Figure 3(b)). In this picture, the fringe concentration point A was just behind the measurement position. We thus establish that A is the rupture tip. The speed of A was obtained by following its position in various frames. The variation was very well approximated as linear and thus it was concluded that the propagation speed was constant. A linear interpolation resulted to a supershear rupture tip speed of $1.32C_S$. Consequently, two Mach lines forming a shear Mach cone emanated from the sliding tip. These Mach lines are highlighted by two dotted lines in Figures 3(a) and (b). Soon after the initiation of sliding, the horizontal velocity of point M_2, exceeded the value of $10m/s$, which is the instrument limit, and the recording was interrupted. In the experiments presented in the rest of the section, the impact speed was lower than $V = 24m/s$. We were, thus, able to continuously record the evolution of in-plane horizontal velocities for a long period of time and draw conclusions about the mode of the generated dynamic frictional sliding.

4.4.2 Visualizing Pulse-like and Crack-like Ruptures in the Laboratory

An instantaneous isochromatic fringe pattern obtained at an impact velocity of $V = 19m/s$ is shown in Figure 4(a). An eye-like fringe structure is again observed traveling, from right to left, behind the longitudinal wave front. The rupture tip A followed this fringe structure

at a supershear speed of $1.36C_S$. Consequently, two Mach lines forming a shear Mach cone emanated from the sliding tip. The tip can be located by tracing the Mach lines to the interface. The rupture tip speed which was obtained by two methods was found to be constant. First, we followed the position of the tip in various frames, as we did in the previous experiment. The variation was again very well-approximated as linear and thus it was concluded that the propagation speed was constant. The rupture tip speed was obtained by using a linear interpolation. In the second method, the Mach angle θ was measured, and by using the relationship $v = C_S / \sin\theta$ the rupture tip speed v was obtained frame by frame. Both methods gave consistent values for the propagation speeds.

The evolution over time of the horizontal relative velocity of two adjacent points M_2 and M_1, belonging to the upper and lower plate, respectively, at a distance of $70mm$ from the impact side of the Homalite plate, is displayed in Figure 4(b). The horizontal particle velocities of the adjacent points never exceeded the instrument limit value of $10m/s$ and were thus continuously recorded for a time period of $60\mu s$. The procedure of the initiation of sliding followed the same pattern as in the first experiment. When the longitudinal wave front arrived at the measurement positions M_1 and M_2 of Figure 4(a), where the pair of the interferometers was pointed, the velocities of both points started to increase. However, the relative horizontal velocity was zero for the next few microseconds and it remained very low for a time interval of approximately $13\mu s$. A numerical integration of the relative velocity with respect to time from $0\mu s$ to $13\mu s$ resulted in a relative horizontal displacement of $2\mu m$ between points M_1 and M_2. An elastic shear deformation arose

during the above period of time. The sliding started at approximately $13\mu s$ when the rupture tip (point A) arrived at the measurement position and the relative velocity increased sharply. After it reached its maximum value of approximately $6m/s$, it decreased and then it fluctuated, but never went below $4m/s$ during the recording time. As is evident from Figure 4(b), the sliding was continuous and thus we can safely say that rupture occurred in a classic crack-like mode.

As was already noted, the speeds of the rupture tips in the first two presented experiments were substantially higher than the shear wave speed of Homalite, and therefore the situation is similar to intersonic shear rupture propagation observed to occur along "coherent" and incoherent interfaces separating identical monolithic solids (Rosakis, Samudrala and Coker 1999 and 2000; Needleman 1999; Coker and Rosakis 2001; Samudrala, Huang and Rosakis 2002a and 2002b; Xia, Rosakis and Kanamori 2004). In the former experiments (Rosakis, Samudrala and Coker 1999 and 2000; Samudrala, Huang and Rosakis 2002a and 2002b), the "coherent" interfaces were bonded and they featured intrinsic strength and toughness in the absence of confining pressure. Unlike the present study, the resulting modes were always crack-like and the rupture speeds were not constant.

In contrast to these early shear crack growth experiments, the present work involves incoherent or frictional interfaces and static far-field compressive loading. Here, the frictional resistance to sliding depends on the normal stress through the friction law. The normal stress, however, is a superposition of the static externally-imposed pressure and a

dynamic (inertial) compression generated by the impact loading as follows. The P-wave produced by the impact loading creates a primarily horizontal compressive stress in the upper plate close to the interface, and due to the Poisson effect it also creates compression in the direction vertical to the interface. As the sliding proceeds, the vertical stress to the rupture interface changes, and thus the friction changes as well. The change in friction, however, affects the evolution of sliding. Thus, we infer that sliding is dependent on impact loading not only through the horizontal compression, which is the driving force for sliding, but also through the vertical compression which affects the resistance to sliding. Because of that dependence, essential changes in the rupture procedure are to be expected as the impact speed decreased.

Consistent with the above line of reasoning, further reduction of the impact speed to $17\,m/s$ resulted in drastic changes to the fringe pattern (Figure 5(a)) and to the horizontal relative velocity history of points M_1 and M_2 (Figure 5(b)). M_1 and M_2 were again located at a distance of $70\,mm$ from the impact side of the Homalite plate. The photoelastic images clearly show a fringe structure (located between points A_1 and A_2) traveling along the interface. Synchronizing the captured photoelastic frames with the horizontal relative velocity history, we were able to correlate the fringe concentration points A_1 and A_2 with abrupt changes in the horizontal relative velocity (Figure 5(b)). At A_1, the relative velocity increased rapidly and the sliding started. This signifies that A_1 was the rupture tip. In this experiment, however, the relative velocity, after it reached its maximum value of approximately $4\,m/s$, decreased significantly to $1.9\,m/s$ in a very short time interval of

about $7\mu s$. Thereafter, at A_2 the relative velocity increased again rapidly. This fact is reflected in the corresponding photoelastic fringe pattern as a fringe concentration point (Figure 5(a)). The propagation speeds of A_1 and A_2 were $1.19C_S$ and C_S respectively, within experimental error. The propagation speed of A_1 was supershear. However, the low impact speed of $17m/s$ produced a low-density fringe pattern, and the Mach lines emanating from A_1 were not well formed. The fringe structure (A_1A_2) was self-sustained. It also expanded with time, since the propagation speed of A_1 was higher than that of the propagation speed of A_2. Behind A_2, the relative velocity of points M_1 and M_2, after reaching a maximum value of approximately $5m/s$, decreased once again to $1.2m/s$ in a time interval of about $7\mu s$. At point A_3, which is almost at the left edge of the dark square area (Figure 5(a)), the relative velocity increased and remained high for the rest of the recording time. Point A_3 propagated at a sub-Rayleigh speed of $0.85C_S$ and signified the start of a clearly crack-like behavior of the rupture. By comparing the photoelastic fringe pattern evolution and the evolution of the relative velocity, it can be concluded that the rupture event was composed of two distinctive modes. From A_1 to A_3, the relative velocity changed rapidly twice in $13\mu s$, forming two pulses which were followed by a crack-like rupture mode which began at A_3.

By further decreasing the impact speed, a similar, albeit much simpler, behavior of the relative velocity was observed. Figure 6(a) shows an instantaneous isochromatic fringe pattern obtained at an impact speed of $15m/s$. The corresponding relative horizontal velocity history, measured at $30mm$ from the impact side of the Homalite plate, is shown

in Figure 6(b). By combining the horizontal relative velocity measurement with the recorded photoelastic frames, we can identify two rupture tips A_1 and A_2, which are fringe concentration points and are propagating along the rupture interface at speeds of $1.09C_S$ and $0.98C_S$ respectively. The deformation at the velocity measurement position was elastic until approximately $18\mu s$ when the rupture tip A_1 arrived there and sliding commenced. As in the previous case, the commencement of slip corresponds to an accumulated relative horizontal displacement of $2\mu m$ as well. Subsequently, the horizontal relative velocity increased rapidly from $0.6m/s$ to a local maximum of $2.5m/s$. After $5\mu s$, the relative velocity decreased abruptly back to $0.6m/s$ at point A_2 (Figure 6(b)). The slip ceased since the relative velocity was very low, allowing surface asperities to re-establish contact and be deformed elastically. The above observations show that the stable fringe structure (A_1A_2) represents a "self-healing" slip pulse of approximately $7\mu s$ in duration. Directly after the pulse, the relative velocity increased rapidly to $6.4m/s$ and retained its large value of approximately $4m/s$ for a long period of time, of about $40\mu s$. This suggests that the initial rupture of the pulse-like mode was immediately followed by a second rupture of the crack-like mode. Thus, as it has been anticipated, the experimental results presented up to this point indicate that the rupture process is very sensitive to impact speed. Indeed, as the projectile speed was decreased while keeping the external confining stress constant, the rupture tip speed was also decreased. Finally, the rupture mode changed from a crack-like mode to a mixed mode where either multiple slip pulses or a single "self-healing" slip pulse were followed by a crack.

By further reducing the impact speed to $10 m/s$, the rupture mode became purely pulse-like. The horizontal relative velocity was measured at a distance of $70 mm$ from the impact side of the Homalite plate and its evolution over time is shown in Figure 7. The rupture started at A_1 and propagated at a sub-Rayleigh speed of $0.76 C_S$, whereas after $15 \mu s$ the sliding ceased at A_2. The duration of sliding was very short compared to the approximately $100 \mu s$ duration of the impact event, and thus we infer that an isolated "self-healing" pulse was formed. Such a case clearly indicates that a pulse-like mode of rupture can definitely occur under appropriate conditions.

In the previous experiment, the speed of the rupture tip was relatively low and thus there was enough time for the reflective waves to arrive at the measurement position and to interfere with the incoming waves produced by the impact. In Figure 7(a), the characteristic shape of the eye-like fringe structure has been deformed because of the interaction between the incoming waves with the reflective waves. The formation of the pulse is due to this interaction. This way of producing a short duration slip at a given point bears strong similarities to the barrier model (Day 1982; Aki 1979; Papageorgiou and Aki 1983a and 1983b). There, the role of the barriers is played by the boundaries of the specimen. It is worth noting, however, that the formation of pulses in Figure 5 and Figure 6 cannot be explained by the barrier model, since these pulses featured very fast rupture tip speed and they were formed well before the reflective waves reached the measurement position. In these cases, we conjecture that the pulse formation was due either to the velocity-

weakening character of the friction law or to changes in the frictional resistance because of the variations in dynamic normal stress on the rupture interface.

In the last part of this section, the influence of confining stress on dynamic sliding is studied. Figure 8 displays the histories of the in-plane horizontal velocities and of the relative velocity of two adjacent points M_1 and M_2 at impact speeds on the order of $13 m/s$ and at three different uniform confining stresses. Points M_1 and M_2 were located at $70 mm$ from the impact side of the Homalite plate for all three experiments presented here. At a static pressure of $10 MPa$ and at an impact speed of $13.5 m/s$, Figure 8(a) shows that both points were moving at the same velocity for more than $20 \mu s$ (from a point before $40 \mu s$ until $60 \mu s$). For an additional period of $23 \mu s$ (from $60 \mu s$ until $83 \mu s$), points M_1 and M_2 traveled at similar velocities. This indicates that the deformation of the corresponding contact surfaces was elastic during the above period of time. Sliding initiated at $83 \mu s$ and continued until approximately $115 \mu s$, when the relative velocity became instantaneously zero. Then, a second period of sliding started. In this experiment, the high confining stress generated high frictional shear stress, which forced the two faces in contact to move locally together for more than $43 \mu s$. We would expect that this interval will decrease as the confining stress decreases.

Indeed, Figure 8(b) shows that at an external compression of $5 MPa$ and at an impact speed of $13 m/s$, points M_1 and M_2 were moving together for about $19 \mu s$ (from

approximately $42\,\mu s$ until $61\,\mu s$). It is also noted that the maximum velocity $7.5\,m/s$ of point M_2, in the upper plate where the impact occurred, was higher than the maximum velocity $6\,m/s$ of point M_2 in the previous experiment performed at $10\,MPa$ static compression. The maximum velocity of point M_1 in the lower plate, however, was approximately $2.5\,m/s$ at $5\,MPa$ compression, lower than $3\,m/s$ which was the maximum speed of point M_1 at $10\,MPa$ external compression. This is due to the fact that at lower external pressure the duration of the acceleration of point M_1 through friction was shorter at $5\,MPa$ than at $10\,MPa$ confining stress.

A similar behavior of the velocities of points M_1 and M_2 is inferred from the study of the results displayed in Figure 8(c). In this case, the uniform external pressure applied to the specimen was $1.5\,MPa$ and the impact speed was again $13\,m/s$. In that experiment, points M_1 and M_2 were moving together only for about $3\,\mu s$ before the initiation of sliding. The maximum velocity of point M_2 was approximately $7.5\,m/s$, whereas the maximum velocity of point M_1 was about $1.5\,m/s$, the lowest of the three cases. It is finally noted that the duration of the initial period of sliding decreased as the confining stress increased and the sliding mode transformed gradually from crack-like to pulse-like.

4.4.3 Wrinkle-like Pulses along Interfaces in Homogeneous Systems

Experiments performed at $10\,MPa$ and at impact speeds on the order of $20\,m/s$ generated a rich isochromatic fringe pattern. High-speed photoelastic images captured during these

experiments show that a very robust fringe structure propagated behind the rupture tip (e.g., fringe formation indicated by the arrow B in Figure 10(a)). A similar fringe structure has been observed in the experiments involved bimaterial interface in chapter 3. It was proved that a wrinkle-like pulse (detachment wave), propagated along the interface, caused the formation of the above fringe structure. Prompted by this similarity, we decided to investigate if a wrinkle-like pulse was once more responsible for the generation of the fringe structure observed here, in the case of identical plates interface. It is known that a system consisting of two identical half-planes and subjected to compression and to far field shear loading cannot sustain a wrinkle-like pulse propagating along the interface. In the setup used in this experiment, however, the loading was not strictly shear and there is not any physical reason to exclude the possibility of a wrinkle-like pulse. A pair of independent velocimeters was employed to measure the vertical in-plane components of the velocities of two adjacent points M_1 and M_2, located across the interface. Adding algebraically the corresponding velocities, the relative vertical velocity can be obtained. The arrangement of the velocimeters is shown schematically in Figure 9(a), whereas a picture of the real setup is shown in Figure 9(b).

An instantaneous isochromatic fringe pattern obtained at confining stress of $10\,MPa$ and at an impact speed of $28\,m/s$ is shown in Figure 10(a). The rupture tip A was propagating at a constant supershear speed of $1.49\,C_S$. A shear Mach cone is clearly visible in the photoelastic image. A fringe structure located at point B, in Figure 10(a), was propagating at a speed of $0.96\,C_S$. The time evolution of the relative vertical displacement of points M_1

and M_2, which were located $70\,mm$ from the impact side of the Homalite plate, is displayed in Figure 10(b). A simple 1-D calculation shows that the initial static compression of $10\,MPa$ caused a negative relative displacement of approximately $1.3\,\mu m$. Negative relative displacement means that the two points approached each other under compression. The P-wave front arrived at about $2.5\,\mu s$ after the triggering of the oscilloscope. Because of the Poisson effect, the horizontal dynamic (inertial) compression generated a vertical dynamic compression in addition to static compression. A negative relative displacement was caused by the dynamic compression. The rupture point crossed the velocity measurement position at approximately $10\,\mu s$ and it did not cause any visible change to the vertical components of the velocities of points M_1 and M_2. The relative displacement became positive at approximately $31\,\mu s$. The photoelastic picture, captured at $30\,\mu s$, clearly shows the fringe structure at B, which is under investigation, very close to the measurement position. The study of the entire set of the 16 recorded photoelastic images in combination with the relative vertical displacement history sheds light on the distribution of the dynamic compression along the interface during sliding. The interface was locally under dynamic compression immediately after the arrival of the P-wave front until the arrival of the mentioned fringe formation. The entire area from the rupture point A to the location of the fringe structure at B was sliding under compression. The length of the area AB was estimated to be approximately $40\,mm$, whereas the entire length of the interface was $139.7\,mm$. The fringe structure at B caused at least a decompression or even an opening locally at the interface. At approximately $42\,\mu s$ the relative vertical displacement became negative and the compression increased abruptly. During the rest of

the recording time the interface at the velocity measurement position was sliding under compression. We, thus, can relate the fringe structure at B to a wrinkle-like pulse propagating along the interface. As we quoted above, its propagation speed, perhaps not very surprisingly, was very close to $0.96C_S$ which lies in the interval between the shear and the Rayleigh wave speeds of the material. This issue will be discussed in detail in chapter 5.

At an impact speed of $18 m/s$ and at a static uniform compression of $10 MPa$, the fringe structure B in Figure 11(a) is not well-formed. This is due to the fact that the lower impact speed generated a lower dynamic compression and consequently a lower fringe density image and poorly formatted fringe structures. Figure 11(b) shows that the dynamic vertical compression was significantly lower than the vertical compression in Figure 10(b). The maximum positive vertical displacement, however, was almost the same in both cases. The relative displacement became positive at $93 \mu s$. The fringe structure at B was captured crossing the measurement position at $100 \mu s$ (Figure 11b). Later, at $121 \mu s$, a new period of compression started. Therefore, a wrinkle-like pulse can again be connected to the fringe structure at B.

We need to clarify why the vertical displacements in the above experiments are the same, while the impact speeds are quite different. This can be explained as follows: The high impact speed in Figure 10 created high vertical compression and thus the driving force for the wrinkle-like pulse formation had to overcome a high compressive stress. In the case of

Figure 11, however, the smaller driving force had to overcome a smaller dynamic compressive stress and finally generated the same positive vertical displacement as that in Figure 10. That is, the large driving force in Figure 10 was counterbalanced by the larger dynamic compressive stress which had to be overcome.

Reviewing the results from all the performed experiments, we verified that, at a confining stress of $10\,MPa$, the lowest impact speed which can generate a wrinkle-like pulse is approximately $17\,m/s$. Figure 12(a) displays an isochromatic fringe pattern obtained at a confining stress of $10\,MPa$ and at an impact speed of $9\,m/s$. It is clear that no fringe structure related to a wrinkle-like pulse appears. That is reflected by the relative vertical displacement history shown in Figure 12(b), where the maximum value of the displacement was only about $0.3\,\mu m$. A comparison of the photoelastic image shown in Figure 12(a) with photoelastic images obtained at the same static compression of $10\,MPa$ and at similar impact speeds during experiments where the horizontal particle velocities measurements were available, shows that the rupture started at point A.

In this section, the fringe structure at B was clearly related to the existence of a wrinkle-like pulse propagating along the interface. In the next chapter, further experimental results will strengthen the above correlation, showing that the propagation speed of the above fringe structure was always between the Rayleigh wave speed and the shear wave speed of Homalite. This result agrees with the theoretical prediction made by Comninou and Dunders 1977 for the propagation speed of the wrinkle-like pulses.

4.5 Conclusions

The experimental results presented in this chapter enlighten the sliding initiation process and provide conclusive evidence of the occurrence of various sliding rupture modes (crack-like, pulse-like or mixed) propagating dynamically along incoherent interfaces. Of particular interest here is the first experimental evidence of the formation of both supershear and sub-Rayleigh sliding pulses of the "self-healing" type, leading the first direct validation of predictions made on the basis of theoretical and numerical models of dynamic shear rupture. These pulses were found to propagate in the absence of interfacial opening. The experiments also provide hints of the dominant physical mechanisms governing the choice of various rupture modes and their evolution. It is also noted that wrinkle-like pulses (associated with interfacial opening and propagating at speeds between C_R and C_S) were discovered propagating along the interface for various loading conditions.

REFERENCES

Aki, K. Characterization of barriers on an earthquake fault. *J. Geophys. Res.* **84**, 6,140-148 (1979).

Andrews , D. J. Rupture propagation with finite stress in antiplane strain. *J. Geophys. Res.* **81**, 3575-3582 (1976).

Andrews, D. J. Dynamic plane-strain shear rupture with a slip-weakening friction law calculated by a boundary integral method. *Bull. Seismol. Soc. America* **75**, 1-21 (1985).

Beeler, N. M. & Tullis, T. E. Self-healing slip pulses in dynamic rupture models due to velocity-dependent strength. *Bull. Seismol. Soc. America* **86**, 1130-1148 (1996).

Ben-Zion, Y. & Rice, J. R. Dynamic simulations of slip on a smooth fault in an elastic solid. *J. Geophys. Res.* **102**, 17,771-17,784 (1997).

Broberg, K. B. *Cracks and fracture* (Academic Press, London, 1999).

Brune, J. N. The physics of earthquake strong motion. in *Seismic Risk and Engineering Decisions* (ed. Lomnitz, C. & Rosenbluth, E.) 141-171 (Elsevier, New York, 1976).

Cochard, A. & Madariaga, R. Dynamic faulting under rate-dependent friction. *Pure Appl. Geophys.* **142**, 419-445 (1994).

Cochard, A. & Madariaga, R. Complexity of seismicity due to highly rate-dependent friction. *J. Geophys. Res.* **105**, 25,891-25,907 (1996).

Cochard, A. & Rice, J. R. Fault rupture between dissimilar materials: Ill-posedness, regularization, and slip-pulse response. *J. Geophys. Res.* **105**, 25891-25907 (2000).

Coker, D. & Rosakis, A. J. Experimental observations of intersonic crack growth in asymmetrically loaded unidirectional composite plates. *Philosophical Magazine A* **81**, 571-595 (2001).

Coker, D., Lykotrafitis, G., Needleman, A. & Rosakis, A. J. Frictional sliding modes along an interface between identical elastic plates subject to shear impact loading. *J. Mech. and Phys. of Solids.* **53**, 884-922 (2005).

Comninou, M. and Dundurs, J. Elastic interface waves involving separation. *Journal of Applied Mechanics, ASME* **44**, 222-226 (1977).

Das, S. & Aki, K. A numerical study of two-dimensional spontaneous rupture propagation. *Geophys. J. Royal Astron. Soc.* **50**, 643-668 (1977).

Day, S. M. Three-dimensional finite difference simulation of fault dynamics: Rectangular faults with fixed rupture velocity. *Bull. Seismol. Soc. America* **72**, 705-727 (1982).

Freund, L. B. *Dynamic fracture mechanics* (Cambridge University Press, Cambridge, UK, 1990).

Harris R. A. & Day, S. M. Dynamics of fault interactions: parallel strike-slip faults. *J. Geophys. Res.* **98**, 4461-4472 (1993).

Hartzell, S. H. & Heaton, T. H. Inversion of strong ground motion and teleseismic waveform data for the fault rupture history of the 1979 Imperial Valley, California, earthquake. *Bull. Seismol. Soc. America* **73**, 1553-1583 (1983).

Heaton, T. H. The 1971 San Fernando earthquake; a double event? *Bull. Seismol. Soc. America* **72**, 2037-2062 (1982).

Heaton, T. H. Evidence for and implications of self-healing pulses of slip in earthquake rupture. *Phys. Earth Planet. In.* **64**, 1-20 (1990).

Johnson, E. On the initiation of unidirectional slip. *Geophys. J. Int.* **101**, 125-132 (1990).

Lapusta, N., Rice, J. R., Ben-Zion, Y. & Zheng, G. Elastodynamic analysis for slow tectonic loading with spontaneous rupture episodes on faults with rate- and state-dependent friction. *J. Geophys. Res.* **105**, 23,765-23,789 (2000).

Lapusta, N. Proceedings. SEM, Portland (2005).

Liu, H. L. & Helmberger, D. V. The near-source ground motion of the 6 August 1979 Coyote Lake, California, earthquake. *Bull. Seismol. Soc. America* **73**, 201-218 (1983).

Lykotrafitis, G., Rosakis, A. J. & Ravichandran, G. Particle Velocimetry and Photoelasticity Applied to the Study of Dynamic Sliding Along Frictionally-Held Bimaterial Interfaces: Techniques and Feasibility. *Exp. Mech.*, Accepted (2005).

Madariaga, R. Dynamics of an expanding circular fault. *Bull. Seismol. Soc. America* **66**, 639-666 (1976).

Mendoza, C. & Hartzell, S. H. Inversion for slip distribution using GDSN P waves: North Palm Springs, Borah peak, and Michoakan earthquakes. *Bull. Seismol. Soc. America* **78**, 1092-1111 (1988).

Mendoza, C. & Hartzell, S. H. Slip distribution of 19 September 1985 Michoacan, Mexico, earthquake: near-source and teleseismic constraints. *Bull. Seismol. Soc. America* **79**, 655-669 (1989).

Needleman, A. An analysis of intersonic crack growth under shear loading. *ASME, J. Appl. Mech.,* **66**, 847-857 (1999).

Nielsen, S. B., Carlson, J. M. & Olsen, K. B. Influence of friction and fault geometry on earthquake rupture. *J. Geophys. Res.* **105**, 6069-6088 (2000).

Papageorgiou, A. & Aki, K. A specific barrier model for the quantitative description of inhomogeneous faulting and the prediction of strong ground motion. I. Description of the model. *Bull. Seismol. Soc. America* **73**, 693-722 (1983a).

Papageorgiou, A. & Aki, K. A specific barrier model for the quantitative description of inhomogeneous faulting and the prediction of strong ground motion. II. Applications of the model. *Bull. Seismol. Soc. America* **73**, 953-978 (1983b).

Pelton, J. R., Meissner, C. W. & Smith K.D. Eyewitness account of normal surface faulting. *Bull. Seismol. Soc. America* **74**, 1083-1089 (1984).

Perrin, G. Rice, J. R. & Zheng, G. Self-healing slip pulse on a frictional surface. *J. Mech. Phys. Solids* **43**, 1461-1495 (1995).

Ranjith, K. & Rice, J. R. Slip dynamics at an interface between dissimilar materials. *J. Mech. and Phys. of Solids.* **49**, 341-361 (2001).

Rice, J. R. Mechanics for a New Millennium. in *Proceedings of the 20th International Congress of Theoretical and Applied Mechanics, 2000, Chicago* (ed. Aref, H. & Philips, J. W.) 1- 23 (Kluwer Academic Publishers, Dordrecht, 2001).

Rice, J. R., Lapusta, N. & Ranjith, K. Rate and state dependent friction and the stability of sliding between elastically deformable solids. *J. Mech. and Phys. of Solids* **49**, 1865-1898 (2001).

Richardson, E. & Marone, C. Effects of normal stress vibrations on frictional healing. *J. Geophys. Res.* **104**, 28,859-28,878 (1999).

Rosakis, A. J., Samudrala, O. & Coker, D. Cracks faster than the shear wave speed. *Science* **284**, 1337-1340 (1999).

Rosakis, A. J., Samudrala, O. & Coker, D. Intersonic shear crack growth along weak planes. *Mat. Res. Innov.* **3**, 236-243 (2000).

Rosakis, A. J. Intersonic shear cracks and fault ruptures. *Advances in Physics* **51**, 1189-1257 (2002).

Ruppert, S. D. & Yomogida, K. A crack-like rupture model for the 19 September 1985 Michoacan, Mexico, earthquake. *Pure and Appl. Geophys.* **138**, 407-427 (1992).

Samudrala, O., Huang, Y. & Rosakis, A. J. Subsonic and intersonic shear rupture of weak planes with a velocity weakening cohesive zone. *Journal of Geophysical Research* **107**, No B8, 10129/2001JB000460 (2002a).

Samudrala, O., Huang, Y. & Rosakis, A. J. Subsonic and intersonic mode II crack propagation with a rate-dependent cohesive zone. *J. Mech. and Phys. of Solids* **50**, 1231-1268 (2002b).

Wallace, R. E. Eyewitness account of surface fault during the earthquake of 28 October 1983 Borah peak, Idaho. *Bull. Seismol. Soc. America* **74**, 1091-1094 (1983).

Xia, K., Rosakis, A. J. & Kanamori, H. Laboratory earthquakes: The sub-Rayleigh-to-supershear rupture transition. *Science* **303**, 1859-1861 (2004).

Zheng, G. & Rice, J. R. Conditions under which velocity-weakening friction allows a self-healing versus a crack-like mode of rupture. *Bull. Seismol. Soc. America* **88**, 1466-1483 (1998).

List of Figures

Figure 1 A homogeneous system, consisting of two identical incoherent Homalite plates, is subjected to uniform compressive stress and to impact-generated shear loading.

Figure 2 (a) Dynamic photoelasticity setup. (b) Schematic illustration of the experimental configuration for the sliding velocity measurement. The area inside the dotted circle is shown magnified. Points M_1 and M_2 were at the same horizontal distance d from the impact side of the Homalite plate.

Figure 3 (a) and (b) Isochromatic fringe patterns captured at $40\mu s$ and $50\mu s$ respectively after impact. The external uniform compression was $10MPa$ and the impact speed was $24m/s$. The rupture tip is at the fringe concentration point A. The dotted lines highlight the location of the Mach lines emanating from the rupture tip. (c) Horizontal velocity histories and relative horizontal velocity history of points M_1 and M_2 located $70mm$ from the impact side of the Homalite plate. The rupture commenced when the rupture tip A reached the velocity measurement position. (d) Detail of the diagram displayed in (c).

Figure 4 (a) Isochromatic fringe pattern generated during an experiment for which the impact speed was $19m/s$ and the external compression was $10MPa$. The

rupture tip is at the fringe concentration point A. The inserts highlight the location of the Mach lines emanating from the rupture tip and the specimen configuration. (b) Relative velocity history of points M_1 and M_2 located at a distance of $70\,mm$ from the impact side of the Homalite plates. The rupture commenced when the rupture tip A reached the velocity measurement position.

Figure 5 (a) Isochromatic fringe pattern generated during an experiment for which the impact speed was $17\,m/s$ and the external compression was $10\,MPa$. The fringe concentration point A_1 is the rupture tip of the pulse-like rupture mode, A_2 is the rear edge of the first pulse and A_3 is the rear edge of the second pulse. The crack-like mode initiated at A_3 right after the second pulse. (b) Relative velocity history of points M_1 and M_2 located at a distance of $70\,mm$ from the impact side of the Homalite plates. The rupture commenced when the rupture tip A_1 reached the velocity measurement position and two pulses A_1A_2 and A_2A_3 were formed. The crack-like rupture mode initiated at A_3 right behind the second pulse.

Figure 6 (a) Isochromatic fringe pattern generated during an experiment for which the impact speed was $13\,m/s$ and the external compression was $10\,MPa$. The fringe concentration points A_1 and A_2 are the rupture tip and the rear edge respectively of the pulse-like rupture mode. The crack-like mode initiated at A_2 right after the pulse. (b) Relative velocity history of points M_1 and M_2 located at

a distance of $30\,mm$ from the impact side of the Homalite plates. The rupture commenced when the rupture tip A_1 reached the velocity measurement position and a pulse A_1A_2 was formed. The crack-like rupture mode initiated at A_2 right behind the second pulse.

Figure 7 (a) Isochromatic fringe pattern generated during an experiment for which the impact speed was $10\,m/s$ and the external compression was $10\,MPa$. The fringe concentration points A_1 and A_2 are the rupture tip and the rear-edge respectively of the "pulse-like" rupture mode. (b) Relative velocity history of points M_1 and M_2 located at a distance of $70\,mm$ from the impact side of the Homalite plates. The rupture commenced when the rupture tip A_1 reached the velocity measurement position and an isolated pulse A_1A_2 was formed.

Figure 8 (a) - (c) Horizontal in-plane velocity histories and horizontal in-plane relative velocity histories of points M_1 and M_2 located at a distance of $70\,mm$ from the impact side of the Homalite plate. The impact speeds are essentially the same, on the order of $13\,m/s$ for all three experiments, whereas the external compression decreases.

Figure 9 (a) Schematic illustration of the experimental configuration for the relative vertical velocity measurement. The area inside the dotted line is shown magnified. Points M_1 and M_2 are at the same horizontal distance from the

impact side of the Homalite plate. (b) Photography of the actual setup displaying the arrangement of the velocimeters' heads.

Figure 10 (a) Isochromatic fringe pattern generated during an experiment for which the impact speed was $28 m/s$ and the external compression was $10 MPa$. The rupture tip is at the fringe concentration point A and the wrinkle-like pulse is at point B. (b) Relative vertical displacement history of points M_1 and M_2, located at a distance of $70 mm$ from the impact side of the Homalite plate. The rupture tip and the wrinkle-like disturbance crossed the velocity measurement position at approximately $10 \mu s$ and $32 \mu s$ after triggering, respectively.

Figure 11 (a) Isochromatic fringe pattern generated during an experiment for which the impact speed was $18 m/s$ and the external compression was $10 MPa$. The rupture tip is at the fringe concentration point A and the wrinkle-like pulse is at point B. (b) Relative vertical displacement history of points M_1 and M_2 located at a distance of $70 mm$ from the impact side of the Homalite plate. The rupture tip and the wrinkle-like disturbance crossed the velocity measurement position at approximately $82 \mu s$ and $100 \mu s$ after impact, respectively.

Figure 12 (a) Isochromatic fringe pattern generated during an experiment for which the impact speed was $9 m/s$ and the external compression was $10 MPa$. The rupture tip is at the fringe concentration point A. No wrinkle-like pulse

appeared. (b) Relative vertical displacement history of points M_1 and M_2 located at a distance of $100\,mm$ from the impact side of the Homalite plate.

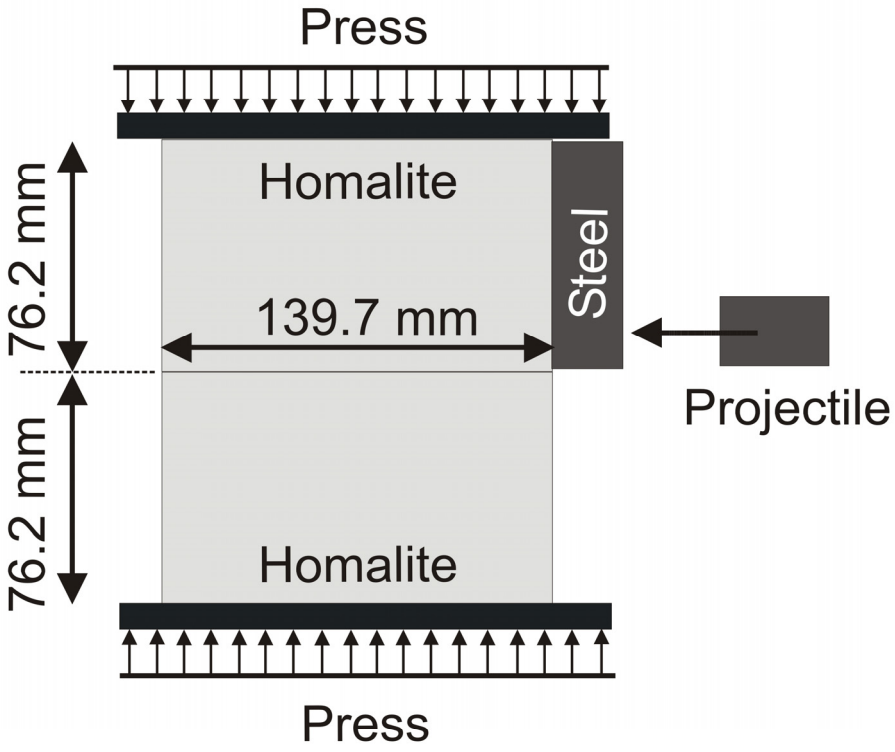

Figure 1 A homogeneous system, consisting of two identical incoherent Homalite plates, is subjected to uniform compressive stress and to impact-generated shear loading.

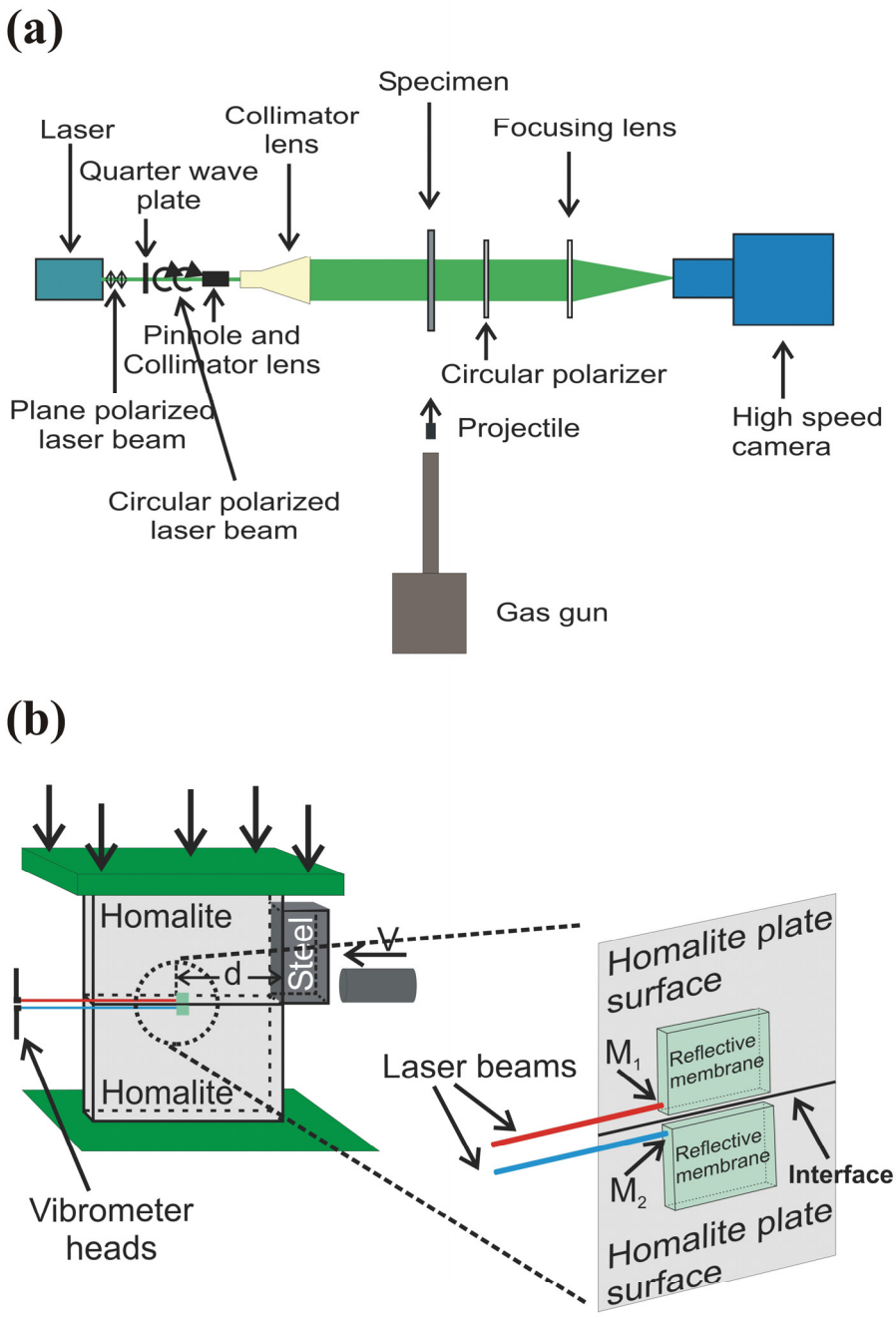

Figure 2 (a) Dynamic photoelasticity setup. (b) Schematic illustration of the experimental configuration for the sliding velocity measurement. The area inside the dotted circle is shown magnified. Points M_1 and M_2 were at the same horizontal distance d from the impact side of the Homalite plate.

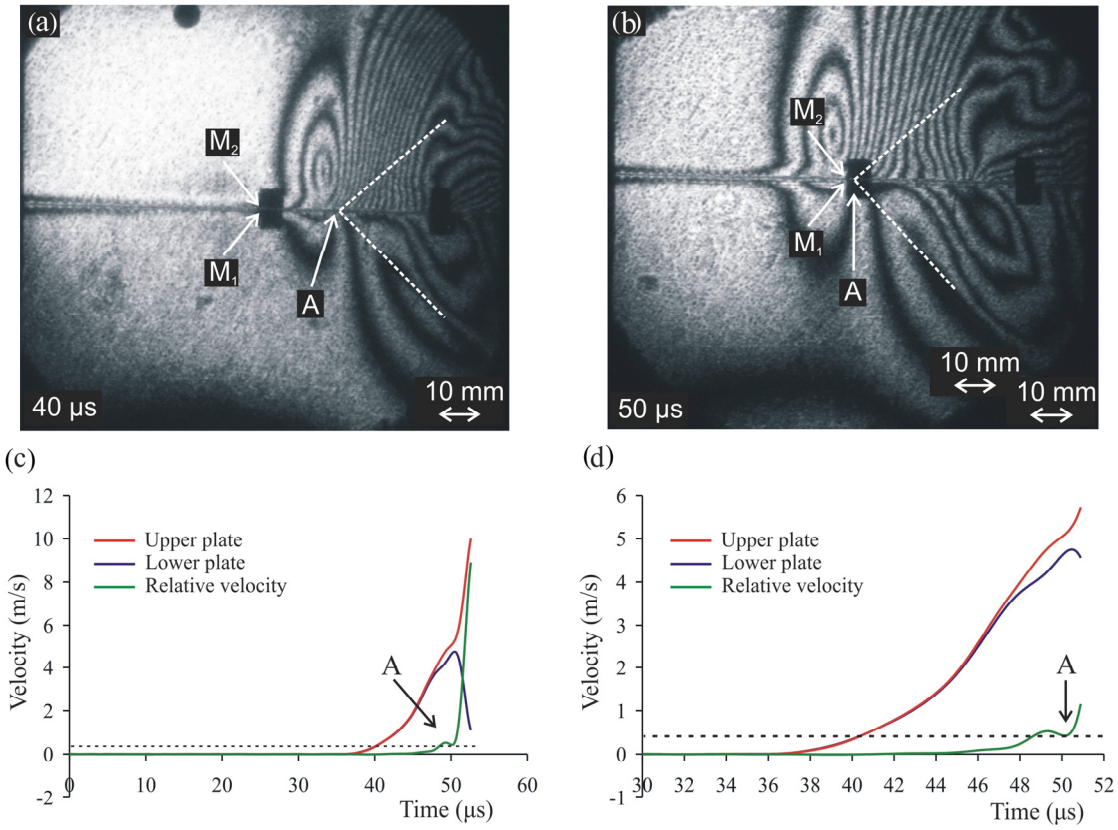

Figure 3 (a) and (b) Isochromatic fringe patterns captured at $40\mu s$ and $50\mu s$ respectively after impact. The external uniform compression was $10MPa$ and the impact speed was $24m/s$. The rupture tip is at the fringe concentration point A. The dotted lines highlight the location of the Mach lines emanating from the rupture tip. (c) Horizontal velocity histories and relative horizontal velocity history of points M_1 and M_2 located $70mm$ from the impact side of the Homalite plate. The rupture commenced when the rupture tip A reached the velocity measurement position. (d) Detail of the diagram displayed in (c).

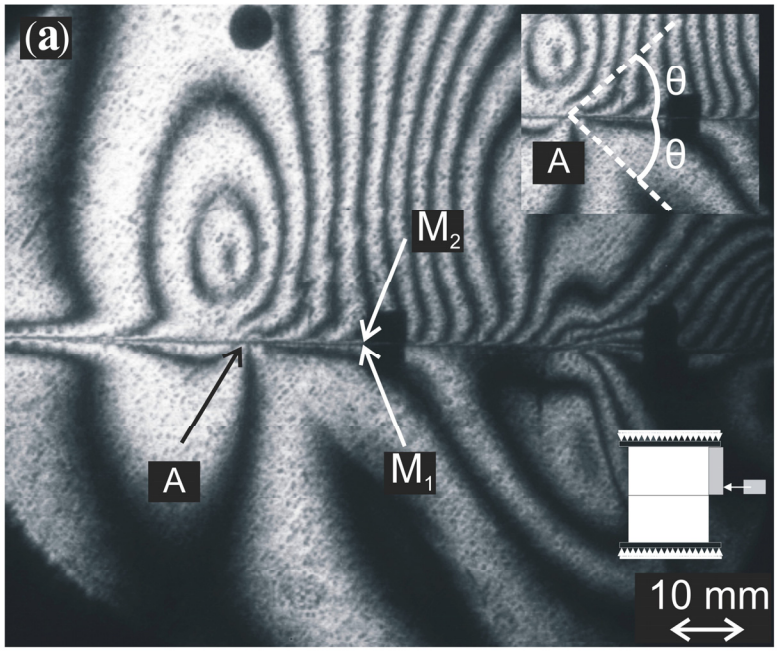

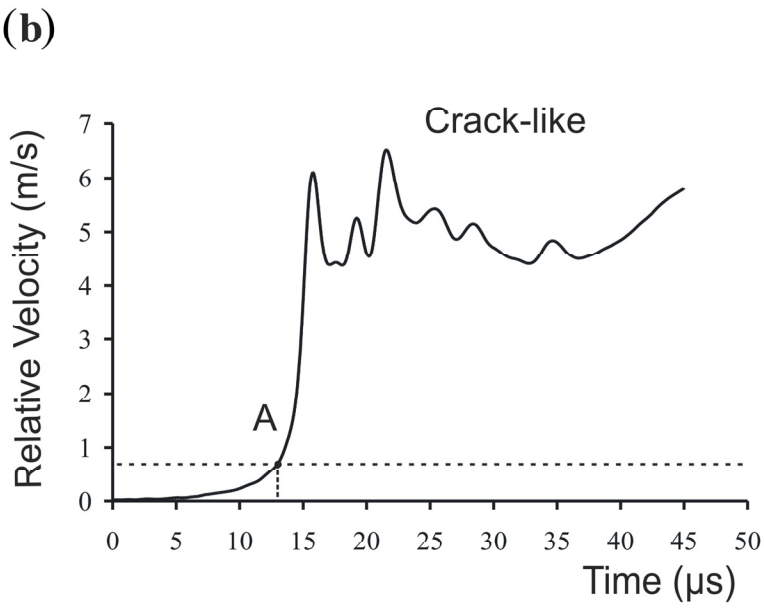

Figure 4 (a) Isochromatic fringe pattern generated during an experiment for which the impact speed was $19\,m/s$ and the external compression was $10\,MPa$. The rupture tip is at the fringe concentration point A. The inserts highlight the location of the Mach lines emanating from the rupture tip and the specimen configuration. (b) Relative velocity history of points M_1 and M_2 located at a distance of $70\,mm$ from the impact side of the Homalite plates. The rupture commenced when the rupture tip A reached the velocity measurement position.

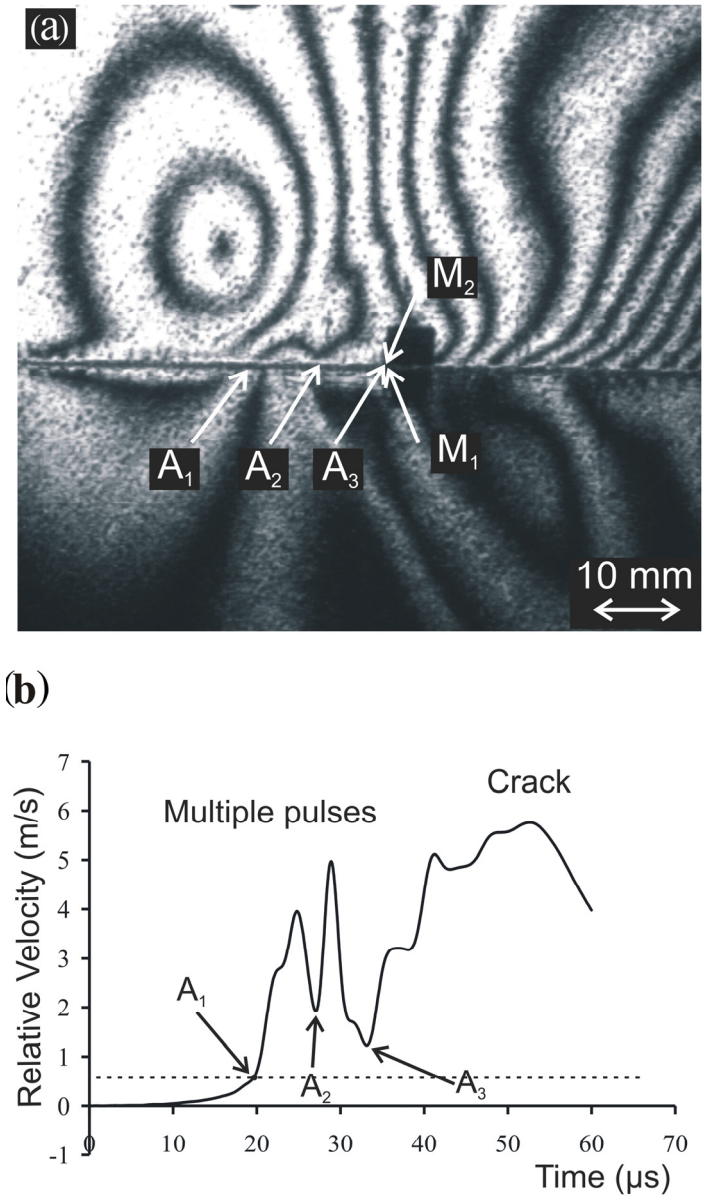

Figure 5 (a) Isochromatic fringe pattern generated during an experiment for which the impact speed was $17\,m/s$ and the external compression was $10\,MPa$. The fringe concentration point A_1 is the rupture tip of the "pulse-like" rupture mode, A_2 is the rear edge of the first pulse and A_3 is the rear edge of the second pulse. The "crack-like" mode initiated at A_3 right after the second pulse. (b) Relative velocity history of points M_1 and M_2 located at a distance of $70\,mm$ from the impact side of the Homalite plates. The rupture commenced when the rupture tip A_1 reached the velocity measurement position and two pulses A_1A_2 and A_2A_3 were formed. The "crack-like" rupture mode initiated at A_3, right behind the second pulse.

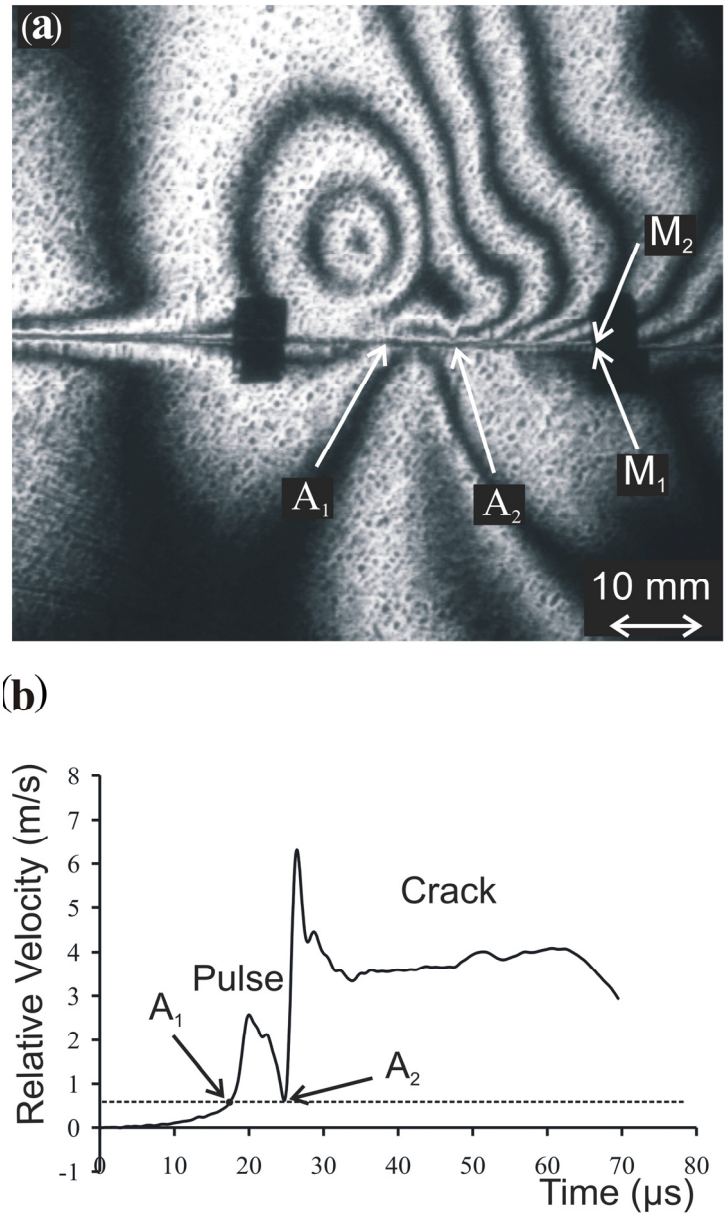

Figure 6 (a) Isochromatic fringe pattern generated during an experiment for which the impact speed was $15\,m/s$ and the external compression was $10\,MPa$. The fringe concentration points A_1 and A_2 are the rupture tip and the rear edge respectively of the "pulse-like" rupture mode. The "crack-like" mode initiated at A_2 right after the pulse. (b) Relative velocity history of points M_1 and M_2 located at a distance of $30\,mm$ from the impact side of the Homalite plates. The rupture commenced when the rupture tip A_1 reached the velocity measurement position and a pulse A_1A_2 was formed. The "crack-like" rupture mode initiated at A_2 right behind the second pulse.

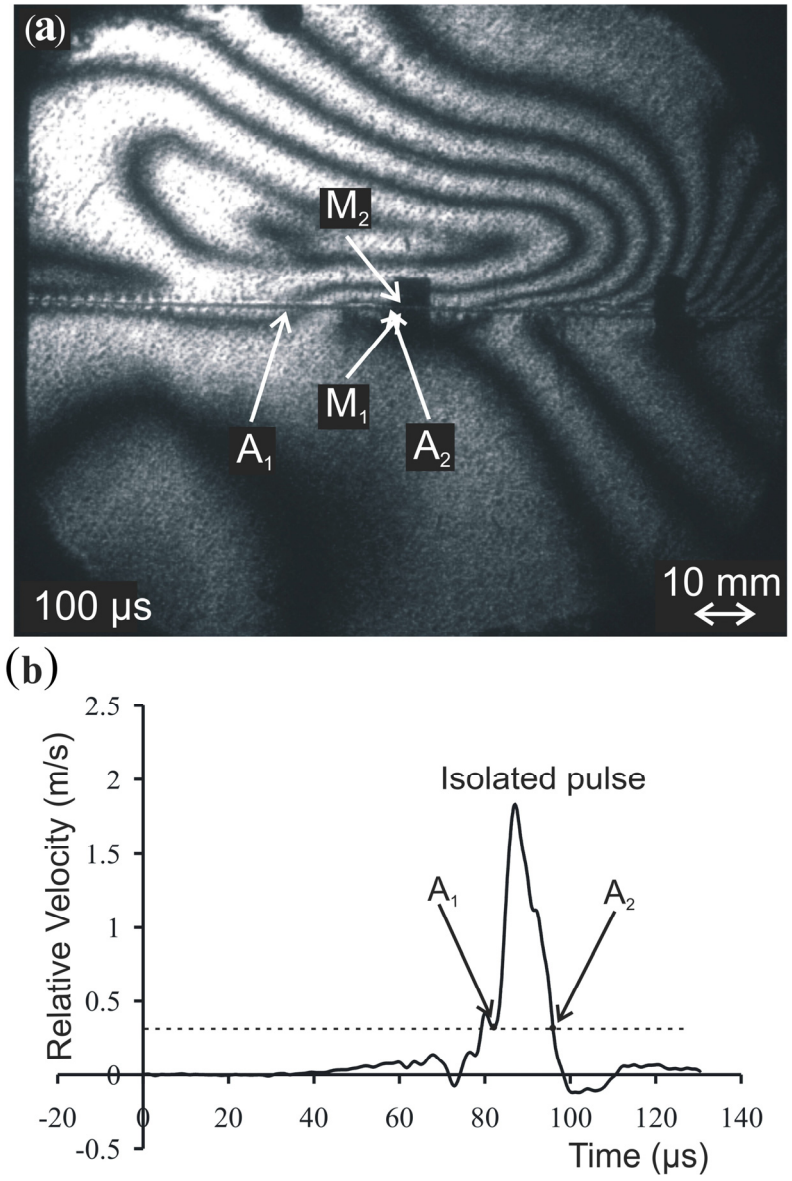

Figure 7 (a) Isochromatic fringe pattern generated during an experiment for which the impact speed was $10\,m/s$ and the external compression was $10\,MPa$. The fringe concentration points A_1 and A_2 are the rupture tip and the rear-edge respectively of the "pulse-like" rupture mode. (b) Relative velocity history of points M_1 and M_2 located at a distance of $70\,mm$ from the impact side of the Homalite plates. The rupture commenced when the rupture tip A_1 reached the velocity measurement position and an isolated pulse A_1A_2 was formed.

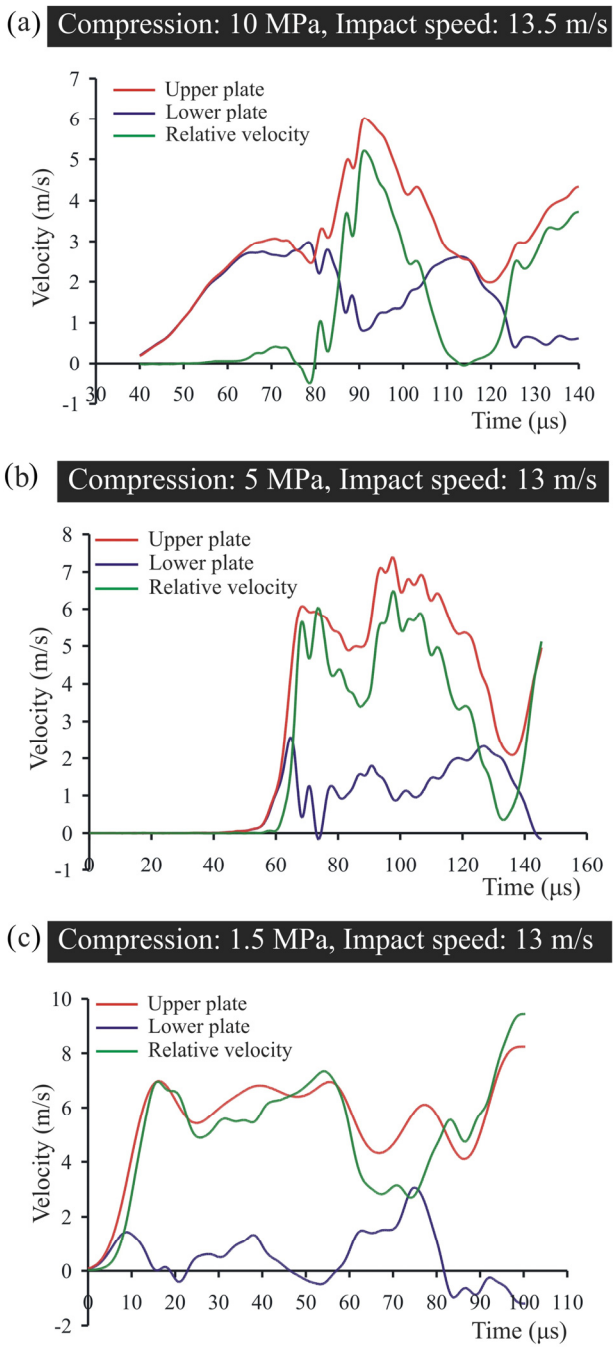

Figure 8 (a) - (c) Horizontal in-plane velocity histories and horizontal in-plane relative velocity histories of points M_1 and M_2 located at a distance of $70\,mm$ from the impact side of the Homalite plate. The impact speeds are essentially the same, on the order of $13\,m/s$ for all three experiments, whereas the external compression decreases.

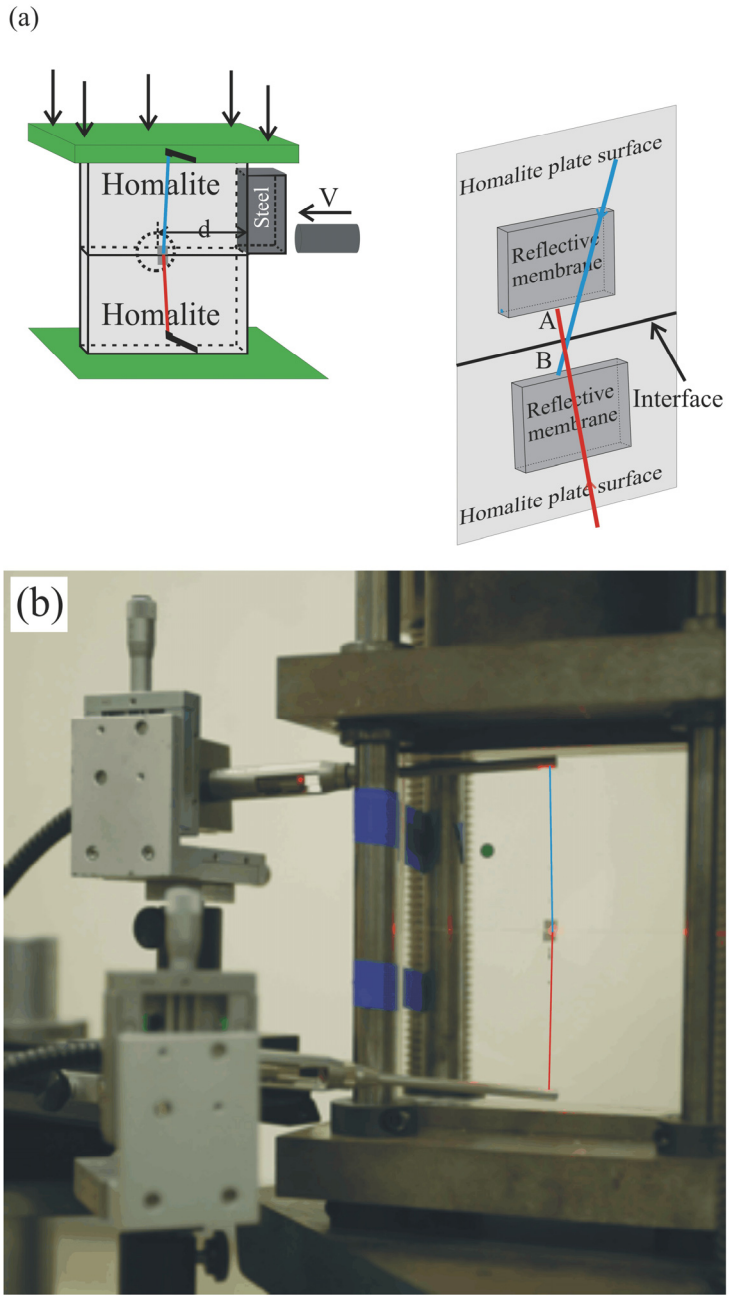

Figure 9 (a) Schematic illustration of the experimental configuration for the relative vertical velocity measurement. The area inside the dotted line is shown magnified. Points M_1 and M_2 are at the same horizontal distance from the impact side of the Homalite plate. (b) Photography of the actual setup displaying the arrangement of the velocimeters' heads.

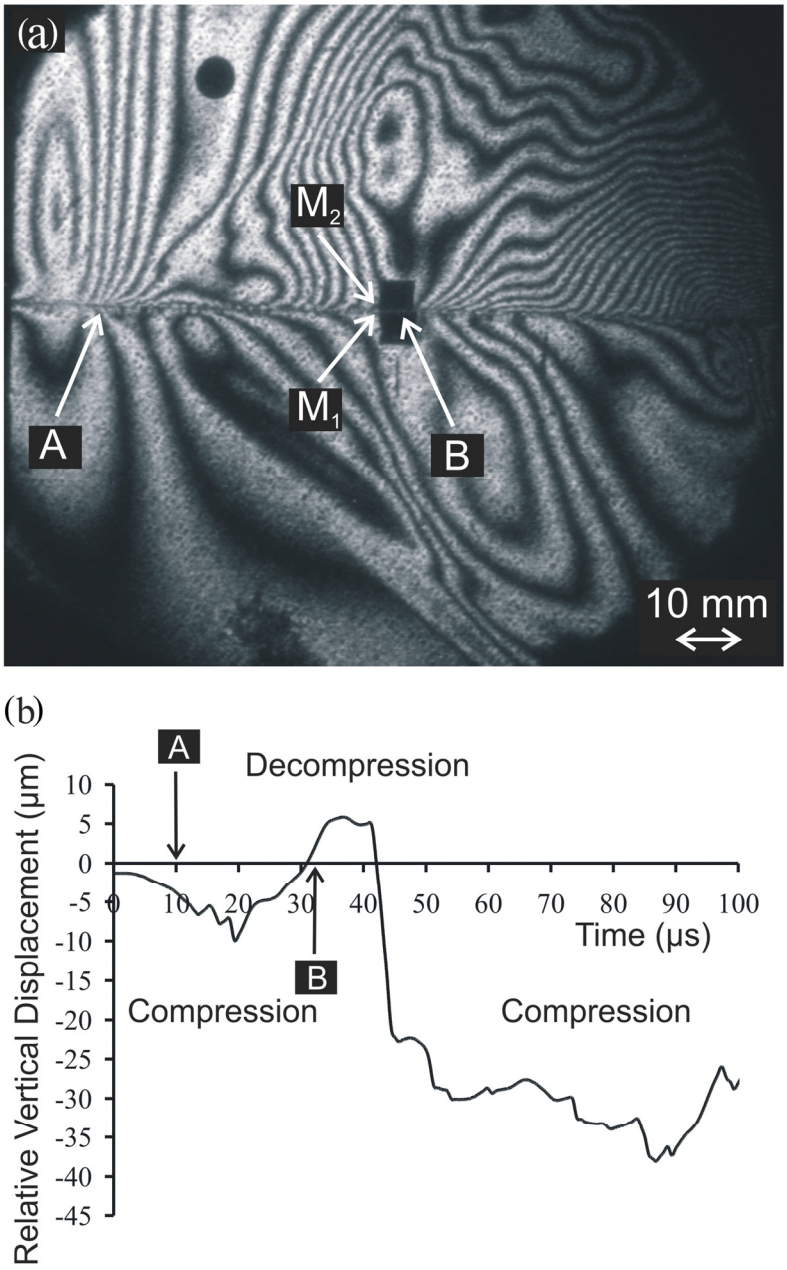

Figure 10 (a) Isochromatic fringe pattern generated during an experiment for which the impact speed was $28 m/s$ and the external compression was $10 MPa$. The rupture tip is at the fringe concentration point A and the wrinkle-like pulse is at point B. (b) Relative vertical displacement history of points M_1 and M_2, located at a distance of $70 mm$ from the impact side of the Homalite plate. The rupture tip and the wrinkle-like disturbance crossed the velocity measurement position at approximately $10 \mu s$ and $32 \mu s$ after triggering, respectively.

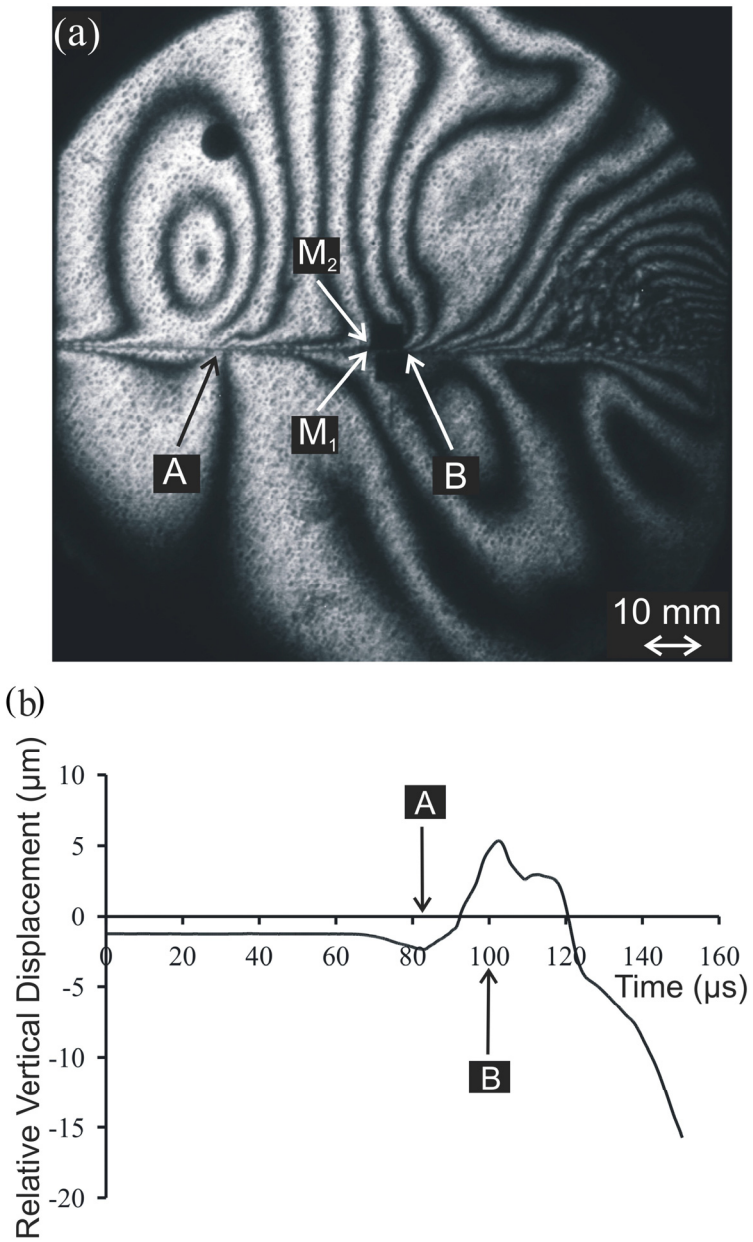

Figure 11 (a) Isochromatic fringe pattern generated during an experiment for which the impact speed was $18\,m/s$ and the external compression was $10\,MPa$. The rupture tip is at the fringe concentration point A and the wrinkle-like pulse is at point B. (b) Relative vertical displacement history of points M_1 and M_2, located at a distance of $70\,mm$ from the impact side of the Homalite plate. The rupture tip and the wrinkle-like disturbance crossed the velocity measurement position at approximately $82\,\mu s$ and $100\,\mu s$ after impact, respectively.

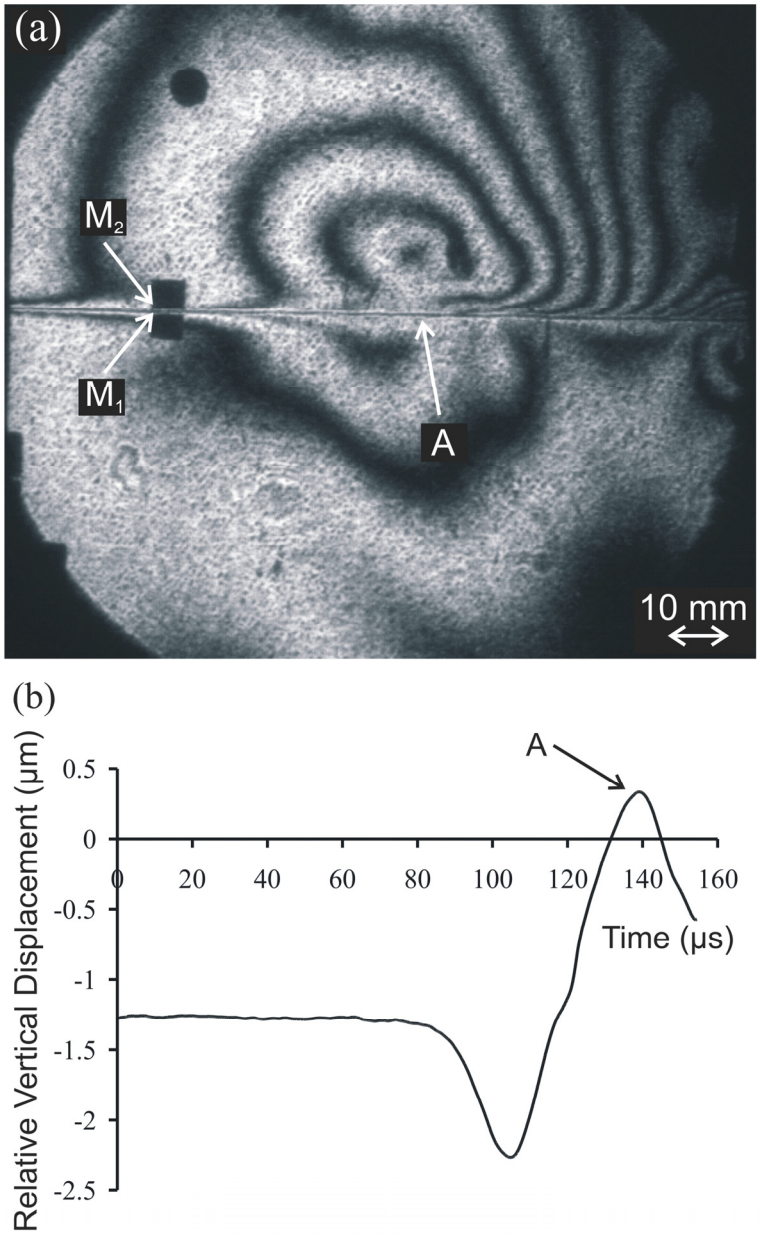

Figure 12 (a) Isochromatic fringe pattern generated during an experiment for which the impact speed was $9 m/s$ and the external compression was $10 MPa$. The rupture tip is at the fringe concentration point A. No wrinkle-like pulse is appeared. (b) Relative vertical displacement history of points M_1 and M_2 located at a distance of $100 mm$ from the impact side of the Homalite plate.

Chapter 5

FRICTIONAL SLIDING ALONG INCOHERENT INTERFACES OF HOMOGENEOUS SYSTEMS INDUCED BY HIGH-SPEED IMPACT SHEAR LOADING

5.1 Introduction

The combined use of classic dynamic photoelasticity with the newly developed technique of velocimetry allowed us to fully characterize the frictional sliding process. Various photoelastic fringe formations were related to physical events like supershear sliding, pulse-like sliding and wrinkle-like pulses. However, the maximum particle velocity which can be measured by the velocimeter is $10 m/s$. In order to comply with the above limit, low impact speeds were used in chapter 4. Here, only dynamic photoelasticity in conjunction with high-speed photography is used as a diagnostic tool. Thus, a wide spectrum of impact speeds is employed for sliding initiation. Experimental results obtained at high impact speeds (on the order of $80 m/s$) are compared to results obtained at low impact speeds (on the order of $10 m/s$).

Besides the impact speed, the static confining stress and the surface roughness are two parameters which also drastically affect the dynamic sliding. In this chapter, results from experiments performed at various static compressive stresses are presented. Three different types of contact surfaces with one order of magnitude difference in roughness between each other are also used.

5.2 Material and Specimen Configuration

The material and specimen configuration employed in this chapter are the same as those in chapter 4. The experimental results were recorded in a microsecond time scale and the initiation and evolution of sliding at high impact speeds were explored. The material used was Homalite-100 and dynamic photoelasticity was employed to extract stress field

information. The isochromatic fringe patterns formed in the Homalite plates were clearly visible at impact speeds higher than $9 m/s$. The longitudinal, shear and Rayleigh wave speeds in Homalite are $C_P = 2583 m/s$, $C_S = 1249 m/s$ and $C_R = 1155 m/s$ respectively. The above values were obtained by ultrasonic measurement, using pressure and shear transducers operating at $5 MHz$, which give the wave speeds in the 3-D bulk material. In the performed experiments, however, the configuration was plane stress, since plate specimens $76.2 mm$ high, $139.7 mm$ long and $9.525 mm$ thick were employed. The plane stress shear wave speeds are identical to the values obtained in the 3-D configuration. The same is true for the Rayleigh wave speed, since the contribution in the Rayleigh wave formation comes primarily from the shear wave. However, the plane stress longitudinal wave speed of Homalite-100 is $C_P^{\sigma} = 2187 m/s$ and it is different from the corresponding 3-D value.

5.3 Experimental Procedure

The experimental procedure was similar to that used by Rosakis, Samudrala and Coker 1999 and by Samudrala and Rosakis 2003 in the investigation of shear crack propagation. The plate specimens were held together by a uniform compressive stress applied by a calibrated hydraulic press (see Figure 1). The asymmetric impact loading was imposed via a cylindrical steel projectile of diameter $25 mm$ and length $51 mm$ fired using a gas gun with impact velocities ranging from $9 m/s$ to $72 m/s$. A steel buffer $73 mm$ high and $25.4 mm$ long was attached to the specimen at the impact site to prevent shattering and to induce a more or less planar loading wave.

Figure 2 shows a typical experimental setup for dynamic photoelasticity experiments. The photoelastic optical setup was arranged for light field. The isochromatic fringes are contours of maximum in-plane shear stress τ_{max} governed by the stress optical law

$$2\tau_{max} = \sigma_1 - \sigma_2 = N\ F_\sigma / h$$

where F_σ is the stress optical coefficient (for Homalite $F_\sigma = 22.6\,KN/m$), h is the specimen thickness, σ_1, σ_2 are the principal stresses and $N = n + 1/2$ (with $n = 0,1,2,...$) is the isochromatic fringe order. A continuous, circular polarized laser beam of $130\,mm$ in diameter was transmitted through the specimen and an analyzer. The resulting isochromatic fringe pattern was recorded by a high-speed digital camera (Cordin model 220), which is able to record 16 distinct frames at framing rates up to 100 million frames per second. In this experimental work, most of the high-speed photography was performed at 250,000 to 1,000,000 frames per second. The field of view was wide enough to cover most of the specimen.

Homalite plates of three different surface roughnesses were utilized. First, the Homalite plates were used as received from the machine shop without undergoing any specific treatment. The average roughness of the surfaces in contact was approximately $R_a = 400\,nm$. The average roughness R_a is simply the average of the absolute values of the surface height variations z_i measured from the mean surface level. Expressed in equation form, this is $R_a = 1 \Big/ N \sum_{i=1}^{N} |z_i|$, where N is the number of equally-

spaced measured points. The mean surface level is defined such that $\sum_{i=1}^{N} z_i = 0$. The measurements were performed by a mechanical stylus surface profiler Tencor Alphastep 200. The polished surfaces were prepared as follows. A Buehler No 70 pad and Lapmaster abrasive 1900 were first employed for 10 minutes. Then a Buehler No 40 pad with diamond compound 3 microns was used for 40 minutes and finally the surfaces were polished by a diamond compound of $1/4$ micron for 10 minutes. The above treatment of the Homalite plate surface resulted to a mirror-like surface with an average roughness of $R_a = 20nm$. In order to prepare the rough surfaces, we started from the polished surfaces and we roughened them by bead blasting with glass beads of (C 40-60, CAS 65997-17-3) for 30 seconds. The above procedure resulted to an average surface roughness of $R_a = 6.3\mu m$. The pictures in Figure 12 were taken by an SEM electronic microscope with magnification 1000 and show representative sections of the three different types of surfaces used in the experiments. It is clear that the morphologies of the three surfaces are very different.

5.4 Photoelastic Stress Field during Dynamic Sliding of a Homalite Plate Subjected to a Constant External Compressive Stress and Different Impact Speeds.

In this section the influence of the impact speed on the sliding process along incoherent interfaces is investigated. Results are described from a number of experiments, performed at the same external confining stress of $10MPa$ and at different impact speeds. The images in Figure 3(a) show the isochromatic fringe patterns at selected times for an impact speed of $32.7m/s$. The images at different times are similar, indicating that the sliding propagation had reached a more or less steady state. In Figure 3(b), our attention is focused on the image (iii) of the Figure 3(a). The loading wave front arrives from the left. The arrow A shows the position of the longitudinal wave front. A relatively broad fringe pattern

(shown just behind point A) having a rib-eye structure emanates from the interface. Since this structure was missing in similar experiments without external pressure (see section 5.5), we can safely conjecture that it was caused by the interference of the loading wave with the preexisting confining static pressure. In addition, it is noted that the eye-like fringe structure was not related to the sliding process, since it developed also in simple impact experiments where the specimens did not have any interface and consequently no sliding was allowed.

The impact loading created a horizontal compressive stress σ_{11} in the upper plate, close to the interface. This was the driving stress for the sliding. Because of the Poisson effect, the horizontal compressive stress induced a dynamic (inertial) vertical compressive stress, which depended on the impact speed. A very simple calculation, based on the theory of 1-D wave propagation in solids, gives that for impact speeds on the order of $40\,m/s$, the maximum dynamic compressive stress is expected to be on the order of $10\,MPa$, which is comparable to the confining static stress we used. The dynamic compressive stress was added to the confining stress and the frictional sliding resistance $\tau = f\,\sigma_{22}$ (where f is the dynamic friction coefficient) increased. Consequently, there was a coupling between σ_{11} and the static friction. The compressive stress σ_{11} generated the shear stress which produced sliding when it overcame the static friction, and at the same time it increased the static friction via the Poisson effect.

The sliding started at point B where the driving shear stress attained its maximum and became equal to the resisting friction. The sliding propagated intersonically behind the loading wave and a shear Mach cone emanating from the rupture point was formed by a sharp change in the fringe density. The insert of Figure 3(b) focuses on the region near the propagating tip and a dotted line is drawn along the Mach discontinuity. The position of the longitudinal wave front was measured in each one of the 16 available frames. As it is shown in Figure 4(a), the positions followed an almost linear pattern which means that the P-wave speed was constant and the longitudinal wave did not exhibit measurable amounts of dispersion within the window of observation of our experiments. A linear interpolation gave a plane stress longitudinal wave speed of $2161 m/s$, which is very close to the value $2187 m/s$ obtained by an ultrasonic measurement as mentioned in the previous section. Using the ultrasonic measurement technique, the glassy properties of Homalite-100 are obtained. The fact that both methods gave essentially the same value for the longitudinal wave speed means that the strain rate during the impact experiment was high and the specimen did not exhibit any viscoelastic behavior. Independent measurements show that the strain rate was on the order of $1000 s^{-1}$.

The propagation speed of sliding was obtained in two different ways and found to be constant. First, we followed the positions of the sliding tip B (see Figure 4(a)) in different frames. The variation is very well approximated as linear and thus we can conclude that the sliding propagation speed was constant. A linear interpolation gave a sliding tip speed of $1868 m/s \cong 1.5 C_S$. Then, by using the relation $\mathrm{v} = \mathrm{c_s}/\sin\theta$, where v is the speed of the

sliding tip and θ is the Mach angle, the sliding tip speed at different frames was obtained (see Figure 4(b)). Again, a constant sliding tip speed within an experimental error is observed. The average value of the sliding tip speed is $1927 m/s \cong 1.54 C_S$. Both methods are found to be in agreement to within 3.1%. The above result was obtained by using the shear wave speed of Homalite measured ultrasonically. Again, the fact that both methods give essentially the same result strengthens the conclusion, drawn from the P-wave propagation speed measurement, that during impact experiments the Homalite specimens do not exhibit viscoelastic behavior.

Some distance behind the sliding tip a fringe structure was formed (point C in Figure 3(b)). This structure was very robust and it was propagated with a speed of $1288 m/s \cong 1.03 C_S$, which is close to the Rayleigh and shear wave speeds of Homalite-100. As we have shown in chapter 4, this fringe structure is related to a wrinkle-like pulse propagating along the interface. Other characteristic features in Figure 3(b) are: (i) a cusp in the stress contours at the interfaces, indicating that the propagation speed is slightly faster along the interface than in the bulk; (ii) the fringe density is higher in the plate where the impact loading was applied, showing that energy is not transferred easily across the interface and (iii) the fringe discontinuity at the interface shows that there is a relative sliding between the two faces behind the rupture point, reflecting the fact that rupture happened in a crack-like mode.

Figure 3(c) displays the variation of the maximum shear stress $\tau_{\max}$ along a horizontal line drawn at a distance of $0.3 cm$ from the interface of the specimen. Assuming that in the

undisturbed area of the isochromatic fringe pattern of Figure 3(b) the stress field was mainly $\sigma_{22} = -10\,MPa$, the expression $\tau_{\max} = \sigma_1 - \sigma_2/2 = N\,F_\sigma/2h$ results in the deviation of the maximum shear stress $\tau_{\max}$ from the static value of $5\,MPa$. The above assumption regarding the static value of the stress σ_{22} has been verified by a static finite element calculation. As the line crossed the eye-like fringe structure, $\tau_{\max}$ initially increased and then decreased to almost the initial value. At the rupture point A, a sharp change in the slope of the diagram of the maximum shear stress occurs. At the Mach line the increase of $\tau_{\max}$ becomes steeper. Along the wrinkle-like pulse, the slope of $\tau_{\max}$ diagram decreases and becomes almost constant as the impact area is approached. Very close to the edge $\tau_{\max}$ increases, since the corner of the specimen is approached.

Finally, an important comment on the frictional sliding experiment discussed above is that the sliding tip speed and the wrinkle-like pulse speed were constant during the entire observation time. That is a general result and it holds true for all the experiments performed. The sliding tip speed, the wrinkle-like pulse speed and the speeds of all the other disturbances or singularities, which are identified in the rest of the paper propagating along the interface, were always constant. This is a strong characteristic of frictional sliding and it agrees with theoretical results (Adams 1998; Rice, Lapusta and Ranjith 2001; Ranjith and Rice 2001) which predict constant discrete propagation speeds for all the different disturbances and singularities along the interface.

In Figure 5, isochromatic fringe patterns are shown at three different times for the same compressive load of $10MPa$ as in the previous experiment and at a higher impact speed of $42.2\,m/s$. The sliding propagated intersonically at approximately $1948m/s = 1.56C_S$. Although the general characteristics we encountered at the slower impact speed were still preserved, new features enriched the picture. Behind the loading wave a shear Mach cone was formed. In addition, a second Mach line which was non-parallel to the first one was observed behind the rupture point (Figure 5(a)). The Mach line was at a shallower slope corresponding to a supershear (approximately sonic) propagation speed of $2514\,m/s = 2.01C_S = 0.97\,C_P$. Non-parallel shock lines imply a highly transient and unstable contact process. Indeed, in Figure 5(b) the tip of the second Mach line approached the end of the first Mach line. Finally, these two points merged as the second point caught up with the first point (see Figure 5(c)). The sliding continued at the lower speed and thus only one Mach line is observed in the next recorded frames. More detailed views of the rupture process are shown in the inserts of Figures 5(a) and (b). The dual and single shock waves structures are highlighted by dotted lines. The existence of two Mach lines means that there was onset of sliding at two different points and thus we can conjecture that the initial sliding which started at point B_1 stopped after a while and new sliding started at point B_2. In this way, an unstable sliding pulse was formed between the points B_1 and B_2 followed by a crack-like sliding which started at point B_2. Behind the second Mach line, the wrinkle-like pulse appeared at point C. It propagated with a speed of $0.92C_S$, close to the Rayleigh wave speed of Homalite. Figure 5(c) shows the position histories of the first and second sliding tips and the wrinkle-like pulse for the case above. It is evident that the

second sliding tip moved faster than the first sliding tip and at approximately $50\mu s$ the pair of points coalesced.

Figure 6 shows an instantaneous isochromatic fringe pattern caused by an impact speed of $60 m/s$, at a confining stress of $10 MPa$. Rupture tip B was traveling at a speed of $1.64 C_S$ and a Mach cone was formed. The fringe structure related to a wrinkle-like pulse appears at C. Its propagation speed was $1.01 C_S$. Unlike in the case of Figure 5, we were not able to capture any transition from double shock to single shock. A reason would be that the transition happened in the very first few microseconds, when the fringe density was too high and the Mach lines were not visible. It is noted that all the experiments performed at a confining stress of $10 MPa$ and at very high impact speeds (higher than $40 m/s$) generated essentially similar stress distributions. As we have seen in chapter 4, however, the situation changes dramatically at low impact speeds.

Figure 7 shows very vividly the change in the photoelastic images as the impact speed decreased. Figure 7(a) depicts the photoelastic field at $40\mu s$ after impact. The impact speed was $24.3 m/s$, while the static pressure was kept constant at $10 MPa$. The sliding tip traveled at a supershear speed of $1813 m/s = 1.45 C_S$ and a Mach cone emerged from it. The wrinkle-like pulse formed and propagated at $1228 m/s \cong 0.98 C_S$. Lower impact speeds result in lower dynamic stresses and therefore a lower fringe pattern density is developed than arises at higher impact speeds. Up to this point, the presented isochromatic fringe patterns had a more or less similar structure. The photoelastic stress field developed in the

case of $13 m/s$ impact speed is different, however, as is clearly shown in Figure 7(b). Two fringe concentration points B_1 and B_2 are observed. The sliding started at point B_1, the end of the eye-like fringe pattern. However at B_2, there was another fringe concentration point which was a second sliding tip. Following B_1 and B_2 at different frames we found that they traveled at constant speeds of $1427 m/s \cong 1.14 C_S$ and $1347 m/s = 1.08 C_S$ respectively. Based on similar results in chapter 4, where sliding velocity measurements were available, we conjecture that the section B_1B_2 was a self-sustained pulse which propagated at a supershear speed. At point B_2 a crack-like sliding started, since an almost uniform fringe discontinuity along the interface was formed. The Mach cones are not so prominent because the fringe density is low, and the fringe discontinuity along the Mach lines was not well formed. However, the two Mach lines can definitely be traced if the kinks of the fringes in the upper plate were to be connected.

In the last part of this section, the influence of the impact speed on the propagation speeds of the sliding tip and of the wrinkle-like pulse is explored. Figure 8(a) shows the variation of the sliding propagation speed with the impact speed at a constant uniform confining stress of $10 MPa$. The slowest impact speed we were able to achieve using the gas gun was $9 m/s$. In this case and in other cases with impact speeds close to $10 m/s$ the sliding tip speed was sub-Rayleigh. At impact speeds higher than $11 m/s$ the sliding edge speed became supershear. We observed that for impact speeds in the range of $20 m/s$ to $40 m/s$, the sliding speed was close to $\sqrt{2}\, c_S$. This is a special rupture speed and it has been shown that it separates regions of unstable and stable intersonic shear crack growth (Samudrala,

Huang and Rosakis, 2002a and 2002b). When the impact speed increased, the sliding tip speed increased toward the plane stress P-wave speed. It is worth mentioning that no sliding speed was observed in the interval between the Rayleigh wave speed and the shear wave speed of Homalite-100. This experimental observation agrees with theoretical works on steady-state shear crack propagation which exclude this speed interval based on energetic arguments (Freund, 1990; Broberg, 1999). We also note that the performed experimental sliding tip speed measurements feature high-enough resolution to obtain propagation speeds in the interval between C_R and C_S, if such speeds existed. This is proven by the fact that almost all the recorded speeds of the wrinkle-like pulses were in this speed interval.

The propagation speeds of wrinkle-like pulses at different impact speeds and at the same confining stress of $10\,MPa$ are shown in Figure 8(b). The sliding speed was, within an experimental error, always between the Rayleigh wave and the shear wave speed of Homalite-100. This result, in combination with the experimental results regarding the relative vertical displacement obtained in chapter 4, favors our conjecture that the interface disturbance was actually a wrinkle-like pulse. As has been already mentioned, the theoretical and numerical analysis on the subject predicts the same wave speed limits with those identified in Figure 8(b).

We finally note that experiments performed at lower compression show that the speed of the wrinkle-like pulse is not affected by the change in the static confining stress. The

rupture speed, however, is affected and it was supershear even at the lowest achieved impact speed.

5.5 Frictional Sliding Without Confining Pressure

Experiments at different impact speeds and without external stress applied are presented in this section. Using the above configuration, we were able to observe only the effect of impact loading on the sliding process. Figure 9(a) shows an instantaneous photoelastic fringe pattern at $92\mu s$ after impact. The projectile speed was $13 m/s$. The fringes at the wave front are almost vertical to the interface, showing that a shear loading was almost obtained. At point C, a fringe structure characteristic of a wrinkle-like pulse is present. We also note that the eye-like fringe pattern was not formed. This proves that the eye-like fringe structure is indeed generated by the interaction between the loading wave and the static confining stress. Regarding sliding, we conjecture that it started almost immediately after the P-wave front. However, we cannot identify any sliding tip, since the fringe density is very small.

Another characteristic of the fringe pattern is that the fringes on the left of the wrinkle-like pulse were slightly bent toward the interface. This is more pronounced in Figure 9(b) where the impact speed was $24 m/s$. The fringes bent toward point B and a fringe concentration point was about to be formed. The wrinkle-like fringe structure was at C and traveled at $1126 m/s \cong 0.9 C_S$.We also note that the first three fringes on the left of point B are slightly inclined but they do not clearly form a Mach cone. At higher impact speeds the fringe density was higher and the different features of the fringe pattern are visible. In Figure 9(c),

the isochromatic fringes are shown for an impact speed of $40\,m/s$ and at $64\,\mu s$ after impact. The wrinkle-like structure is better defined than in the case of $24\,m/s$ impact speed. Point C traveled along the interface at a speed of $1065\,m/s \cong 0.85\,C_S$. The fringes on the left of the wrinkle-like pulse were bent and a Mach zone was clearly emanating from the section B_2B_3. This Mach zone has an internal structure and it shows that a disturbance on the interface traveled at a supershear speed of $2118\,m/s \cong 1.7\,C_S = 0.82\,C_P$. Also the inclination of the fringes on the left of point B_2 is visible and a zone B_1B_2 has been formed. From the inclination angle we computed the sliding zone speed as $1830\,m/s = 1.46\,C_S = 0.71\,C_P$. Based on the fringe pattern, we can argue that sliding started at point B_1 and the whole zone B_1B_2 propagated along the interface. We also note that the stress field in the lower plate was very low in front of point B_2. This means that the lower plate did not interact with the upper plate and the interface did not exhibit considerable friction, which would have created, by the principle of action reaction, a significant shear stress field in the lower plate. It is obvious, however, in Figure 9(c) that at point B_2, the stress field in the upper plate was disturbed and a significant stress field developed in the lower plate. It is reasonable to argue that the horizontal compressive stress in the upper plate increased to the right of the P-wave front on the side of impact. Because of the Poisson effect, this caused an increase in the vertical dynamic (inertial) compressive stress. Higher vertical compressive stress resulted in higher friction, which created the field in the lower plate. According to the above argument, B_2B_3 was acting like a shear loading zone which was propagated along the interface with a supershear speed. A Mach zone emerging from the area B_2B_3 is clearly visible in Figure (9). B_2B_3 is similar to a cohesive

zone developing during shear crack propagation along glued (coherent) interfaces (Samudrala, Huang and Rosakis, 2002a and 2002b).

Figure 9(d) shows the photoelastic fringe pattern at $74\mu s$ after impact from a projectile at a high speed of $72.4 m/s$. The wave front is at A, whereas the bent fringes form a very narrow cohesive-type zone (B_2B_3). A Mach cone clearly emanates from the zone B_2B_3 at the interface and shows that a disturbance traveled along the interface with a supershear speed. The speed has been measured by means of the Mach angle and by following the positions of B_2 at different frames. The two measurements give $1943 m/s \cong 1.55 C_S$ and $1835 m/s \cong 1.47 C_S$, which are very close (within a 5% experimental error). The narrow zone was detached from the wrinkle-like structure, appearing at point C of the interface (see Figure 9(d)). This separation verifies our conjecture that the creation of a cohesive type zone B_2B_3 is independent of the wrinkle-like pulse and it is instead related to the sliding procedure. Based again on the isochromatic fringe pattern we can argue that sliding started at point B_1.

It is clear from this investigation that the main features of the stress field (with the exception of the eye-like fringe pattern, which is associated to the loading wave) were governed by the impact speed.

5.6 Influence of External Pressure on the Sliding Process

In order to investigate the influence of external pressure on sliding, three cases with very different external applied pressures and similar impact speeds (within the range of $45 m/s$ to $51 m/s$) are compared. In Figure 10(a) the initial pressure was $20 MPa$ and the impact speed was $45.5 m/s$. We observed a complex sliding procedure (similar to the case of Figure 5, discussed extensively in section 5.3). The sliding tip speed was $1859 m/s \cong 1.49 C_S$. A second sliding edge, which existed in the previous frames, is not shown in this picture since it already merged with the sliding edge. Comparing Figure 10(a) with Figure 5(c), we first observe that the eye-like structure at the higher external stress had more fringes, and the compression zone AB was wider than in the case of $10 MPa$ confining pressure. The sliding occurred behind the sliding tip in the section BC, which was smaller than the corresponding segment BC in Figure 5(c). This means that the sliding area was larger in the case of lower external pressure for the same impact speed. At $5 MPa$ confining external pressure (see Figure 10(b)), the loading structure had fewer fringes and the loading wave zone AB was decreased. The fringe structure was simpler than the fringe structure at higher confining pressures and there was not a second sliding edge. The sliding tip speed was $1.62 C_S$.

At a very low external pressure of $1.5 MPa$ (Figure 10(c)), the eye-like fringe structure was not formed. The photoelastic fringe pattern was similar to the fringe pattern developed in the case discussed extensively in section 5, where no external pressure was applied. From the discontinuity of the fringe pattern on the interface we can conclude that at $5 MPa$ and

$1.5\,MPa$ external pressure there is an extended sliding area behind the rupture point (the whole section BC is a sliding zone) which shows that the rupture mode is crack-like. These sliding zones were larger than the corresponding zones developed in the cases with higher external compressive loads. We also mention that the wrinkle-like pulse was present in all cases since the impact speeds were high enough. Finally, it is noted that the sliding tip speed did not depend on the confining stress.

The results derived by an intermediate impact speed on the order of $20\,m/s$ were similar to the results of the high impact speeds discussed above. Because of this similarity, we will not present this case. Instead we will proceed with the case of the low impact speed of $13\,m/s$ (see Figure 11). In this speed range, sliding exhibits some very interesting properties.

At $10\,MPa$ external pressure (Figure 11(a)), two fringe concentration points B_1 and B_2 are observed. In this case a supershear sliding pulse was generated ahead of a crack. Another significant result is that the wrinkle-like pulse was not generated because the impact loading was too small and the wrinkle-like pulse could not overcome the confining pressure. In Figure 11(b), the confining pressure was $5\,MPa$ and the wrinkle-like pulse was formed; it is visible at point C. In this case the sliding tip B traveled at supershear speed of $1872\,m/s \cong 1.5\,C_S$ and the Mach cone is clearly visible. For an even smaller external pressure of $1.5\,MPa$, the wrinkle-like pulse was more prominent, whereas the supershear sliding tip B speed was $1655\,m/s \cong 1.32\,C_S$ (see Figure 11(c)).

In this section, the influence of the external confining pressure on the sliding process was discussed. Many features the stress field developed during sliding were greatly affected by the static pressure (e.g., eye-like fringe structure, length of sliding section, sliding modes). We note, however, that the sliding tip speed was not dependent on the confining pressure but only on the projectile speed. Higher projectile speed resulted in higher sliding tip speed. The speed of the wrinkle-like pulse was not dependent on the confining pressure or on the projectile speed; it was always in the theoretically defined speed range (C_R, C_S).

5.7 Effect of the Surface Roughness on Dynamic Sliding

The surfaces of the Homalite plates employed in the experiments up to this point had not undergone any special treatment. The average roughness was approximately $R_a = 400\,nm$. In this section, the effect of surface roughness on the sliding process and especially on the initiation of sliding is investigated. First, experimental results from dynamic sliding of polished surfaces are displayed and they are compared to corresponding results from the sliding of untreated surfaces. In the second part, the dynamic sliding of roughened surfaces is investigated. The average roughness of the polished surfaces was approximately $R_a = 20\,nm$, one order of magnitude lower than the roughness of the untreated surfaces. The roughened surfaces featured an average roughness of approximately $R_a = 6.3\,\mu m$, one order of magnitude higher than the roughness of the untreated surfaces. Samples of the three different surfaces magnified by an electronic microscope are displayed in Figure 12. From the pictures it is obvious that the morphologies of the surfaces are different.

5.7.1 Dynamic Sliding of Polished Surfaces

Instantaneous isochromatic fringe patterns captured at specific times during experiments which involved Homalite plates with polished and untreated surfaces are shown in Figures 13(a) and (b) respectively. The uniform confining stress ($10\,MPa$) and the impact speed ($19\,m/s$) were the same for both cases. The images feature similar structures. Sliding started at point B behind an eye-like fringe structure propagating from right to left. The rupture tips speeds were in both cases supershear and similar ($1.3\,C_S$ in the case of polished surfaces and $1.36\,C_S$ in the case of untreated surfaces). The fringe structure related to wrinkle-like pulses also appears. Its propagation speed was approximately $1.03\,C_S$ in the case of the polished surfaces and C_S in the case of the unpolished surfaces. Again the speeds were essentially the same within an experimental error.

The general features of the two photoelastic pictures and the extracted propagation speeds of the rupture tips and the wrinkle-like pulses are very similar for both polished and unpolished contact surfaces. There is, however, a significant difference in the fringe patterns around the rupture tip, which means that the rupture initiation process was different in the two cases. In Figure 13(b), the rupture tip B is almost under the center of the eye-like fringe structure and the fringes are stretched around B. In Figure 13(a), the rupture tip B is further away from the center of the eye-like fringe structure and the fringes on the left of B are continuous from the upper plate to the lower plate. This means that the maximum value of dynamic friction was higher in the case of the polished surfaces than in

the case of the unpolished surfaces. Figure 14 presents photoelastic pictures captured in four experiments with polished surfaces performed at the same external pressure of $10\,MPa$ and at different impact speeds. Using our experience, acquired by velocimetry, we conjecture that the rupture tip in Figure 14(a) is at point B. The impact speed was low ($6.2\,m/s$) and the sliding tip was traveling at a subshear speed of $0.94\,C_S$. As the impact speed increased at $14\,m/s$, the rupture became supershear with a propagation speed of $1.3\,C_S$. Two Mach lines emanate from rupture tip B, which is located far from the center of the eye-like fringe structure (Figure 14(b)). As the impact speed increased to $21\,m/s$ (Figure 14(c)) and to $49\,m/s$ (Figure 14(d)), the sliding tip speed also increased to $1.37\,C_S$ and to $1.56\,C_S$ respectively. By comparing those speeds to the corresponding sliding tip speeds developed in experiments with unpolished surfaces, it can be concluded that the surface roughness does not affect the resulting rupture tip speed. The same conclusion holds true also for the wrinkle-like pulse speeds. In addition, it is observed that the sliding tip distance from the center of the eye-like structure decreased as the impact speed increased. This means that the process of sliding initiation occurred more abruptly as the impact speed increased.

5.7.2 Dynamic Sliding of Roughened Surfaces

Figure 15 displays the photoelastic images captured during dynamic sliding of roughened surfaces. The compression was $10\,MPa$ and the impact speeds were $22\,m/s$ and $40\,m/s$. In both cases the rupture was supershear. In the first experiments the speed of the rupture tip and of the wrinkle-like wave were approximately $1.30\,C_S$ and $0.9\,C_S$. The rupture tip

speed in the second experiment was $1.52C_S$ and the speed of the wrinkle-like pulse was approximately $0.99C_S$. The configurations of the isochromatic fringe patterns are very similar to the fringe patterns developed in previous experiments which involved untreated surfaces. We thus conclude that increase of roughness from $Ra = 400nm$ to $Ra = 6.3\mu m$ does not greatly affect the sliding process at a compression of $10MPa$ and with impact speeds between $22m/s$ and $40m/s$.

5.8 Conclusions

The evolution of dynamic frictional sliding along incoherent interfaces of two identical Homalite plates, held together by compressive stress and subjected to impact shear loading, was experimentally investigated. The case of freely standing plates with no external pressure was also studied. The stress fields developed during the events were recorded in a micro-second time scale by high-speed photography used in conjunction with classical dynamic photoelasticity. By modifying the experimental parameters of impact speed and superimposed quasi-static pressure the following significant effects were captured:

- The interaction between the impact wave and the preexisting static stress field caused a relatively broad loading wave that emanated from the interface.
- As the projectile speed decreased under a certain value, the sliding transitioned from pure crack-like to a slip pulse followed by a crack.
- The observed propagation speeds of the sliding tips were not dependent on the confining pressure but only on the projectile speed. The speeds spanned almost the whole interval from sub-Rayleigh to nearly the P-wave speed of the material, with the

exception of a forbidden gap between the Rayleigh wave speed and the shear wave speed.

- Sub-Rayleigh and intersonically propagating pulses were discovered and recorded.
- Mach lines with different inclinations emanating from the sliding zone tips were observed.
- Unlike classic shear cracks in coherent interfaces of finite strength, sliding areas in frictional interfaces seem to grow without noticeable acceleration phases and at various discrete speeds.
- Behind the sliding tip, wrinkle-like pulses that traveled always (independently of the impact speed or the confining stress) at speeds between the Rayleigh wave speed and the shear wave speed of the material were identified.
- There was a cusp in the stress contours at the interface, indicating that the propagation speed was slightly faster along the interface than in the bulk.
- The surface roughness does not affect the propagation speeds of the rupture tip or the propagation speed of the wrinkle-like pulse. It affects, however, the rupture initiation process.

REFERENCES

Adams, G. Steady sliding of two elastic half-spaces with friction reduction due to interface stick-slip. *ASME J. Appl. Mech.* **65**, 470-475 (1998).

Broberg, K.B. *Cracks and fracture*. (Academic Press, London, 1999).

Freund, L. B. *Dynamic fracture mechanics*. (Cambridge University Press, Cambridge, UK, 1990).

Ranjith, K. & Rice, J. R. Slip dynamics at an interface between dissimilar materials, *J. Mech. Phys. Solids* **49**, 341-361 (2001).

Rice, J. R., Lapusta, N. & Ranjith, K. Rate and state dependent friction and the stability of sliding between elastically deformable solids. *J. Mech. Phys. Solids* **49**, 1865-1898 (2001).

Rosakis, A. J. Intersonic shear cracks and fault ruptures. *Advances in Physics* **51**, No. 4, 1189-1257 (2002).

Rosakis, A. J., Samudrala, O. & Coker, D. Cracks faster than the shear wave speed. *Science* **284**, 1337-1340 (1999).

Samudrala, O., Huang, Y. and Rosakis, A. J. Subsonic and intersonic mode II crack propagation with a rate-dependent cohesive zone. *J. Mech. Phys. Solids* **50**, 1231-1268 (2002a).

Samudrala, O., Huang, Y. & Rosakis, A. J. Subsonic and intersonic shear rupture of weak planes with a velocity weakening cohesive zone. *J. Geophys. Res.* **107**, No B8, 10129/2001JB000460 (2002b).

Samudrala, O. and Rosakis, A. J. Effect of loading and geometry on the subsonic/intersonic transition of a bimaterial interface crack. *Eng. Fract. Mech.* **70**, 309-337 (2003).

List of Figures

Figure 1 Geometry and loading configuration for a specimen consisting of two identical incoherent Homalite plates.

Figure 2 Experimental setup. A circular polarized laser beam passes through the specimen which is subjected to impact shear loading via a projectile fired by a gas gun. The resulting isochromatic fringe patterns are recorded by a high-speed digital camera.

Figure 3 (a) Isochromatic fringes of intersonic sliding propagation at different time instances. (b) The P-wave front (A), the sliding tip (B) and the wrinkle-like pulse (C) are shown clearly in the magnification of the fringe pattern (iii). (c) Variation of maximum shear stress along a line at $0.3cm$ distance from the interface.

Figure 4 (a) Positions of the longitudinal wave front, the sliding tip and the wrinkle-like pulse as a function of time. (b) Sliding tip speeds at different frames measured using the Mach angle.

Figure 5 (a-c) Isochromatic fringes of sliding propagation at different time instances. Two sliding tips (B_1 and B_2) were propagating at different intersonic speeds. In the inserts the dual and single Mach lines are marked. (d) Positions of the

sliding leading edge, the second sliding tip and the wrinkle-like pulse as a function of time.

Figure 6 Isochromatic fringes of sliding propagation. The arrows B and C indicate the positions of the rupture tip and of the wrinkle-like pulse respectively. The arrows B and C indicate the positions of the rupture tip and of the wrinkle-like pulse respectively.

Figure 7 Representative isochromatic fringe patterns from four different experiments of sliding propagation initiated by different impact speeds. The specimens were subjected to the same confining stress. The arrows B and C indicate the positions of the rupture tip and of the wrinkle-like pulse respectively. The arrow B_1 indicates the position of the sliding tip, whereas the arrow B_2 shows the position of a fringe concentration point which corresponds to velocity discontinuity.

Figure 8 (a) Variation of the sliding tip speed with the impact speed. The confining stress was $10\,MPa$. (b) The wrinkle-like pulse speed remained between the Rayleigh wave speed and the shear wave speed of Homalite-100, independent of the impact speed.

Figure 9 Representative isochromatic fringe patterns from four different experiments of sliding propagation initiated by different impact speeds. No confining stress was

applied. The arrows B and C indicate the positions of the rupture tip and of the wrinkle-like pulse respectively. The arrow B_1 indicates the position of the sliding tip, whereas the arrows B_2 and B_3 show the position of fringe concentration points which correspond to velocity discontinuities.

Figure 10 Representative isochromatic fringe patterns from three different experiments of sliding propagation initiated by similar high impact speeds; the specimen was subjected to different confining stresses. Arrows A, B and C show the positions of the P-wave front, of the sliding tip and of the wrinkle-like pulse respectively.

Figure 11 Representative isochromatic fringe patterns from three different experiments of sliding propagation initiated by the same low impact speed; the specimen was subjected to different confining stresses. Arrows B and C show the positions of the sliding tip and of the wrinkle-like pulse respectively. Arrows B_1 and B_2 indicate the position of the sliding tips.

Figure 12 Picture showing sections of unpolished, polished and roughened Homalite surfaces taken via a SEM electronic microscope at a magnification 1000. The surfaces B and C have been carbon coated.

Figure 13 Representative isochromatic fringe patterns developed in two different experiments of dynamic sliding, initiated by the same impact speed. In both cases the specimen were subjected to the same static uniform pressure. (a) The

surfaces in contact were polished. (b) The surfaces in contact were unpolished. Arrows B and C indicate the sliding tip and the wrinkle-like pulse respectively.

Figure 14 Representative isochromatic fringe patterns developed in four different experiments of dynamic sliding, initiated by different impact speed. In all cases the specimen were subjected to the same uniform confining stress. The surfaces in contact were polished.

Figure 15 Representative isochromatic fringe patterns developed in two different experiments of dynamic sliding, initiated by different impact speeds. In both cases the specimen were subjected to the same uniform confining stress. The surfaces in contact were roughened.

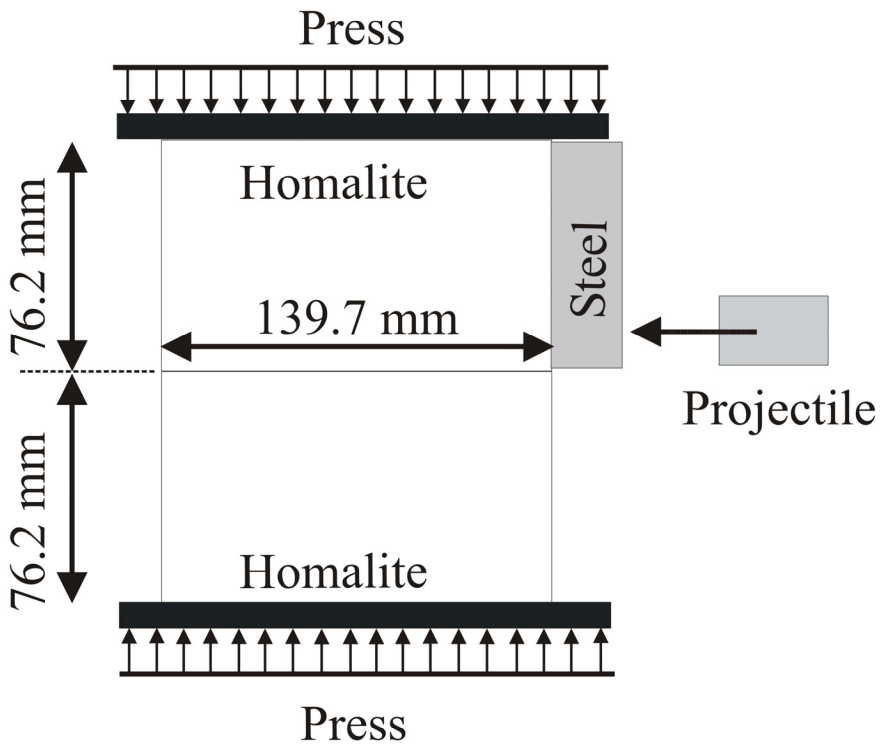

Figure 1 Geometry and loading configuration for a specimen consisting of two identical incoherent plates.

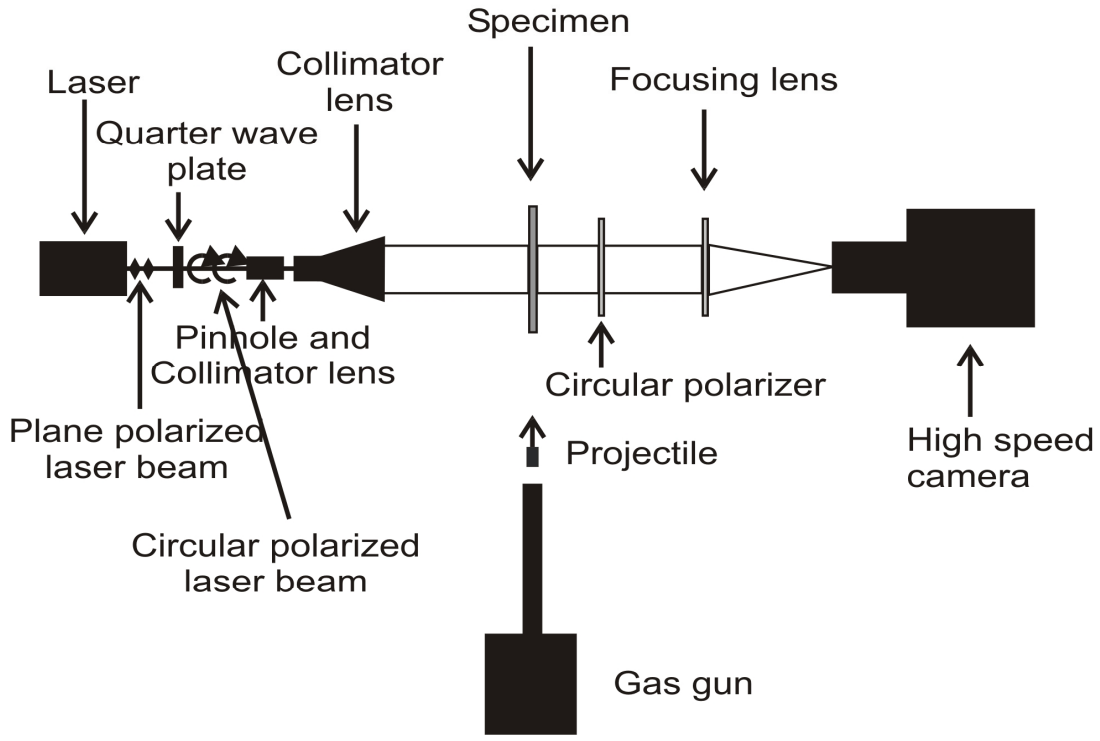

Figure 2 Experimental setup. A circular polarized laser beam passes through the specimen which is subjected to impact shear loading via a projectile fired by a gas gun. The resulting isochromatic fringe patterns are recorded by a high-speed digital camera.

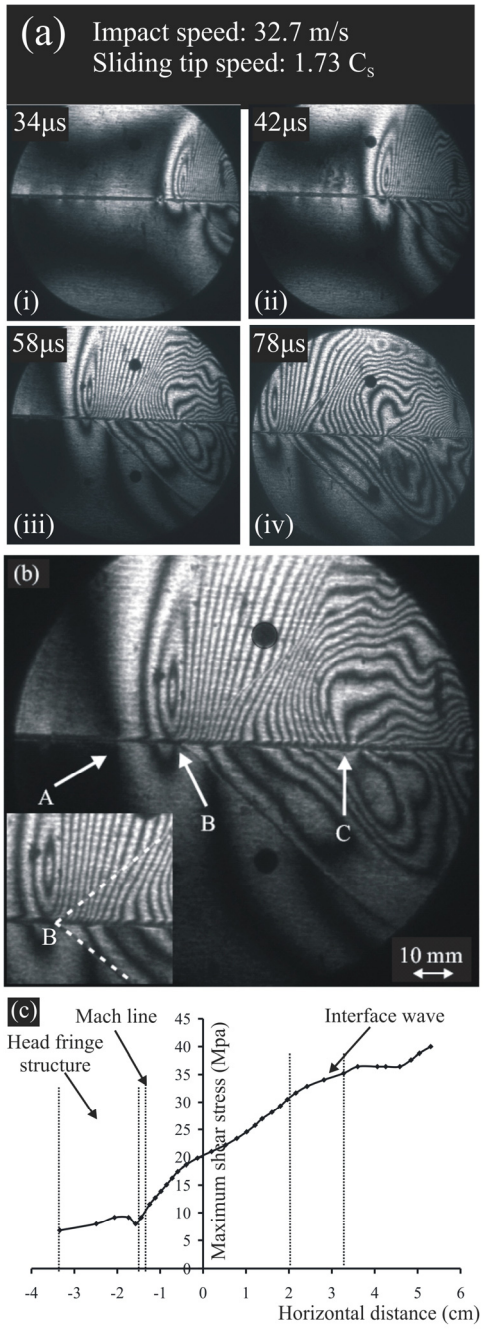

Figure 3 (a) Isochromatic fringes of intersonic sliding propagation at different time instances. (b) The P-wave front (A), the sliding tip (B) and the wrinkle-like pulse (C) are shown clearly in the magnification of the fringe pattern (iii) (c) Variation of maximum shear stress along a line at $0.3cm$ distance from the interface.

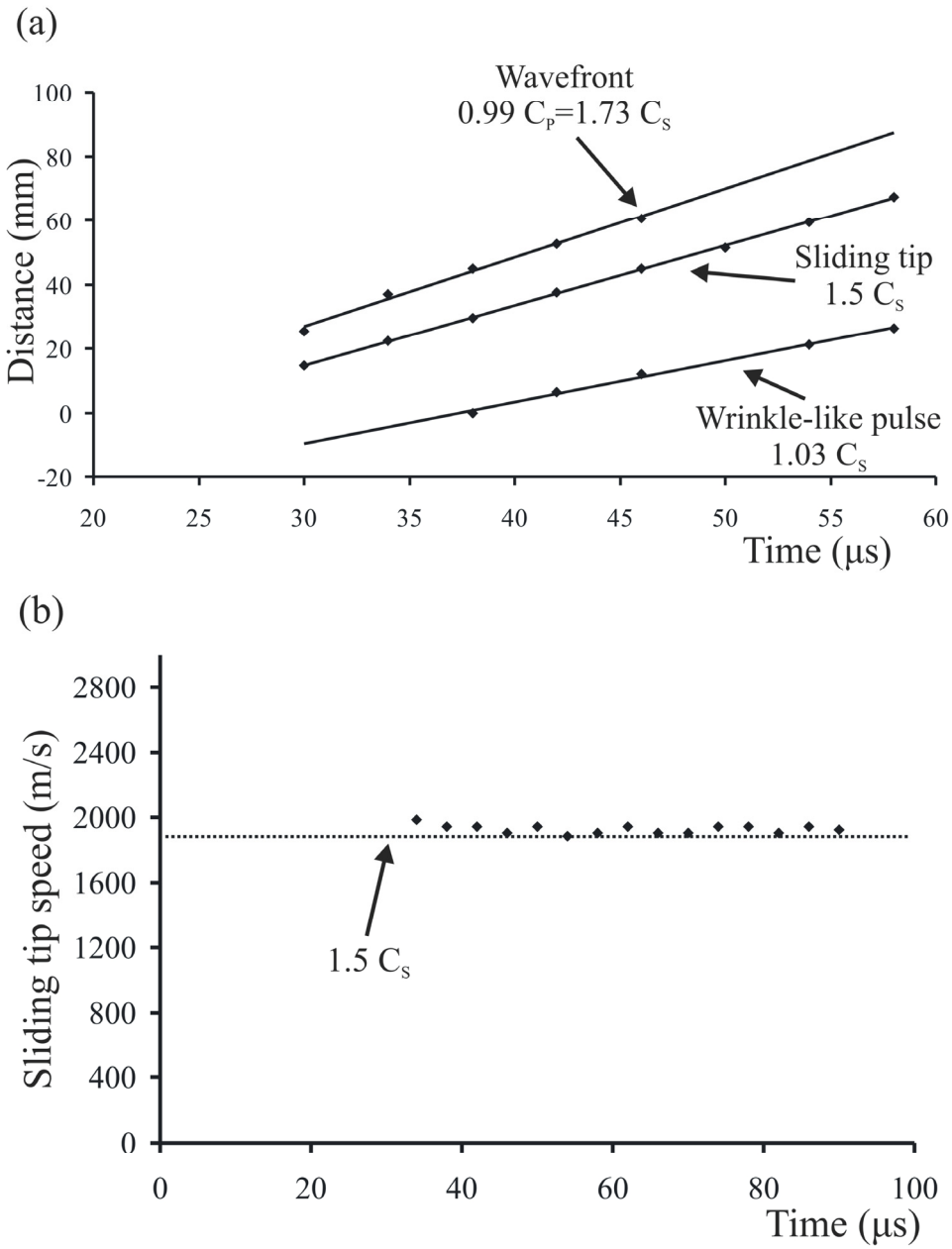

Figure 4 (a) Positions of the longitudinal wave front, the sliding tip and the wrinkle-like pulse as a function of time. (b) Sliding tip speeds at different frames measured using the Mach angle.

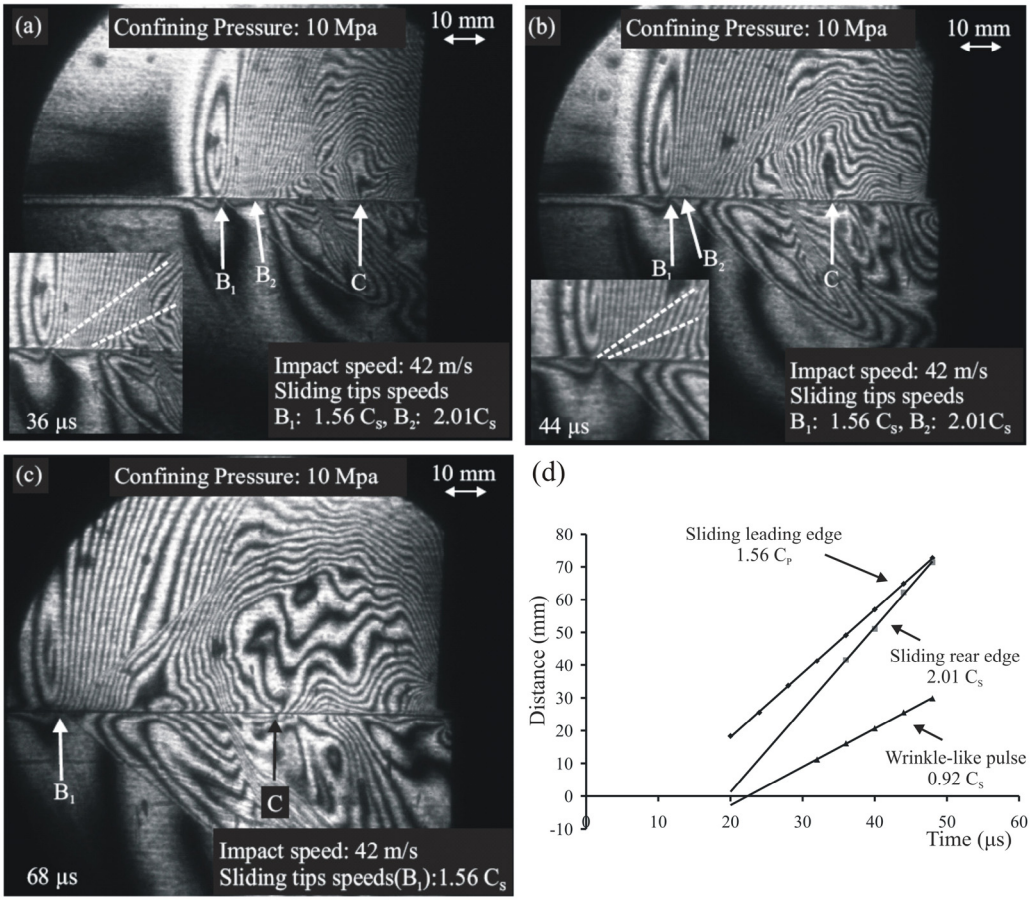

Figure 5 (a-c) Isochromatic fringes of sliding propagation at different time instances. Two sliding tips (B_1 and B_2) were propagating at different intersonic speeds. In the inserts the dual and single Mach lines are marked. (d) Positions of the sliding leading edge, the second sliding tip and the wrinkle-like pulse (C) as a function of time.

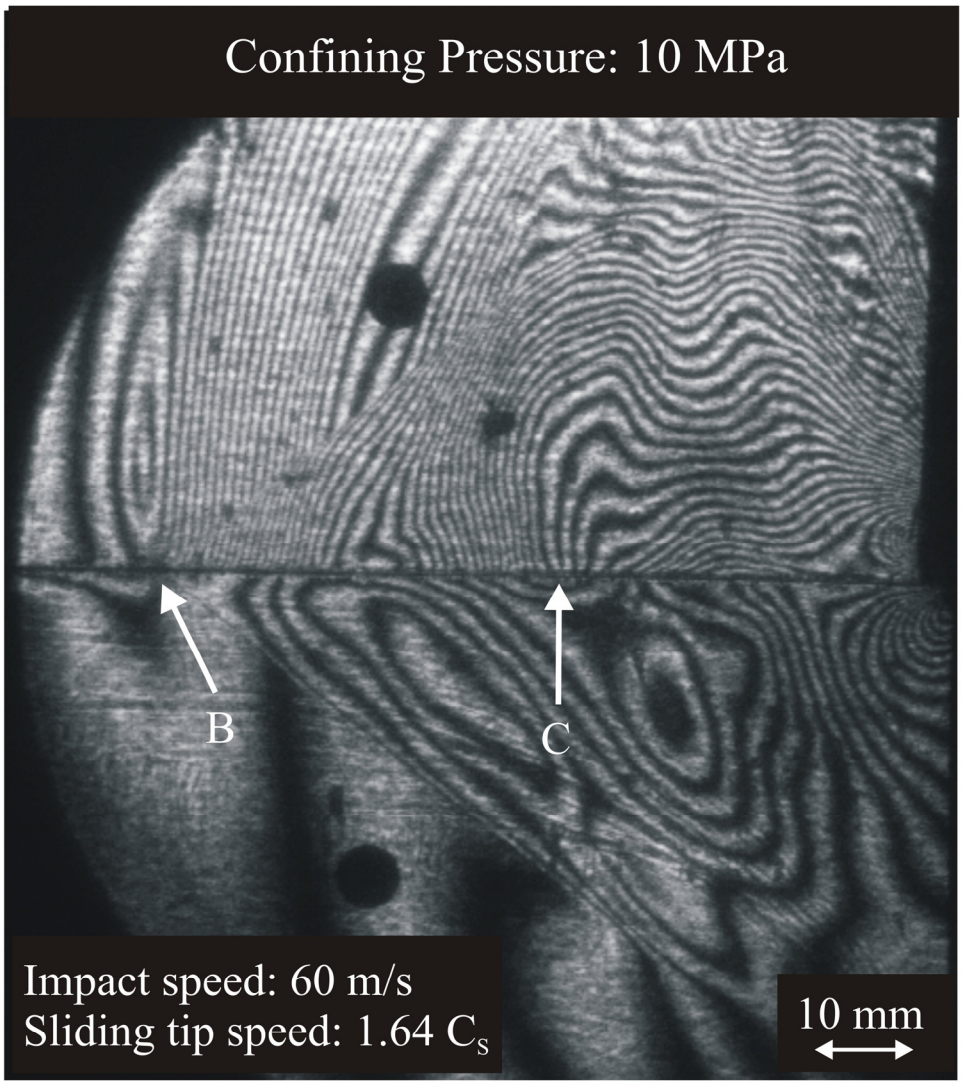

Figure 6 Isochromatic fringes of sliding propagation. The arrows B and C indicate the positions of the rupture tip and of the wrinkle-like pulse respectively.

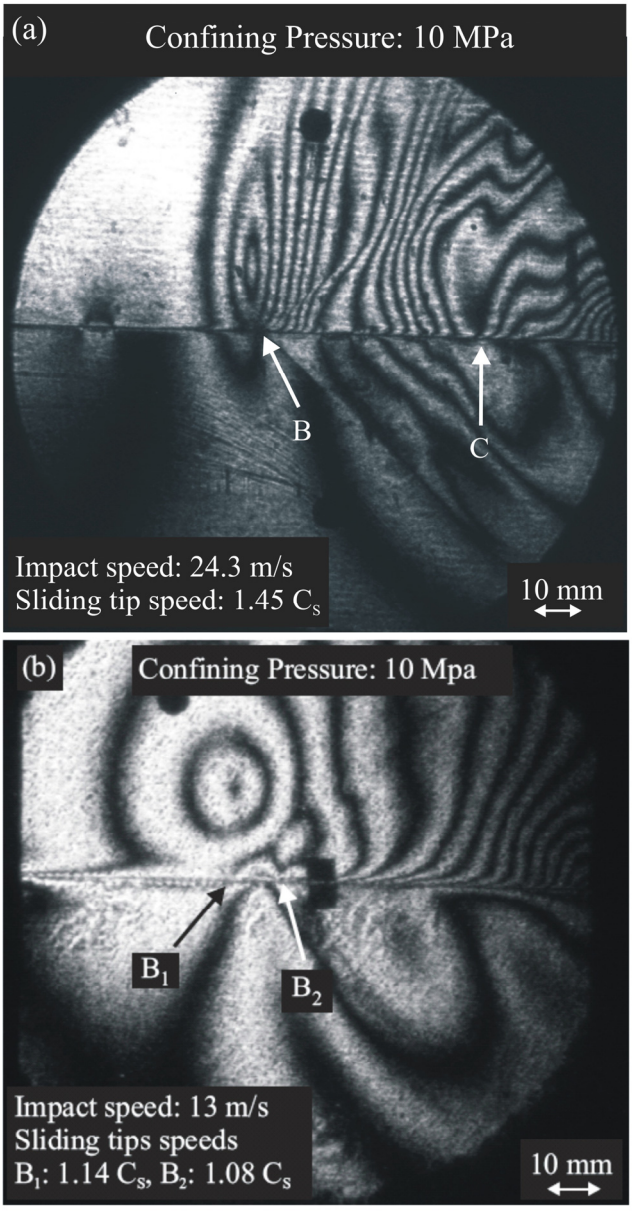

Figure 7 Representative isochromatic fringe patterns from two different experiments of sliding propagation initiated by different impact speeds. The specimens were subjected to the same confining stress. The arrows B and C indicate the positions of the rupture tip and of the wrinkle-like pulse respectively. The arrow B_1 indicates the position of the sliding tip, whereas the arrows B_2 shows the position of a fringe concentration point which corresponds to velocity discontinuity.

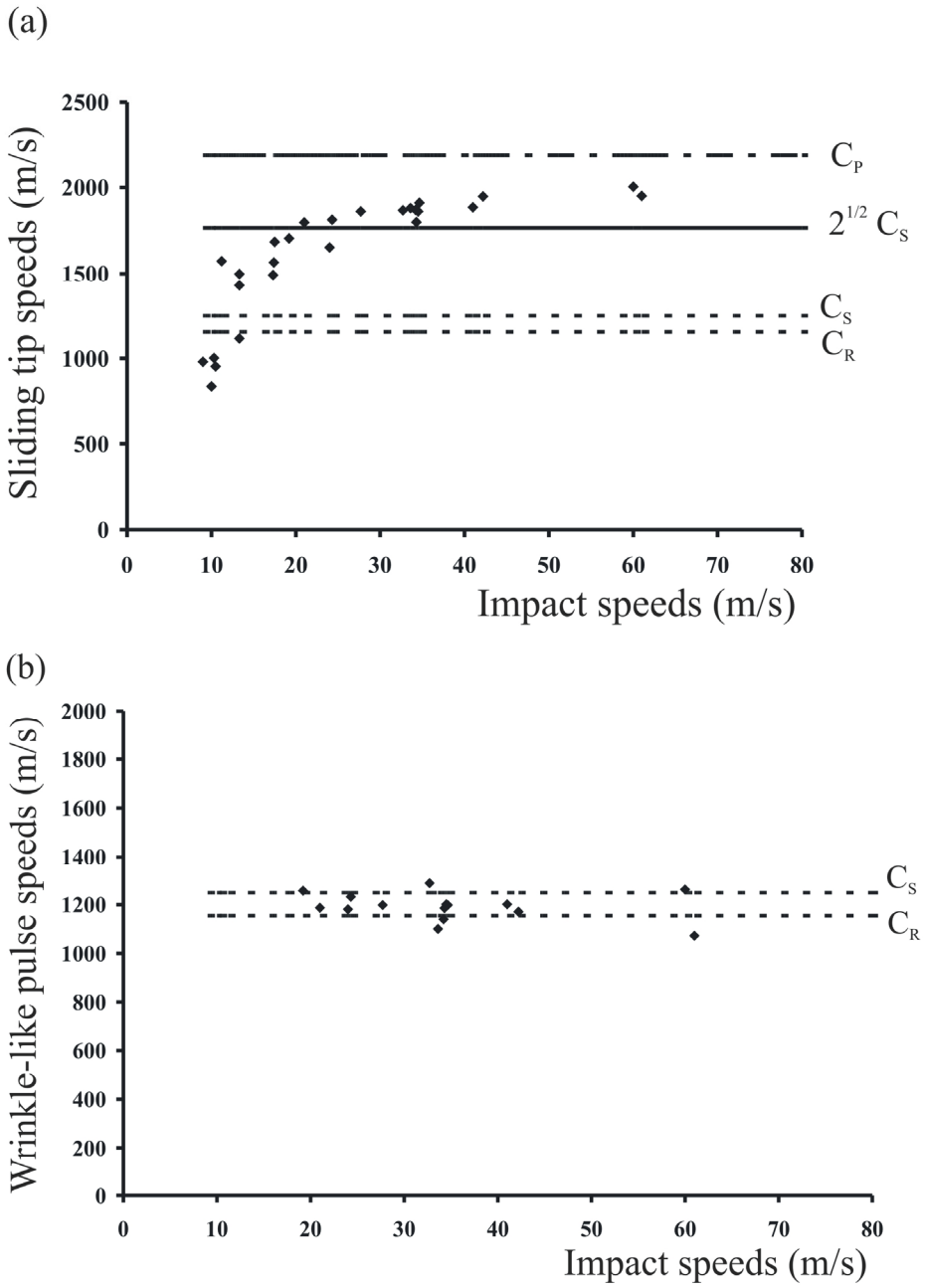

Figure 8 (a) Variation of the sliding tip speed with the impact speed. The confining stress was $10\,MPa$. (b) The wrinkle-like pulse speed remained between the Rayleigh wave speed and the shear wave speed of Homalite-100, independent of the impact speed.

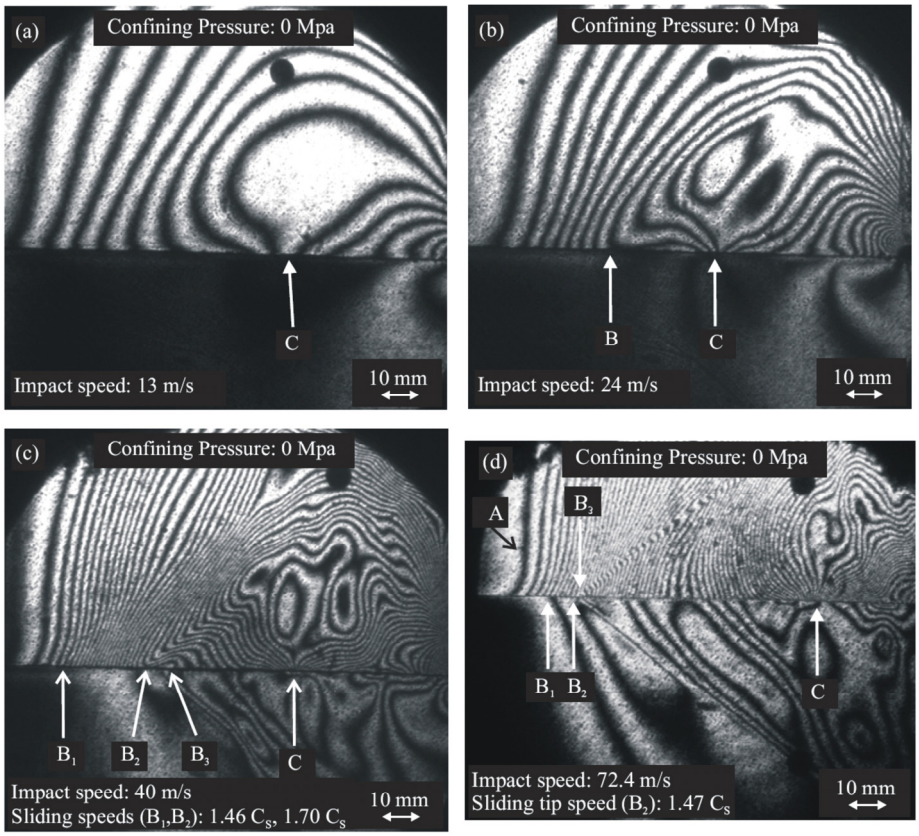

Figure 9 Representative isochromatic fringe patterns from four different experiments of sliding propagation initiated by different impact speeds. No confining stress was applied. The arrows B and C indicate the positions of the rupture tip and of the wrinkle-like pulse respectively. The arrow B_1 indicates the position of the sliding tip, whereas the arrows B_2 and B_3 show the position of fringe concentration points which correspond to velocity discontinuities.

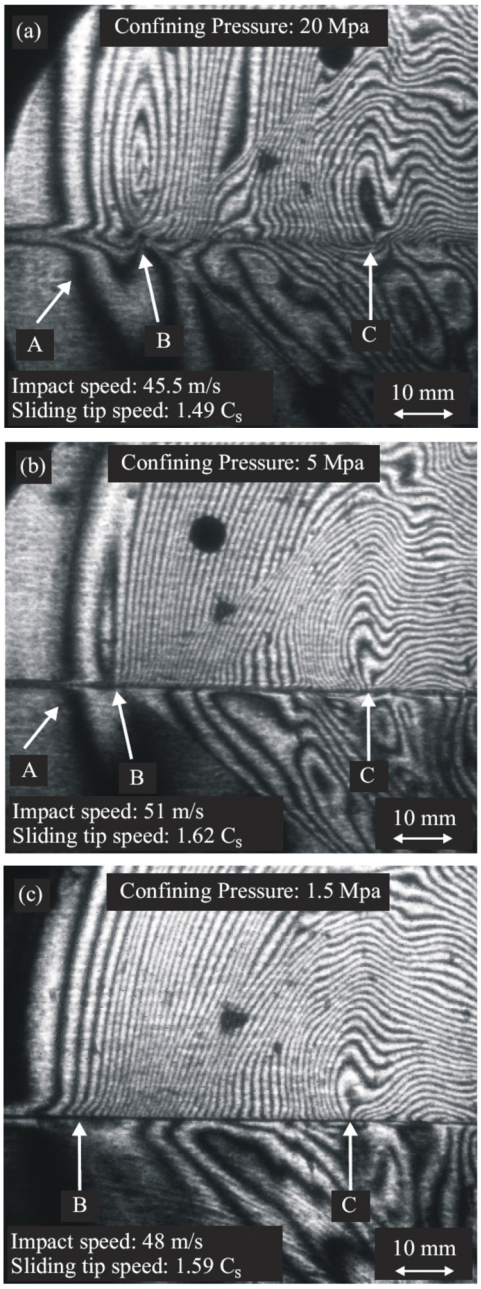

Figure 10 Representative isochromatic fringe patterns from three different experiments of sliding propagation initiated by similar high impact speeds; the specimen was subjected to different confining stresses. Arrows A, B and C show the positions of the P-wave front, of the sliding tip and of the wrinkle-like pulse respectively.

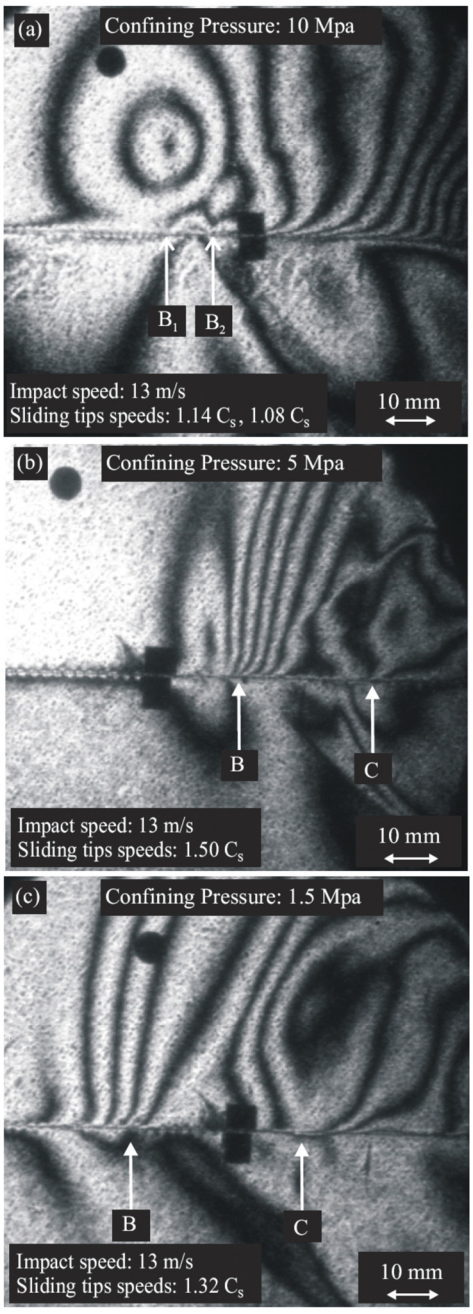

Figure 11 Representative isochromatic fringe patterns from three different experiments of sliding propagation initiated by the same low impact speed; the specimen was subjected to different confining stresses. Arrows B and C show the positions of the sliding tip and of the wrinkle-like pulse respectively. Arrows B_1 and B_2 indicate the position of the sliding tips.

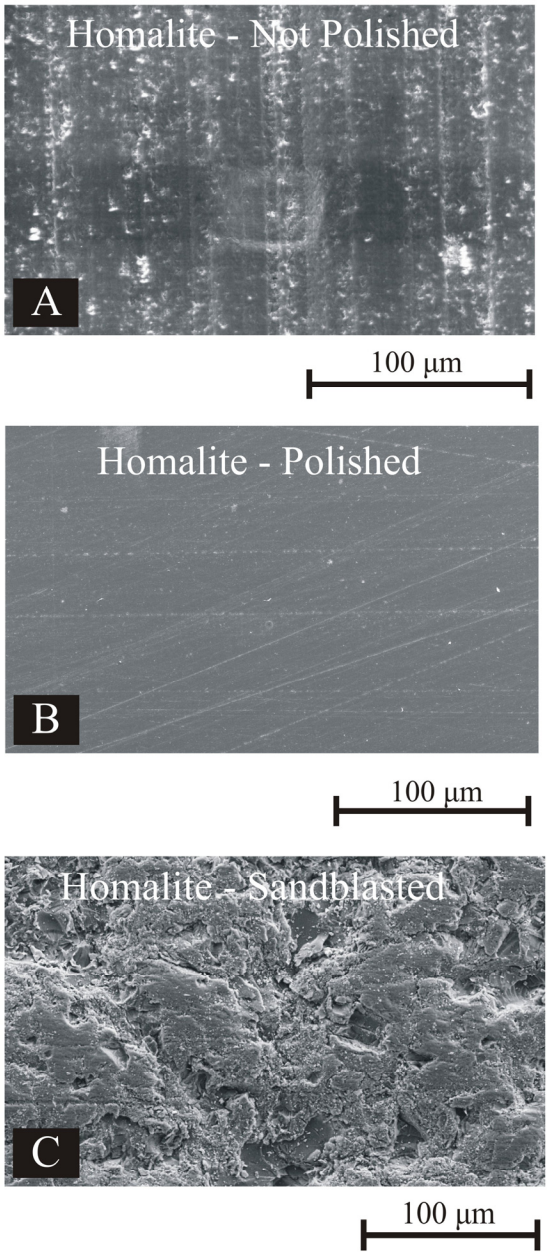

Figure 12 Picture showing sections of unpolished, polished and roughened Homalite surfaces taken via a SEM electronic microscope at a magnification 1000. The surfaces B and C have been carbon coated.

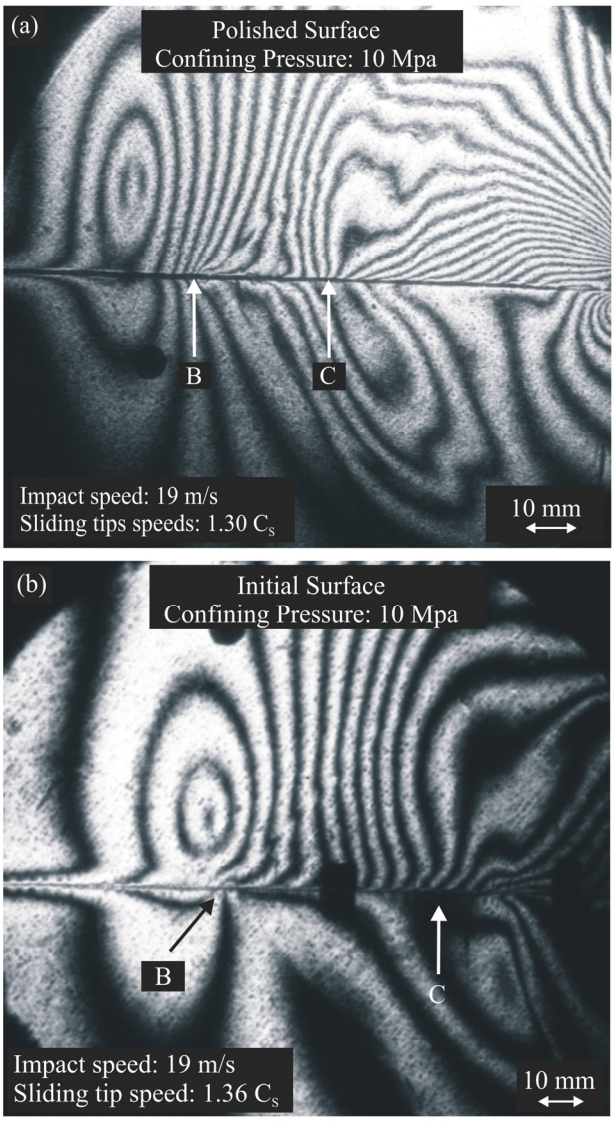

Figure 13 Representative isochromatic fringe patterns developed in two different experiments of dynamic sliding, initiated by the same impact speed. In both cases the specimen were subjected to the same static uniform pressure. (a) The surfaces in contact were polished. (b) The surfaces in contact were unpolished. Arrows B and C indicate the sliding tip and the wrinkle-like pulse respectively.

Figure 14 Representative isochromatic fringe patterns developed in four different experiments of dynamic sliding, initiated by different impact speed. In all cases the specimen were subjected to the same uniform confining stress. The surfaces in contact were polished.

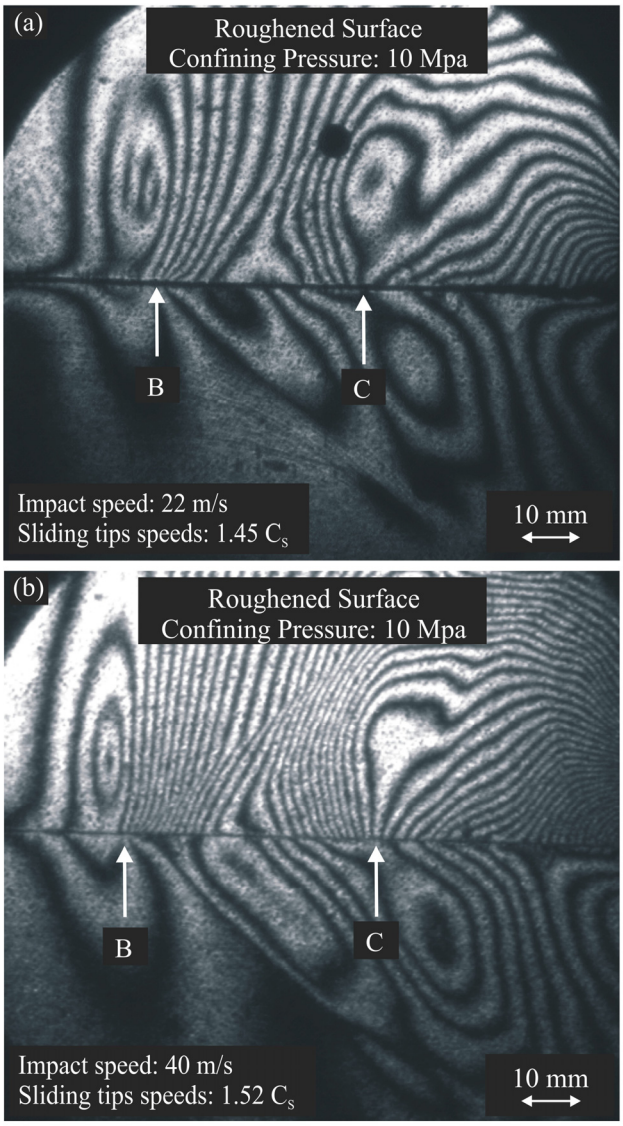

Figure 15 Representative isochromatic fringe patterns developed in two different experiments of dynamic sliding, initiated by different impact speeds. In both cases the specimen were subjected to the same uniform confining stress. The surfaces in contact were roughened.

Chapter 6

EPILOGUE

In this thesis work, dynamic sliding along incoherent (frictional) interfaces was investigated experimentally in a microsecond time scale. A bimaterial system comprised of Homalite and steel plates and a homogeneous system consisting of two Homalite plates were considered. The plates were held together by a uniform compressive stress while dynamic sliding was initiated by an impact-induced shear loading. The evolution of maximum shear stress contours was recorded by high-speed photography in conjunction with dynamic photoelasticity. Simultaneously with photoelasticity, a newly-developed, very accurate technique based on laser interferometry was employed to locally measure, at high temporal resolution, sliding speed at the interface. This technique is suitable for general use and it can be easily employed at different experimental configurations. The combination of velocimetry with the full field technique of photoelasticity is proven to be a very powerful tool in studying fast events in solid structures.

The response of the Homalite-steel bimaterial system differed according to whether the impact loading was applied to the Homalite plate or to the steel plate. In the first case, the interaction between the traveling impact wave and the preexisting static field caused the generation of a relatively broad eye-like fringe formation emanating from the interface and propagating just behind the P-wave front. A disturbance, traveling at the interface at a constant speed (close to the Rayleigh wave speed of steel, which is higher than the shear wave speed of Homalite) generated a shear Mach line crossing the P-wave front and the

eye-like fringe structure. Velocimetry revealed that sliding initiated behind the eye-like fringe pattern. A second shear Mach line, originating from the sliding tip, appeared in the photoelastic images, indicating that the sliding was supershear with respect to the shear wave speed of Homalite. A disturbance, traveling at constant speeds between the shear wave speed and the longitudinal wave speed of Homalite, appeared behind the sliding tip. Self-sustaining wrinkle-like opening pulses, propagating along the bimaterial interface at a constant speed between the Rayleigh wave and the shear wave speed of Homalite, were also observed. When the impact load was applied to the steel plate, the data acquired by the velocimeter were the only useful source of information. Analysis of these data showed that sliding at a given point initiates with the arrival of the P-wave front there, so that the rupture was sonic with respect to the steel and supersonic with respect to the Homalite.

A central issue in the modeling of frictional sliding is the duration of slip at a point on the interface compared to the duration of sliding. The most classic approach to sliding uses shear crack models (crack-like mode), where the slip duration at a point is a significant fraction of the overall sliding. According to the pulse-like model, the duration of slip at a point is considerably shorter than the duration of sliding.

In all the experiments performed on the bimaterial structure (Homalite-steel), sliding always occurred in a crack-like mode. However, in the case of a homogeneous system of Homalite plates, direct physical evidence of different modes of sliding was recorded. Crack-like sliding, pulse-like sliding and mixed mode sliding in the form of pulses followed by a crack were discovered. The propagation speeds of the sliding tips were

dependent on the projectile speed. They spanned almost the whole interval from sub-Rayleigh speeds to nearly the sonic speed of the material, with the exception of a forbidden gap between the Rayleigh wave speed and the shear wave speed. Supersonic trailing pulses were also recorded. Mach lines with different inclinations emanating from the sliding zone tips were discovered. Behind the sliding tip, wrinkle-like pulses were developed for a wide range of impact speeds and confining stresses. They always traveled at speeds between the Rayleigh wave speed and the shear wave speed of Homalite.

Although the results of this work show in an unprecedented detail how dynamic frictional sliding occurs in bimaterials and in homogeneous systems with interfaces, they cannot be directly used to validate the various friction laws since there is no appropriate theoretical solution for the experimental configuration employed here. However, the presented experimental results can be indirectly used to validate the theoretical models of friction through numerical simulations. Finite element calculations can be performed to verify or discard various types of friction laws on the basis of agreement or essential disagreement between the numerical and the experimental results. Finite element calculations on dynamic frictional sliding between deformable bodies have always been a very challenging task for numerical analysts. A main source of difficulty, as was recently recognized (see chapter 1), was the ill-posedness of the corresponding boundary and initial value problem if the right friction law was not implemented. Coker *et al.* (2005) took advantage of the latest advances in frictional sliding theory and by using a rate-enhanced, rate and state friction law of Prakash-Clifton type, they were able to perform stable (grid-size independent) finite element calculations for a configuration very similar to the experiments described above.

Their attempt gave promising results. The use of a rate-enhanced Prakash-Clifton law was an essential element for the successful completion of the simulations because of the presence of fast changes in the local compression at the interface, caused by the wave propagation, during the dynamic sliding. The Prakash-Clifton law is currently considered the only friction law which correctly describes the effect of fast changes in the compression on the frictional resistance. We note that for various impact speeds the numerical simulations exhibit a richer behavior than the experimental results, and generate not only crack-like, pulse-like and mixed mode ruptures but also trains of pulses and pulses following a crack-like rupture. This indicates that the simulated dynamic frictional sliding is very sensitive to various parameters introduced by the friction law. We believe that the similarity between the numerical and the experimental results can perhaps be improved by fine tuning the parameters of the friction law and by perhaps using a more advanced model than elasticity for the description of the response of the bulk to impact loading and to dynamic sliding.

My work in the near future will aim to identify the friction law which is valid during dynamic sliding. Finite simulations can be used to distinguish between the various friction laws and to perhaps discard some categories of friction laws which profoundly disagree with the experimental results. We also plan to investigate other experimental configurations which are either closer to theoretically studied boundary value problems and/or are easier to simulate. In this way, the comparison between the theoretical and experimental results will give more reliable conclusions.

REFERENCES

Coker, D., Lykotrafitis, G., Needleman, A. & Rosakis, A. J. Frictional sliding modes along an interface between identical elastic plates subject to shear impact loading. *J. Mech. and Phys. of Solids*. **53**, 884-922 (2005).